



**INVESTIGATION OF THE EFFECTS OF TARGET
FEATURE VARIATIONS ON BALLISTIC MISSILE RCS**

THESIS

Sang H. Lee, First Lieutenant, USAF
AFIT/GE/ENG/06-34

**DEPARTMENT OF THE AIR FORCE
AIR UNIVERSITY**

AIR FORCE INSTITUTE OF TECHNOLOGY

Wright-Patterson Air Force Base, Ohio

APPROVED FOR PUBLIC RELEASE; DISTRIBUTION UNLIMITED

The views expressed in this thesis are those of the author and do not reflect the official policy or position of the United States Air Force, Department of Defense, or the United States Government.

AFIT/GE/ENG/06-34

INVESTIGATION OF THE EFFECTS OF TARGET FEATURE VARIATIONS ON
BALLISTIC MISSILE RCS

THESIS

Presented to the Faculty

Department of Electrical and Computer Engineering

Graduate School of Engineering and Management

Air Force Institute of Technology

Air University

Air Education and Training Command

In Partial Fulfillment of the Requirements for the
Degree of Master of Science in Electrical Engineering

Sang H. Lee, BSEE

First Lieutenant, USAF

March 2006

APPROVED FOR PUBLIC RELEASE; DISTRIBUTION UNLIMITED.

INVESTIGATION OF THE EFFECTS OF TARGET FEATURE VARIATIONS ON
BALLISTIC MISSILE RCS

Sang H. Lee, BSEE
First Lieutenant, USAF

Approved:

//Signed//
James A. Fellows (Chairman)

date

//Signed//
Michael J. Havrilla (Member)

date

//Signed//
Andrew J. Terzuoli (Member)

date

Abstract

Uncertainties in certain features of target geometries result in a loss of confidence in the signature assessment of the target. Knowledge of the impact to a target's radar cross section (RCS) due to changes to specific target features can assist to identify whether uncertainty in a certain target feature warrants a loss of confidence in the target signature. This study will allow a development of a general "rule-of-thumb" on how the radar signature of a target varies as a function of the target's specific target features. The targets of interest which this study is centered around are fictitious ballistic missiles. Four target features that were investigated: fin size, nosecone shape, effect of panel riveting along the sides of the missile and the effects of heat shielding on the nosecone. By varying each of the four target features into a missile configuration and comparing to another configuration, a relationship between specific target features and its effect on the radar cross section of a ballistic missile can be obtained. Based on the range of possible configurations that target's feature can take, it is possible to estimate a range of possible values of the radar signature. This will enable the user of the signature data to have a better understanding of the target being assessed and target characteristics when a complete knowledge of target configuration is unavailable.

AFIT/GE/ENG/06-34

To My Grandparents

Acknowledgments

To start off, I would like to express my sincere appreciation to my faculty advisor, Lt. Col. James A. Fellows, for his patient guidance and wisdom throughout the course of this thesis effort. I would also like to thank my committee members, Dr. Michael J. Havrilla and Dr. Andrew J. Terzouli, for lending me their immense knowledge and expertise.

Many thanks goes out to my Bob Schalle, Richard Bowman, Lt. Mark Wilson, Andrea Gilkey and the others at NASIC/AENS who kindly provided the technical knowledge and the resources I needed to complete this study. I would also like to thank Capt. Gary Krupp and Janet Krupp for enlightening me in the ways of Unix and XPatch.

My heartfelt gratitude goes out to William F. Boyee who always encouraged me to do “whatever makes my heart beat fast.” He has been a model of unselfishness and encouragement. A special thanks to my classmate and dear friend, Capt. Paul Lash, who has waded through more mud with me at AFIT than anyone else.

I thank my friends who motivated me and brought humor into my days. Three friends I would like to thank specifically are Phil, Reed and Zach for helping me through one of the darkest times in my life to find “peace and zen.”

I offer my deepest appreciation to my parents for raising me, my sisters for their moral support, my grandmother for instilling her values in me at a young age, and my grandfather for always setting an example of how one should lead their lives.

Last but not least, I would like to thank my Lord and Savior, Jesus Christ, for His gift of life, for being an anchor in my life in times of storms, and for His most precious

and unbreakable promises. “So do not fear for I am with you; do not be afraid, for I am your God. I will strengthen you and help you; I will uphold you with my righteous right hand.” (Isaiah 41:10)

Sang H. Lee

Table of Contents

	Page
Abstract	iv
Acknowledgments.....	vi
Table of Contents.....	viii
List of Figures	x
List of Tables	xiii
 1 Introduction.....	 1
1.1 Background.....	1
1.2 Problem Statement	2
1.3 Scope.....	2
1.4 Methodology	5
1.5 Development	6
 2 Background	 8
2.1 Introduction to Radar Cross Section	8
2.2 RCS of Simple Targets	9
2.3 RCS of Complex Targets	13
2.4 Effects of Changing Geometries on RCS	15
2.5 Analyzing RCS Uncertainty	17
2.6 Evaluation of RCS at High Frequencies	21
2.7 Data Reduction and Presentation Techniques.....	23
 3 Methodology	 25
3.1 Target Geometry	25
3.2 XPatch Data Collection.....	31
3.3 Data Reduction and Missile Comparison for XPatch Data	34
3.4 Comparing Missile Configurations Utilizing C&S Formulations	42
3.4.1 Modeling Missile Configurations Using C&S Formulations	42
3.4.2 Limitations of Approximating Complex Targets.....	45
 4 Analysis and Results	 48
4.1 Analysis on the Effects of Nosecones.....	48
4.1.1 Simple Conic vs. Bi-conic	48
4.1.2 Simple Conic vs. Broken	52
4.1.3 Bi-conic Nosecone vs. Broken.....	55
4.1.4 Summary of Nosecones	57
4.2 Analysis on the Effects of Fins	57
4.2.1 Finless vs. Small Fins	58
4.2.2 Finless vs. Large Fins	63

4.2.3	Small Fins vs. Large Fins.....	65
4.2.4	Summary of Fins.....	67
4.3	Analysis on the Effects of Heat Shielding	68
4.3.1	Heat Shielding on Conic Nosecone	68
4.3.2	Heat Shielding on the Bi-conic Nosecone	71
4.3.3	Heat Shielding on the Broken Nosecone	73
4.3.4	Summary of Heat Shielding.....	75
4.4	Analysis on the Effects of Paneling	76
5	Conclusion	79
5.1	Missile Components Conclusions.....	79
5.2	Conclusions of XPatch and C&S Approximations	80
5.3	Recommendations for Follow-On Research.....	81
Appendix A: Sample XPatch Input File		83
Appendix B: MATLAB RCS Approximation Code.....		86
Bibliography		96

List of Figures

	Page
Figure 1-1: Diagram of a generic ballistic missile.....	2
Figure 1-2: Coordinate space of the generic missile.....	5
Figure 3-1: Diagram of the simple conic nosecone.	26
Figure 3-2: Diagram of the bi-conic nosecone	26
Figure 3-3: Diagram of the “broken” nosecone.....	27
Figure 3-4: Diagram of the ‘small’ (left) and ‘large’ (right) fin configurations.	27
Figure 3-5: Diagram of panel and rivet placement on the generic ballistic missile.	29
Figure 3-6: Screenshot of a missile facet file (blue) along with its corresponding extracted edges (black) viewed in XPatch.....	32
Figure 3-7: The effects of leaking rays in XPatch.	33
Figure 3-8: Mean RCS and 2 standard deviation bounds of 32 X-band frequencies plotted over each individual frequency (colored) in VV polarization at $\theta = 15^\circ$	36
Figure 3-9: Difference between 2 standard deviation upper bound and lower bound of the 32 X band frequency RCS plots in VV polarization at $\theta = 15^\circ$	36
Figure 3-10: Arithmetic RCS of finless missile configuration and small fin missile configuration.	37
Figure 3-11: C&S RCS comparison between simple conic and bi-conic nosecone missile configurations over elevation in X-band at HH polarization.....	39
Figure 3-12: XPatch RCS comparison between finless and small fin missile configurations over elevation in X band at VV polarization.	40
Figure 3-13: XPatch difference plots of finless missile configurations vs. large fin missile configurations plotted over varied configurations.	41
Figure 4-1: XPatch and C&S difference plots of the simple conic nosecone vs. the bi-conic nosecone configurations over X band frequencies.....	49

Figure 4-2: XPatch and C&S difference plots of the simple conic nosecone vs. the bi-conic nosecone configurations over L-S band frequencies.....	49
Figure 4-3: XPatch RCS of simple conic nosecone configuration compared to RCS of bi-conic nosecone configuration at X band in HH polarization at $\theta = 0^\circ$	50
Figure 4-4: XPatch RCS of bi-conic nosecone missile plotted in X band and L-S band illustrating loss of resolution of conic component specular return peaks at lower frequencies.	51
Figure 4-5: XPatch and C&S difference plots of the simple conic nosecone vs. the broken nosecone configurations over X band frequencies.	52
Figure 4-6: XPatch and C&S difference plots of the simple conic nosecone vs. the broken nosecone configurations over L-S band frequencies.	53
Figure 4-7: XPatch RCS of simple conic nosecone configuration compared to RCS of broken nosecone configuration at X band in VV polarization at $\theta = 0^\circ$	54
Figure 4-8: C&S RCS of simple conic nosecone configuration compared to RCS of broken nosecone configuration at X band at $\theta = 0^\circ$	54
Figure 4-9: XPatch and C&S difference plots of the bi-conic conic nosecone vs. the broken nosecone configurations over X band frequencies.	55
Figure 4-10: XPatch and C&S difference plots of the bi-conic nosecone vs. the broken nosecone configurations over L-S band frequencies.	56
Figure 4-11: XPatch and C&S difference plots of the finless missile configuration vs. the small fin missile configuration over X band frequencies.	58
Figure 4-12: XPatch and C&S difference plots of the finless missile configuration vs. the small fin missile configuration over L-S band frequencies.	59
Figure 4-13: XPatch screenshot of missile fins with curved edges.	59
Figure 4-14: XPatch RCS comparison between finless and small fin missile configurations over elevation in X band at VV polarization.	60
Figure 4-15: C&S RCS comparison between finless and small fin missile configurations over elevation in X band at VV polarization.	61
Figure 4-16: Illustration of difference of specular returns between curved fin edges and flat fin edges over elevation.	62

Figure 4-17: XPatch and C&S difference plots of the finless missile configuration vs. the large fin missile configuration over X band frequencies.	64
Figure 4-18: XPatch and C&S difference plots of the finless missile configuration vs. the large fin missile configuration over L-S band frequencies.	64
Figure 4-19: XPatch and C&S difference plots of the small fin missile configuration vs. the large fin missile configuration over X band frequencies.	65
Figure 4-20: XPatch RCS comparison between small and large fin missile configurations over elevation in X band at HH polarization.	66
Figure 4-21: XPatch and C&S difference plots of the small fin missile configuration vs. the large fin missile configuration over L-S band frequencies.	67
Figure 4-22: XPatch difference plots of the PEC conic nosecone missile configuration vs. the heat shielded missile configuration over X band frequencies.	69
Figure 4-23: XPatch difference plots of the PEC conic nosecone missile configuration vs. the heat shielded missile configuration over L-S band frequencies	70
Figure 4-24: XPatch RCS of PEC conic nosecone configuration compared to RCS of heat shielded nosecone configuration.	71
Figure 4-25: XPatch difference plots of the PEC bi-conic nosecone missile configuration vs. the heat shielded missile configuration over L-S band frequencies.	72
Figure 4-26: XPatch difference plots of the PEC bi-conic nosecone missile configuration vs. the heat shielded missile configuration over L-S band frequencies.	72
Figure 4-27: XPatch difference plots of the PEC broken nosecone missile configuration vs. the heat shielded missile configuration over X band frequencies.	74
Figure 4-28: XPatch difference plots of the PEC broken nosecone missile configuration vs. the heat shielded missile configuration over L-S band frequencies.	74
Figure 4-29: XPatch difference plots of non-paneled missile configurations vs. paneled missile configuration over X band frequencies.	76
Figure 4-30: XPatch difference plots of non-paneled missile configurations vs. paneled missile configuration over L-S band frequencies.	76
Figure 4-31: XPatch RCS plot comparison of a paneled and non-paneled missile configuration in HH-polarization at $\theta = 0^\circ$	77

List of Tables

	Page
Table 3-1. Table of missile configurations	30

1 Introduction

1.1 *Background*

The signatures branch of the National Air and Space Intelligence Center (NASIC) performs radar signature assessments against all foreign aerodynamic threat systems. Foreign powers are understandably unwilling to share knowledge of their military capabilities with competing nations. Reconnaissance, surveillance, and other intelligence gathering techniques are employed in order to obtain information on foreign threat systems. Unfortunately, obtaining all information on state-of-the-art threat systems from an uncooperative power is a near impossibility. Due to the speculative nature in which the intelligence community gathers its information, there are uncertainties inherent in the predicted features of an unknown target. Uncertainties in target features result in a loss of confidence in the signature assessment of the target. A study on the impact of specific target features on the target's radar signature can tell us whether uncertainty in a certain target feature warrants a loss of confidence in the radar assessment or not. Based on the range of possible configurations that target's feature can take, it may be possible to evaluate a good estimate on the possible values of the radar signature. This will enable the user of the signature data to have a better understanding of the target he's assessing and what the target's characteristics are when a complete set of target data is unavailable.

The targets of interest that this thesis will address are ballistic missiles. The ability to accurately detect hostile missiles by radar depends directly on how well the radar signature of the threat is characterized. High fidelity signature prediction is crucial

for early warning, target identification, target acquisition and tracking, and missile defense.

1.2 Problem Statement

To investigate how the monostatic radar signature changes as a result of changes in four specific ballistic missile features: nosecones, fins, heat shielding and panels.

1.3 Scope

The targets of interest in this thesis are limited to ballistic missiles. A generic ballistic missile is shown in Figure 1-1. Four specific features of ballistic missiles will be looked at: nosecones, fins, heat shielding and panels.

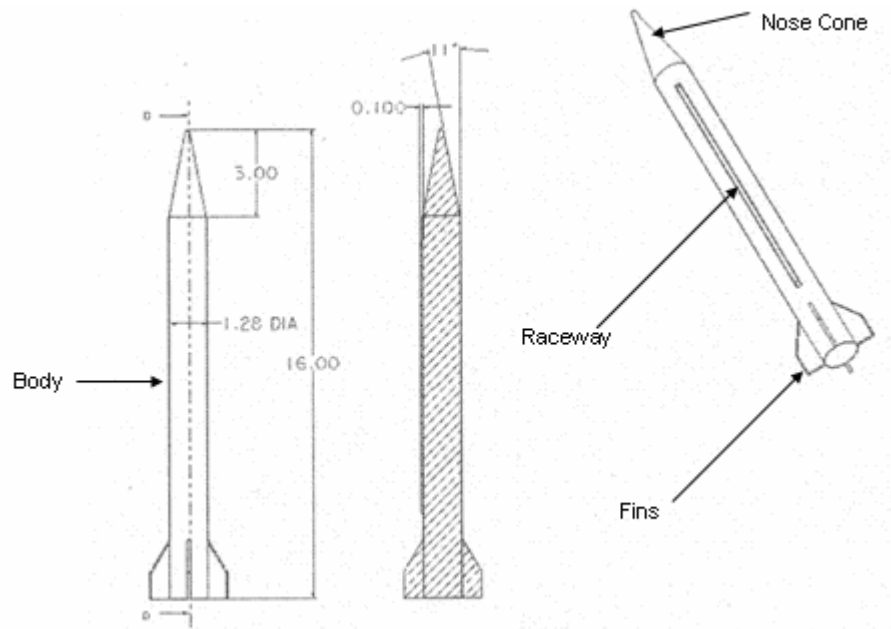


Figure 1-1: Diagram of a generic ballistic missile.

Nosecone: A nosecone is the tip of the missile. The shape of the nosecone is dependent on the type of warhead contained within it. Ballistic missiles fly past the upper atmosphere and into space in an effort to cut down on drag caused by the air in the atmosphere. When a ballistic reaches its final stages of flight and approaches its destination the nosecone portion of the missile, which contains the warhead, breaks off and re-enters the atmosphere towards its intended target. For this reason, the nosecone portion of the missile is referred to as the re-entry vehicle or RV. “Most ballistic missile re-entry vehicles shapes are conical or ogival at the nose with the ‘tip’ often rounded off with a segment of a section.” [1] Thus the radar signature can be approximated as segments of ogives or spheroids.

Fins: The fins on any missile serve to stabilize the body during flight. Because ballistic missiles are designed to travel very long distances, they usually have significantly smaller fins than conventional short range missiles. The drag created by the air moving along the fins can significantly cut down the distance a ballistic missile can travel; thus many ballistic missiles do not have any fins at all. From a signatures point of view, “... fins have the basic appearance of flat plates or thin wedges.” [1]

Panels: In many past works, bodies of missiles have been modeled as perfectly smooth cylinders. In real life there are panels on the bodies of missiles. These panels give access to the circuitry, armament and other devices within the missile. The presence of panels introduces sharp discontinuities and small gaps within the otherwise smooth bodies of the missiles. The panels are also held down by metallic rivets. Panels and riveting may diminish the validity of modeling the body of a missile as a smooth continuous surface.

Heat Shielding: Usually the RV is covered with heat shielding material to protect the warhead from overheating due to air friction when it re-enters the atmosphere. From a signatures standpoint, the heat shield is a dielectric material that covers the nosecone. Due to the difference in material properties between the heat shield and perfect electric conductors (PEC), there will be a difference in the radar signature. A PEC is an object that has infinite conductivity. All electric currents travel on the surface of a PEC structure and no electric fields can exist within the structure. Though true PECs do not exist in real life, metals can be very closely modeled as a PEC.

The four features were chosen based on NASIC/ADNS's assessment of which target features on a ballistic missile were of most interest to them. Any other non-varied features on the geometry of the generic missile model will be a compilation of commonly seen features on other ballistic missiles provided by the sponsor office.

The radar signatures of the missile will be evaluated at 2 bands of frequencies: X band frequency (8.5-10.5 GHz) and L-S band frequency (1.5-3.5 GHz). The two frequency bands were chosen due to the wishes of the sponsor. A ballistic missile illuminated at X and L-S band frequencies makes the missile an electrically large target; meaning the dimensions of the target are much greater than the wavelengths of the illuminating frequencies. The electrically large nature of our targets allows us to use high frequency asymptotic techniques in this study.

A high emphasis is placed on target shape in this thesis. With the exception of heat shielding, the effects of dielectric materials or differing material features are not taken into consideration in this thesis. All target components, with the exception of the heat shield, are considered to be PEC.

1.4 Methodology

The electrically large nature of the ballistic missile in the frequencies of interest allows us to use high frequency approximations. X-Patch, an electromagnetics code using a high frequency asymptotic solver, will be employed to obtain target radar signature data. Though a code utilizing full wave solvers (i.e. FISC, CARLOS, SAF, *etc*) will generate more accurate results, the time required to obtain the solution on full wave solvers may take months or even years to complete. In the interest of completing this thesis in a timely manner, high frequency asymptotic solutions will be applied.

Figure 1-2 shows the generic missile within its defined coordinate space. The missile body is concentric with the x-axis. The center of the circular flat end of the missile lies at the origin of the coordinate system. The azimuth angle, ϕ , is the angle formed on the x-y plane by the radar's line of sight and the x-axis. The elevation angle, θ , is the angle formed by the radar's line of sight and the x-y plane.

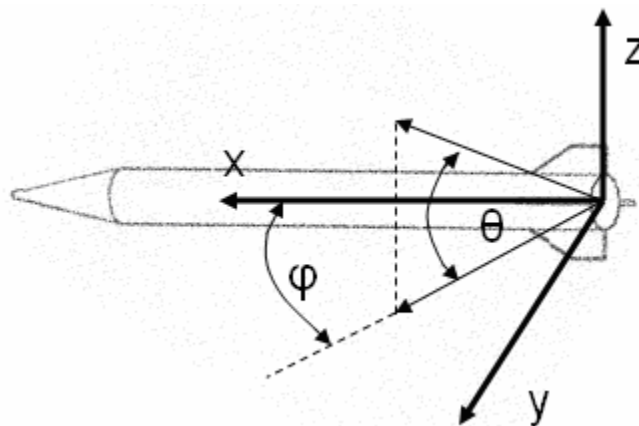


Figure 1-2: Coordinate space of the generic missile.

Four specific features of a generic ballistic missile will be varied with respect to commonly observed variations seen in the intelligence community. Each combination of the four varied features in the missile geometry will be evaluated by X-Patch and the output will be radar signature data with respect to a range of aspect angles. All 360° in azimuth around the length of the missile and the $-15^\circ \leq \varphi \leq 15^\circ$ sector in elevation will be analyzed.

Using a combination of statistical and averaging methods, which are discussed further in Chapters 2 and 3, a MATLAB routine will be written that compiles all the radar signature data from the X-Patch results into a format where the data can be easily analyzed. By analyzing each variable target feature independently by holding the other three variable features constant, the effects of a specific variable target feature on radar signature can be isolated.

1.5 Development

The content in each of the following chapters are summarized below:

Chapter 2 lays the technical foundations of this study with a literature review.

The concept of radar cross section (RCS), simple and complex shapes in terms of RCS, uncertainty associated with RCS measurement, high frequency approximations, and data analysis and reduction techniques will be reviewed according to past works.

Chapter 3 discusses the methodology used to approach the problem. The technique that Crispin, Maffet and Siegel developed [1, 2, 3] to obtain a radar signature estimate of complex targets will be applied specifically to the generic missile model and

its variations. A discussion of the X-Patch software package and the manner in which its resultant files will be analyzed will be given as well.

Chapter 4 evaluates the results and analysis of this thesis. The signature data given by X-Patch will be compiled through the use of data analysis and reduction techniques developed in Chapters 2 and 3. A parametric study will be performed from the compilation of raw X-Patch data. The results of the parametric study will be compared to the results of the theoretical target predictions based on the works of Crispin and Siegel [2] in an effort to validate the parametric study.

Chapter 5 will end the thesis with concluding remarks and recommendations for future studies.

2 Background

2.1 Introduction to Radar Cross Section

The concept of radar cross section will be introduced in this section because it is a fundamental concept that the rest of this thesis is based on. Radar cross section (RCS) is a measure of how much scattering is received at a receiver from an illuminated target. Knott [4] describes RCS (σ) mathematically as

$$\sigma = \lim_{r \rightarrow \infty} 4\pi r^2 \left| \frac{\bar{E}_s}{\bar{E}_i} \right| \quad (2.1)$$

where \bar{E}_i is the incident electric field vector and \bar{E}_s is the scattered electric field vector.

The variable r is the distance (or range) from the receiver to the target. The limit of r in equation (2.1) is set to infinity so that the RCS is independent of range at which the receiver is from the target.

According to Crispin and Maffet [2], the RCS of an object is dependent on:

1. the frequency of incident radiation,
2. the polarization of transmitting antenna,
3. the polarization of receiving antenna,
4. the material which the target is composed of and
5. the geometry of target.

It is important to note here that, though not listed, the position of the transmitting and receiving antennas relative to the target is critical to RCS as well. All data collected in this thesis is for the monostatic case.

2.2 RCS of Simple Targets

The term simple shape refers to geometric shapes whose exact solutions for the wave equation exist due to the separable nature of their surface coordinate systems (*e.g.* sphere, infinite plate, *etc*). They also refer to shapes that are encountered frequently in signature assessment and whose RCS values are intuitively obvious (*e.g.* ogive, finite cone). Crispin and Maffet [3] describes simple shapes as “...a configuration whose geometry is not particularly involved and also one in which the RCS is determined for the most part by a relatively small number of contributions.”

Any scattering problem can be characterized in terms of some characteristic dimension, d , and the wavelength of the illuminating frequency, λ . The RCS contributions can be classified “in terms of their principal radii or curvature at the point where the normal to the surface is parallel to the direction of incidence.” [3] These classes are

1. 2 infinite radii of curvature (plane)
2. 1 infinite, 1 nonzero finite (cylinder)
3. 1 infinite, 1 zero (wedge)
4. 2 nonzero finite (spheroid)
5. 1 nonzero finite, 1 zero (nonplanar edge)
6. 2 zero (point)

All the elementary scatterers within these classifications have a RCS that is a function of a characteristic target dimension and the wavelength of the illuminating wave. Mathematically, the RCS of the simple elementary scatterers have the form

$$\sigma = \lambda^m f(d / \lambda) \quad (2.2)$$

Where d is a characteristic length of the target, λ is the wavelength of the illuminating frequency, and $f(d/\lambda)$ represents a function of target characteristic length divided by wavelength (whatever that function may be). The value of the exponent term, m , is equal to -2, -1, 0, 1, or 2 respective to the 5 simple shape classes.

Crispin, Siegel and Maffet [2, 3] developed key RCS expressions for certain simple shapes in the optics region which will be introduced shortly. Simple shapes that are of interest in this thesis are those that are commonly found on ballistic missiles such as the ogive, cone, and cylinder. It must be noted that the RCS formulas given in this section are only to be applied in the optics region where the characteristic dimension of the target is at least 10 times as long as the wavelength of the illuminating frequency. Commonly seen simple shapes on missiles include

Ellipsoids: Ellipsoid features are regularly seen on missiles, especially on the head of the missile. An ellipsoid is described by the equation

$$\left(\frac{x}{a}\right)^2 + \left(\frac{y}{b}\right)^2 + \left(\frac{z}{c}\right)^2 = 1 \quad (2.3)$$

where x , y , and z are Cartesian coordinates in 3-dimensional space variables a , b , and c characterize the ellipsoid's geometry. The ellipsoid described in equation (2.3) has an RCS value that can be described by [2]

$$\sigma = \frac{\pi a^2 b^2 c^2}{\left(a^2 \sin^2 \theta \cos^2 \phi + b^2 \sin^2 \theta \sin^2 \phi + c^2 \cos^2 \theta\right)^2} \quad (2.4)$$

The angles ϕ and θ are the azimuth and elevation angles, respectively, of the location of the radar.

Ogives: “Most ballistic missile re-entry vehicle shapes are conical or ogival at the nose with the ‘tip’ rounded off with a segment of a sphere.” [3] An ogive is obtained

when an arc on a circle of radius R_I is rotated about a chord of length L , whose midpoint is at a distance $R_I - a$ away from the center of the circle, where a is a value less than R_I .

The dimensions of the ogive are related by

$$\cos \alpha = 1 - (a / R_I) \quad (2.5)$$

and

$$L / 2 = \sqrt{R_I^2 - (R_I - a)^2} \quad (2.6)$$

where α is the half angle of the ogive.

After the optics approach is applied, the RCS of the ogive when $0^\circ \leq \theta < \sim (90^\circ - \alpha)$ is approximated by [2]

$$\sigma(\theta) = \frac{\lambda^2 \tan^4 \alpha}{16\pi \cos^6 \theta (1 - \tan^2 \alpha \tan^2 \theta)^3} \quad (2.7)$$

At $\theta = (90^\circ - \alpha)$, the RCS of the ogive is given by [2]

$$\sigma(90^\circ - \alpha) = \frac{a^2}{4\pi \tan^2(\alpha / 2)} \quad (2.8)$$

and in the region $\sim (90^\circ - \alpha) < \theta \leq 90^\circ$ [2]

$$\sigma(\theta) = \pi R_I^2 \left(1 - \frac{R_I - a}{R_I \sin \theta} \right) \quad (2.9)$$

Cones: As mentioned previously, a conical tip is a commonly seen feature in many ballistic missiles. The geometry of the circular finite cone can be written as

$$x^2 + y^2 = z^2 \tan^2 \alpha \quad (2.10)$$

where α is the half angle of the cone.

The RCS at normal incidence to the cone of length, L , can be described as [2]

$$\sigma_{\perp} = \frac{8\pi L^{\frac{3}{2}} \sin \alpha}{9\lambda \cos^4 \alpha} \quad (2.11)$$

The RCS of the circular cone at non-normal incidence is [2]

$$\sigma = \frac{\lambda L \tan \alpha \tan^2(\theta - \alpha)}{8\pi \sin \theta} \quad (2.12)$$

Cylinders: The cylinder is an obvious feature of a missile as it comprises most of the missile body. The RCS of a cylinder with a radius of length a and length of L at normal incidence ($\theta = 90^\circ$) is [2]

$$\sigma_{\perp} = \frac{2\pi L^2 \sin \theta}{\lambda} \quad (2.13)$$

For non-normal incidence, the RCS can be written as [2]

$$\sigma = \frac{\lambda a^2 \sin \theta}{8\pi \cos^2 \theta} \quad (2.14)$$

Plates: “Almost all fins [on missiles] have the basic appearance of plates or thin wedges.” [1] The RCS of a circular plate of radius a , off normal incidence can be described by [2]:

$$\sigma = \frac{\pi a^2}{\tan^2 \theta} \left[J_1 \left(\frac{4\pi a \sin \theta}{\lambda} \right) \right]^2 \quad (2.15)$$

where J_1 is a Bessel function of the first order.

A square flat plate with side length a , off normal incidence can be described by:

$$\sigma = \frac{4\pi a^4}{\lambda^2} \left[\frac{\sin(ka \sin \theta)}{ka \sin \theta} \right]^2 \quad (2.16)$$

At normal incidence, any flat plate with an area A will have an RCS of:

$$\sigma = \frac{4\pi A^2}{\lambda^2} \quad (2.17)$$

2.3 RCS of Complex Targets

In Section 2.2, simple shapes were introduced which described features of a ballistic missile very well. However, a ballistic missile is a combination of features. For complex targets that are composed of two or more simple shapes, such as ballistic missiles, Crispin and Maffet [1] offer an RCS prediction technique. The RCS of a complex target can be predicted in three steps:

1. The complex shape is “resolved into” an ensemble of components each of which can be geometrically approximated by a simple shape in such a way that the RCS of a simple shape approximates the component it replaces.
2. RCS values are computed for the approximations to the components (simple shapes) derived in step 1.
3. Steps 1 and 2 are then combined to yield an estimate of the RCS of the entire body.

The effects of a collection of simple shapes that make up a target can be summed to find an estimate of the RCS of the complex target. Summing coherently results in the relative phase method. The RCS of a complex target that is composed of N components can be described using the relative phase method as:

$$\sigma = \left| \sum_{j=1}^N (\sigma_j)^{\frac{1}{2}} e^{i\phi_j} \right|^2 \quad (2.18)$$

where σ_j and ϕ_j denote the RCS and the phase of the j^{th} component of the complex target, respectively.

Although the relative phase method will predict the RCS of a complex target very closely, determining the phase of each component on a very involved target may prove

difficult, if not impossible. If the phase information is not available or too computationally intensive to obtain, the random phase method is the more advantageous method to use. The random phase method is described mathematically as

$$E[\sigma] = \sum_{j=1}^N \sigma_j \quad (2.19)$$

where $E[\sigma]$ is the expected RCS value.

Note the phase information is not taken into account in equation (2.19). The reason for neglecting the phase terms is that if a complex target has numerous components, the phase terms from each component will average out, assuming the phase terms are randomly and independently distributed. It is important to note that the assumptions behind using equation (2.19) are that the phase terms are independently distributed, that there are large number of scattering centers that the complex target is comprised of, and that the strength of the scattering from each of the components are similar. The random phase method will not yield good results if there are only a few scattering centers of similar strength.

When the random phase method is implemented, the probable deviation due to the phase variation of the components from the expected target RCS can be obtained by using the root mean square (rms) spread. The bounds of the probable deviation within the random phase method lie within the range of

$$E[\sigma] - S \leq \sigma \leq E[\sigma] + S \quad (2.20)$$

where the standard deviation, S , is described as

$$S = \left(\sum_{j=1}^N \sigma_j \right)^2 - \sum_{j=1}^N \sigma_j^2 \quad (2.21)$$

2.4 Effects of Changing Geometries on RCS

In 1986, Beck [5] conducted a study on the effects of aeroelastic wing deformations on wing RCS. Beck described the RCS of the wings with the effects of aeroelastic deformations as a set of functionals as follows

$$\sigma = f(\lambda, \Omega', P_i, P_r, \theta + \alpha_e, \varphi) \quad (2.22)$$

λ is the incident wavelength,

Ω' represents the changed target geometry due to aeroelastic deformations from the original target geometry, Ω .

P_i is the polarization of the incident wave

P_r is the polarization of the reflected wave

θ is the angle of observation in the elevation plane

α_e is the change in elevation angle due to the twisting of the wings

φ is the angle of observation in the azimuth plane

Beck's study and this thesis have an underlying parallel between them. Beck's study investigates a phenomenon which causes uncertainty (aeroelastic deformation) on a target's geometric feature (aircraft wing) and its effect on the RCS of that target feature. This thesis investigates a phenomenon which causes uncertainty on a target's geometric features (incorrect modeling of ballistic missile features) and its effects on the overall RCS of the missile.

Beck's study dealt with 2 types of wing deformations: twisting and bending. The wing that was modeled was the NACA 0015 airfoil in swept and unswept wing configurations. The deformations were evaluated at 5 GHz and 9 GHz in both horizontal and vertical polarization. Beck found that the results of twisting the wing did

affect the RCS but the manner in which it affected the RCS was dependent upon airfoil thickness and the angle of observation. Twisting of the wings caused the wing trailing edge to be “visible over a larger angular area” and “look thicker.”

Beck’s study also concluded that the effect of wing bending on the RCS is strong coupling between RCS and deflections. “Increased speed and reduced stiffness increased RCS above the wing and reduced it below the wing.” Swept wing configurations showed resistance to RCS changes when bending was applied. “Swept back wings showed little change from aeroelastic deformations in the frontal angular aspects tested. Patterns changed but sector averages remained constant.”

Though Beck’s study has found a “rule-of-thumb” for the effects of bending and twisting on the RCS of a wing, what Beck did not address is the effect of the wing on the RCS of an entire target. Beck modeled his wings to be isolated in space. Predicting the effects of wing deformation on more complex targets, such as an aircraft, is much more complicated.

In 1991, McKenzie [6] followed up on Beck’s work by investigating the effects of wing deformation on the RCS of an entire aircraft. The two aircraft that were looked into in McKenzie’s thesis were the T-38 and C-5A. The T-38, a compact jet, was chosen to represent the set of rigid body airframes. The C-5A, a large transport, was chosen to represent a set of large flexible airframes. A program called NASTRAN was used to calculate realistic wing deformations due to structural loading in flight through the use of finite element analysis.

McKenzie’s conclusion was that “the effects can be lumped into basically two categories: (1) variations in the lobing structure of the RCS pattern, or (2) changes in

amplitude of various lobes within the RCS pattern.” McKenzie goes on to explain broadening and narrowing of lobes due to changing edge lengths, constructive/destructive phase interference affecting RCS amplitudes, and changing wing dimensions at differing angular aspects affecting RCS amplitudes. McKenzie goes into great depth describing the changing lobing patterns and differing RCS return strengths. However, McKenzie does not summarize the changes in the RCS patterns to a level where it is easy to note a relationship or correlation between the deformation of the wings and the RCS of the aircraft.

2.5 Analyzing RCS Uncertainty

Other studies have been conducted in the field of RCS uncertainty. Welsh, Muller, and Kent [7] conducted a calibration uncertainty analysis on compact RCS measurement ranges. According to their paper, uncertainty in range measurement can be characterized using the model:

$$E_m = \alpha \frac{E_t + \partial_t}{E_c + \partial_c} E_p \quad (2.23)$$

where

E_p is the calibrated electric field,

α accounts for multiplicative errors in the measurements,

E_t is the error-free target electric field,

∂_t is the additive complex error associated with target measurement,

E_c is the error-free calibration target electric field,

∂_c is the additive complex error associated with calibration measurement and,

E_p is the error free prediction for the calibration target.

The complex additive error terms, ∂_i and ∂_c , are assumed to be circularly complex Gaussian independent random variables, with variances $\langle |\partial_i|^2 \rangle$ and $\langle |\partial_c|^2 \rangle$, respectively. For the multiplicative error term, α , we assume it to be a multiplicative combination of smaller errors such that

$$\alpha = \alpha_1 \alpha_2 \dots \alpha_N \quad (2.24)$$

where α_i is the i^{th} independent multiplicative error term where $i = 1, \dots, N$. Assuming a log normal distribution for $|\alpha_i|^2$, the variance is

$$S^2 = S_1 S_2, \dots, S_N \quad (2.25)$$

Using Taylor-series expansion and assuming $\partial_c/E_t \ll 1$, Welsh [7] derived the following term for uncertainty,

$$U = \frac{\langle |E_m|^2 \rangle}{|E_t^{true}|^2} \pm \sqrt{\text{var} \left(\frac{|E_m|^2}{|E_t^{true}|^2} \right)} \quad (2.26)$$

where

$$E_t^{true} = \frac{E_t E_p}{E_c}. \quad (2.27)$$

Welsh *et.al.* derived a general term for uncertainty in range measurements which bound the error. This term gives us some insight into the behavior of uncertainty. Unlike Welsh *et.al.* [7] who leaves sources of uncertainty in a very general nature, Wittman [8] hones in on potential sources of error which lead to uncertainty. Wittman's claims RCS can be quantified by a statement of uncertainty,

$$\sigma = \sigma_o \pm \Delta\sigma \quad (2.28)$$

The term σ_o is the best estimate of the RCS and $\Delta\sigma$ is the uncertainty associated with the RCS which ends up giving an expression that bounds the measurement error. Whittman [8] makes it a point to note the subtle difference between error and uncertainty. “We distinguish between ‘error’ which is the difference between measured and actual values, and ‘uncertainty,’ which is a bound on what the error might be.” [8] The root sum of squares method is used to calculate the overall uncertainty. Mathematically, the overall uncertainty is written as

$$\left(\frac{\Delta\sigma}{\sigma_o}\right)^2 = \sum_i \left(\frac{\Delta\sigma_i}{\sigma_o}\right)^2 \quad (2.29)$$

where $\Delta\sigma_i$ are components (or sources) of uncertainty. Major sources of uncertainty in RCS measurement that are characterized by Wittman [8] as described in this section.

Average Illumination: If the effective beamwidth, the beam pattern or sidelobe locations are unknown, error will be introduced that may not be accounted for, leading to uncertainty. The ideal illumination in a measurement case is a illuminating beam with a constant planar wavefront with no sidelobes.

Background-Target Interactions: Interactions and multi-bounce from the target and its surroundings will inevitably lead to unwanted returns. The effects of target-background interactions can be alleviated by time gating the data but may not be completely eradicated.

Cross Polarization: The ideal polarization of an antenna in a measurement range would align the electric fields perfectly vertically or horizontally. Due to real life effects, there will always a tilt in the polarization of the antenna leading to errors in measured data.

Drift: Drift is the changing parameter in any radar system as time progresses.

Frequency: Frequency uncertainty is essentially the effective bandwidth of the system. Whittman describes frequency uncertainty as “... the minimum of the transmitted bandwidth and received bandwidth.” Usually, frequency uncertainty is negligible in the monostatic case since the transmitting and receiving antennas are the same. Uncertainty due to frequency is

$$\Delta\sigma(dB) = -20\log\left(1 - \frac{\Delta f}{f}\right) \quad (2.30)$$

Integration (Moving Target): Target motion will introduce uncertainty into the RCS. If a target is moving too fast and integration is performed on the target returns, the result of the integrations will be a sum of returns from a range of angles rather than at one point. In the static measurement case, the integration uncertainty can be controlled by slowing target rotation during measurement or stopping it altogether.

I-Q Imbalance: If the I-Q channels in the radar system are not perfectly 90° out of phase or the amplitudes are not the same magnitude, there will be error introduced leading to uncertainty.

Near Field: When measuring RCS, we always assume a far field measurement. A far field measurement implies that the target is illuminated by a planar wave originating from a point source. Realistically, when the source is close to the target, the outer envelope of the illuminating wave will be slightly curved, leading to near field uncertainty.

Noise-Background: Noise-background errors are caused by clutter and stray electrical signals from the environment. Integration techniques and background subtraction help mitigate the uncertainty associated with noise-background errors. For a

signal power level of S and a noise power level of N, the noise-background uncertainty can be characterized as:

$$\Delta\sigma(dB) = -20\log\left(1 - 10^{-\varepsilon_n/20}\right) \quad (2.31)$$

where $\varepsilon_n = 20\log(S/N)$.

Target Orientation: Errors due to target orientation are significant for electrically large objects. When a target is placed on a pedestal in an RCS range, the slightest tilt or nudge from the desired angle will result in errors. If θ is the respective angular variable, the uncertainty due to target orientation can be written as:

$$\Delta\sigma(dB) = -10\log\left(1 - \frac{\partial\sigma}{\partial\theta} \frac{\Delta\theta}{\sigma}\right) \quad (2.32)$$

Even though uncertainty in Welsh's and Whittman's studies pertain to range measurement uncertainty rather than uncertainty in target geometry (as in this thesis), their studies allow a better understanding of the nature of uncertainty and how any variation or change within measurement variables can affect the RCS of the target; analogous to how variations in missile components affect the RCS of the entire missile.

2.6 Evaluation of RCS at High Frequencies

To evaluate the RCS of targets for this thesis, XPatch was utilized. XPatch was developed by SAIC-Demaco under the sponsorship of the Air Force Research Laboratory. XPatch computes the RCS of arbitrarily shaped impenetrable targets using the physical optics (PO) equivalent currents on the surface of the target radiating in free space. These equivalent currents are obtained by shooting a grid of small ray tubes at the

target. Each ray tube is tracked through multiple reflections on the surface of the target according to the rules of geometrical optics. At each reflection point the intersection of the ray-tube with the surface defines a “footprint” of PO currents which are integrated and summed to give the total RCS.

The assumption behind physical optics is that the illuminated target is so large that any surface that is hit by the incoming wave sees the surface of the target as a flat plane. The frequencies of interest for this thesis lie in the X-band, which ranges from 8.5 GHz to 10.5 GHz, and the L-S band, which ranges from 1.5 GHz to 3.5 GHz. When the wavelength, λ , is at least an order of magnitude smaller than the target of interest or any of its features, high frequency asymptotic techniques can be used to approximate the RCS of the target. X-band waves illuminating a target as large as an intercontinental ballistic missile certainly satisfy this criterion.

Using the assumption that the target is much greater than the wavelength of the illuminating wave, we can use the PO approximation of the induced surface currents by:

$$\bar{J}_s = 2\hat{n} \times \bar{H}^i \quad (2.33)$$

where \bar{J}_s is the surface current induced by the incoming wave, \hat{n} is the unit normal vector to the surface of the target, and \bar{H}^i is the incident magnetic field.

The induced currents will radiate a field that can be found by integrating around the surface body.

$$\bar{E}_s = \frac{-j\omega\mu}{4\pi r} e^{-j\beta_0 r} \iint_s \hat{e} \cdot \bar{J}_s e^{j\beta_0 \hat{r} \cdot \bar{r}'} ds \quad (2.34)$$

where

\hat{e} is the unit polarization vector of the transmitted energy,

μ is the permeability of the medium the wave is traveling through,

ω is the angular frequency,

β_o is the wave number,

r is the distance from the target to the radar,

\hat{r} is the unit vector pointing towards the receiver and

\vec{r}' is the position vector of the target.

The scattered electric field can in turn be used to compute the RCS of the target through equation (2.1). The PO approximation works very well for signatures dominated by specular returns. However, to account for diffraction and other second order effects, such as traveling waves, additional mathematics must be introduced. Edge diffraction has been taken into account in XPatch but not in the Crispin and Siegel formulas.

2.7 Data Reduction and Presentation Techniques

Many times, overwhelming amounts of data keep us from seeing the “big picture” or a general trend. “If a domain of RCS data is to be represented by a single (or a few) statistic(s) (such as the average or median), then the choice of these statistics should be determined by the situation or system in which these RCS data are used.” [4] This study does not require knowledge of the RCS pattern down to each oscillation. The following methods can help reduce the amount of RCS data and organize it in a meaningful way.

Angular Smoothing: Angular smoothing is one of the widest used smoothing techniques. It is used in windowing sector averages to remove rapid oscillations in a RCS curve that occur due to angle dependence. This way, the RCS dependence on other param can be seen more easily. In the case of a body of revolution (such as a ballistic

missile), the angular sector averaged RCS, $A(\sigma)$, as a function of elevation, θ , off the symmetry axis can be given as

$$A(\sigma) = \int \sigma(\theta) d\theta \quad (2.35)$$

Phase Smoothing: A form of phase smoothing has already been introduced in equation (2.19). The method of random phase is a form of phase smoothing where violent oscillations within the RCS curve due to some phase relation are smoothed out by averaging out the phase. This averaging is done on the assumption that the phases are randomly and independently distributed amongst a large number of scatterers.

Cumulative Distribution Function (CDF): Unlike the previously mentioned averaging techniques, the nature of the oscillations within a RCS plot can be captured using a CDF. The CDF is a number between 0 and 1 denoting the fraction of total values given below a certain RCS value, σ . Mathematically,

$$CDF(\sigma) = \int_{-\infty}^{\sigma} PDF(\sigma) d\sigma \quad (2.36)$$

where $PDF(\sigma)$ denotes the probability distribution function.

By comparing the distribution as a function of RCS, not only is the difference in the mean and medians apparent, but other quantitative distribution information about the RCS data (range of RCS values, strength of oscillations, *etc*) rather than a single statistic are also apparent.

3 Methodology

This chapter will provide a detailed description of the methods and processes used to obtain the results that will be presented in Chapter 4. This thesis is composed of two major data sets. The first data set was obtained through XPatch simulations. There will be 36 different missile configurations modeled as facet files, evaluated in XPatch and compared to obtain a parametric relationship between target features and radar signature. The C&S dataset will be an evaluation of only 9 of the total 36 configurations in a more mathematically predictive nature utilizing the works of Crispin and Siegel [2] for analyzing the RCS of complex targets at high frequencies as an effort to validate the results we obtain from the XPatch parametric study. Only 9 configurations are evaluated in the C&S dataset because of the limitations of the C&S approximations on certain configurations.

3.1 *Target Geometry*

Every missile configuration investigated in this study has a variation on each of the following components:

Nosecone: NASIC/ADNS is interested in 3 types of nosecone configurations. The first nosecone configuration is a simple cone with a half angle of 11° and a base radius of 0.64 m. The point of the cone is rounded off into a spheroid of radius 0.075 m. The total length of the nosecone is 3 m. The simple nosecone is given in Figure 3-1.

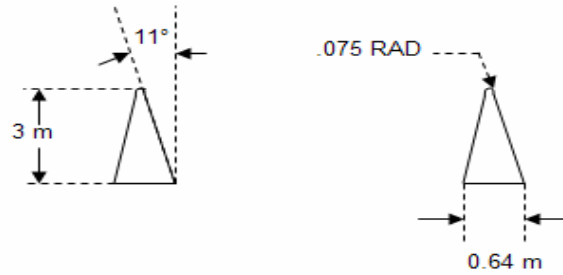


Figure 3-1: Diagram of the simple conic nosecone.

The second nosecone configuration is a bi-conic nosecone. Like the simple nosecone, the base radius is 0.64 m, the length of the nosecone is 3 m, and the point is rounded into a 0.075 m spheroid. The base of the cone is angled at a half angle of 10° up to a height of 1.6 m. The conic shape of the nosecone then changes to a half angle of 12° for the remaining 1.4 m until it comes to a rounded point. The bi-conic nosecone is shown in Figure 3-2.

The third nosecone configuration is a “broken” nosecone. The conic shape of the nosecone is “broken” by a cylinder with a diameter of 0.525 m and a length of 1 m. The base is comprised of a truncated cone with a half angle of 21° and a base radius of 0.64 m. The base extends to a height of 1 m and connects to one end of the sandwiched cylinder. The other end of the cylinder forms the base of a cone with a half angle of 11° and forms the tip of the missile. Once again, the tip of the missile is rounded off to

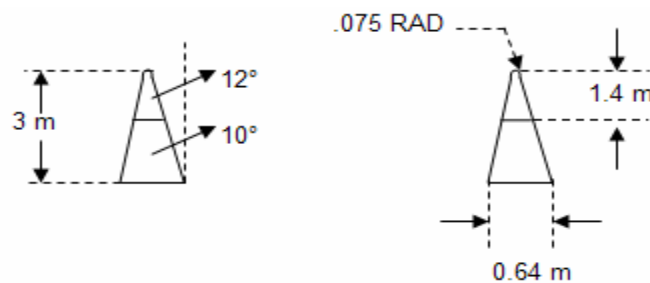


Figure 3-2: Diagram of the bi-conic nosecone

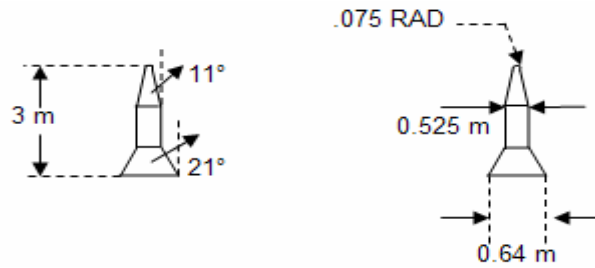


Figure 3-3: Diagram of the “broken” nosecone.

become a spheroid. The length of the entire nosecone is 3 m. The broken nosecone is shown in Figure 3-3.

Fins: The combinations for fin variation on a ballistic missile are infinite. In order to finish this thesis in a timely manner, only two fin geometries are considered. The first fin geometry is a fin with a length of 1.025 m along the side of the missile. The base of the fin has a 0.32 m width. A .45 m edge runs parallel to 1.025 m side and the ends of both edges are connected by 31° angled edge as shown in Figure 3-4. The second fin geometry is exactly the same as the first fin geometry except that every dimension in the fin geometry is doubled, as shown in Figure 3-4. Since the only difference between the two fins are their dimensions, the 1.025 m fin and the 2.05 m fin will be called the “small” and “large” fins, respectively.

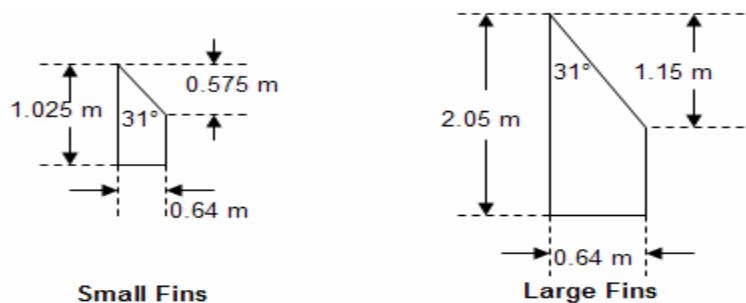


Figure 3-4: Diagram of the ‘small’ (left) and ‘large’ (right) fin configurations.

Fins are not present in many ballistic missiles. In order to account for the family of ballistic missiles where fins are not present in the geometry, a missile with no fins will be considered the third fin configuration. Thus there are 3 fin configurations in total: the large fin case, the small fin case, and the finless case.

Heat Shields: Target models are most commonly and easily modeled as perfect electric conductors (PEC). Any other material other than metals will add material properties to the target. Heat shielding on the nosecone portion of a missile is not an exception. Heat shielding is used to protect the RV containing the warhead of the missile from excess heat during re-entry into the earth's atmosphere from space. From a signatures assessment standpoint, heat shielding will absorb radar energy resulting in lower RCS returns. Heat shielding will also affect phase interactions resulting in an altered lobing pattern compared to a purely PEC case. This thesis will investigate only one material coating used for heat shielding, the asbestos phenolic. The material properties of the asbestos phenolic were modeled with a relative permittivity of $\epsilon_r = 5 - 0.5j$ and a relative permeability of $\mu_r = 1$. The asbestos phenolic will be applied as a PEC-backed 10 mm-thick coating surrounding the nosecone of the missile. As far as heat shielding on the nosecone is concerned, there are two configurations: heat shielding present and heat shielding not present (pure PEC nosecone).

Panels: As mentioned previously in chapter 1, NASIC/ADNS is interested in the effects of panels and rivets on the signature of a ballistic missile. Three panels were modeled along the side of the missile. The first panel had a 1 m length along the missile axis, a width of 0.7 m and placed 2 m from the flat end of the missile. The second panel has a 1 m length along the missile axis, a width of 0.7 m and placed 7.75 m from the flat

end of the missile. The third panel of 0.5 x 0.5 m was placed on the RV section of the nosecone. The grooves separating the panels from the body of the missile are 3 mm wide. The dimensions of the rivets holding the panels down are modeled as cylinders with a 7.5 mm radius and a height of 4 mm. The rivets were spaced no more than 15 mm apart from each other and placed 1 to 2 cm away from the panel grooves. Approximately 550 rivets were modeled on the three separate panels shown in Figure 3-5.

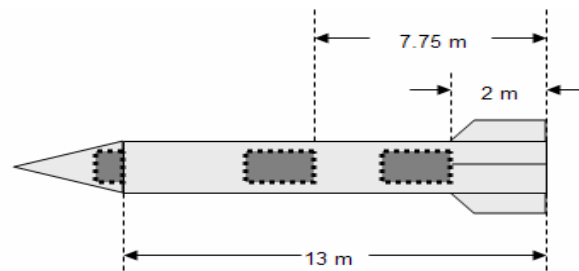


Figure 3-5: Diagram of panel and rivet placement on the generic ballistic missile.

In XPatch, the panels can be modeled through the use of incremental length diffraction coefficients (ILDCs). ILDCs are used for modeling target features that are much smaller than a wavelength through the use of equivalent currents. The largest dimension of the rivets is 15 mm, which is half the wavelength of the highest frequency of 10.5 GHz. Therefore the use of ILDCs to model the rivets is well justified.

Body: The “body” of the missile refers to the 13 m long cylinder with a radius of 0.64 m. The dimensions of this cylindrical body do not vary throughout the 36 missile configurations. One end of the cylinder is connected to the circular base of the nosecone and the other end is a circular flat plate.

Raceway: The raceway of the missile can be described as a long “rod” that runs across the side of the missile. The raceway of the generic missile can be clearly seen in

Figure 1-1. Its purpose is to hold and protect the wires and cables which connect the head of the missile to the rocket motors allowing guidance and navigation. The raceway of the missile was modeled on the opposite side of the panels so that the RCS returns of both components could be isolated for analysis purposes. The raceway runs 9.4 m alongside the missile at a height of 0.1m. Each end of the raceway is beveled at a 30° angle to the missile body. The dimensions of the raceway remain the same in each missile configuration.

By combining every variation of the 6 missile components, 36 different missile configurations were generated. Table 3-1 lists the 36 missile configurations and the combination of components which make up each configuration.

Table 3-1. Table of missile configurations

Configuration	Nosecone Type	Fin Type	Paneling	Heat Shielding
01	Simple Conic	None	Absent	Absent
02	Simple Conic	None	Absent	Present
03	Simple Conic	None	Present	Absent
04	Simple Conic	None	Present	Present
05	Simple Conic	Small	Absent	Absent
06	Simple Conic	Small	Absent	Present
07	Simple Conic	Small	Present	Absent
08	Simple Conic	Small	Present	Present
09	Simple Conic	Large	Absent	Absent
10	Simple Conic	Large	Absent	Present
11	Simple Conic	Large	Present	Absent
12	Simple Conic	Large	Present	Present
13	Bi-conic	None	Absent	Absent
14	Bi-conic	None	Absent	Present
15	Bi-conic	None	Present	Absent
16	Bi-conic	None	Present	Present
17	Bi-conic	Small	Absent	Absent
18	Bi-conic	Small	Absent	Present
19	Bi-conic	Small	Present	Absent
20	Bi-conic	Small	Present	Present
21	Bi-conic	Large	Absent	Absent
22	Bi-conic	Large	Absent	Present

23	Bi-conic	Large	Present	Absent
24	Bi-conic	Large	Present	Present
25	Broken	None	Absent	Absent
26	Broken	None	Absent	Present
27	Broken	None	Present	Absent
28	Broken	None	Present	Present
29	Broken	Small	Absent	Absent
30	Broken	Small	Absent	Present
31	Broken	Small	Present	Absent
32	Broken	Small	Present	Present
33	Broken	Large	Absent	Absent
34	Broken	Large	Absent	Present
35	Broken	Large	Present	Absent
36	Broken	Large	Present	Present

3.2 XPatch Data Collection

NASIC/ADNS provided facet files of every variation of the missile components mentioned in section 3.1. Facet files are files with a listing of coordinates and node combinations that are representative of a desired geometry. Each node combination represents a flat PEC facet on the target geometry. Each facet is arranged so that as a whole, the facet arrangement models the desired target geometry. The facet files of different components were merged in different combinations to create full-missile representations of the 36 missile variations listed in Table 3-1.

Using the cifer utility tool in XPatch, the nodes of the full-missile facet files were consolidated at a 0.0001 mm spacing tolerance. Consolidating nodes reduces the number of redundant nodes that exist in a facet file that have no impact on RCS evaluation. Consolidation also reduces the memory size of the facet files and allows the edge extraction feature in XPatch give less erroneous results. The edge extraction feature in



Figure 3-6: Screenshot of a missile facet file (blue) along with its corresponding extracted edges (black) viewed in XPatch.

XPatch can be accessed through the cifer utilities as well. Edge extraction allows XPatch users to account for diffractive effects from sharp wedge discontinuities that can't be accounted for using the PO approximations allowing an extra level of accuracy to the true solution. The maximum interior wedge angle for edge extraction was set to the recommended 120° by the cifer utility. Edges were extracted from the ends of the missile body, corners of the raceway, edges of the fins, and discontinuities in the nosecones, as shown in Figure 3-6.

After consolidation and edge extraction were completed, a ray absorber was placed inside the PEC surface of the missile geometry. A ray absorber essentially nulls any illuminating ray that touches it and always gives an RCS return of 0 m^2 . The ray absorber was used to deal with the problem of leaking rays. Leaking rays are rays that travel in between facets where they are not supposed to go and may get trapped inside the

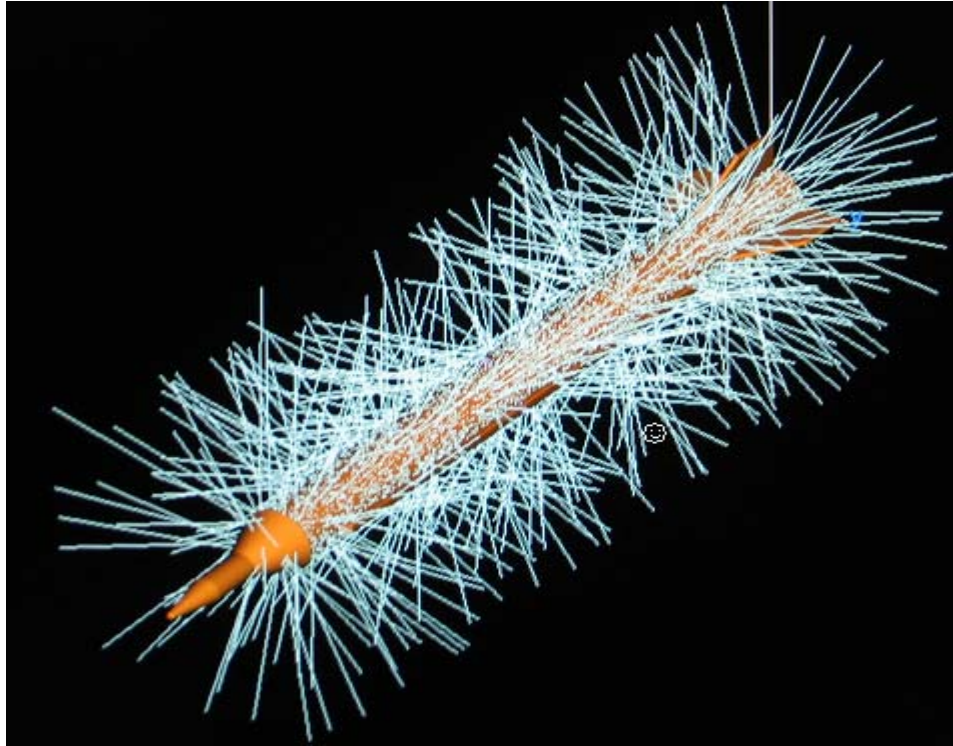


Figure 3-7: The effects of leaking rays in XPatch.

geometry. These rays may bounce around inside the target geometry, greatly lengthening the runtime of XPatch, or they may escape and contribute RCS returns where they shouldn't. In XPatch a transmitter was placed within the missile facet geometry and the leaking rays (white) can clearly be seen in Figure 3-7.

The facet files and the corresponding input scripts (or input pages) were entered into XPatch for RCS evaluation. An example of a XPatch input page is shown in Appendix A. The azimuth angles were swept from 0° to 360° in 1° increments. The elevation angles were swept from 0° to 15° in 3° increments. Two bands of frequencies were evaluated at the request of NASIC/ADNS: one in X band (8.5 to 10.5 GHz) and the other in L-S band (1.5 to 3.5 GHz). In each 2 GHz bandwidth, 32 equally spaced frequencies were evaluated in order to capture the RCS variations due to frequency. The

results that XPatch produced were *.rcs files which were then converted into *.mat files for data analysis using MATLAB.

3.3 Data Reduction and Missile Comparison for XPatch Data

This section will only outline the methodology for efficiently comparing RCS plots. A discussion of individual peaks in each plot and what the differences mean will be discussed in Chapter 4. In order to investigate the effects of a single variable missile feature on the RCS, two missile configurations that will be compared must differ by that one variable feature while all other target features remain fixed. In other words, by varying each of the four target features and comparing one configuration to another, a relationship between specific target features and its effect on the RCS of a ballistic missile can be obtained. Even though only a single variable feature is compared at a time, every possible combination of components must be investigated in the event that interactions with other variable target features affect the overall target RCS.

Though this may sound easy at first, the sheer volume of raw data makes this a formidable task. There are five dimensions of RCS data: azimuth, elevation, frequency (or wavelength), polarization and missile configuration, which can be represented mathematically as

$$\sigma = f(\varphi, \theta, \lambda, p, K) \quad (3.1)$$

In order to reach a conclusion in a concise and organized fashion, the way in which the raw data was handled had to be well planned. Too much averaging and data consolidation will result in loss of information. Too little averaging or consolidating will result in being overwhelmed with RCS data.

The first step in data reduction was to average out the 32 different frequencies in each of the 2GHz frequency bands. For a given polarization, configuration, azimuth and elevation, the RCS data predicted at each of the 32 frequencies in both the X band and the L-S band were arithmetically averaged to characterize the frequency band. Equation (3.1) is now transformed to

$$\sigma_{\lambda_{avg}} = f(\varphi, \theta, p, K) \quad (3.2)$$

Figure 3-8 plot the RCS of the 33 missile configuration in color at all 32 frequencies at X band in VV polarization at an elevation of $\theta = 15^\circ$. The arithmetic mean and the bounds of two arithmetic standard deviations above and below the mean are plotted over all 32 frequencies to serve as an illustration of how well the averaged result characterizes the whole frequency band. The difference in dBsm between the upper and lower two standard deviation bounds (in which 95% of the data falls) is shown in Figure 3-9. The average difference between the 2 standard deviation bounds across azimuth is 6.9 dBsm. Because NASIC/ADNS is willing to tolerate up to a 10 dBsm induced uncertainty in RCS resulting from averaging, the use of frequency averaging is well justified. Similar results are obtained for HH- polarization and in all other missile configurations.

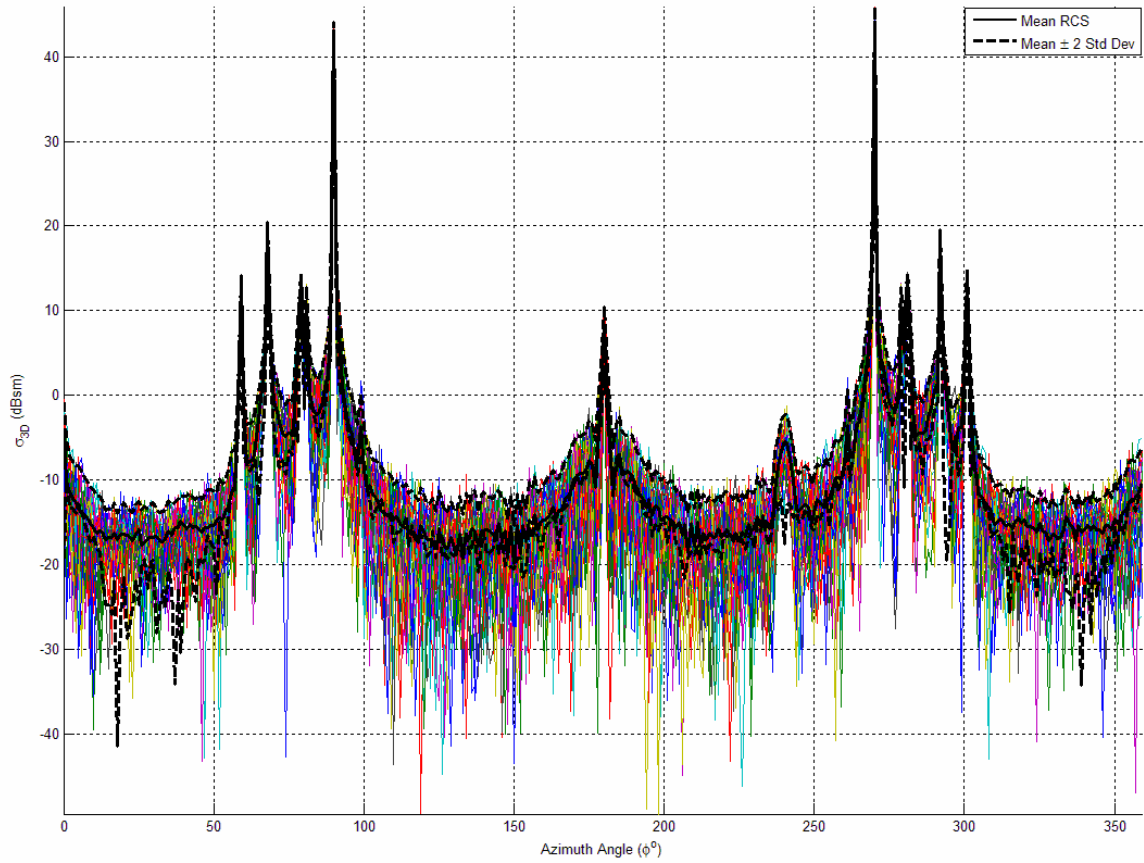


Figure 3-8: Mean RCS and 2 standard deviation bounds of 32 X-band frequencies plotted over each individual frequency (colored) in VV polarization at $\theta = 15^\circ$

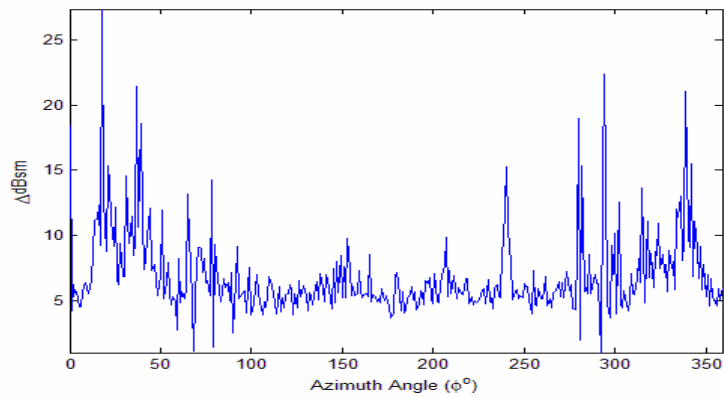


Figure 3-9: Difference between 2 standard deviation upper bound and lower bound of the 32 X band frequency RCS plots in VV polarization at $\theta = 15^\circ$.

In order to investigate the effect of changing or adding a specific component on a missile, two missile configurations that differ only by that particular component are analyzed side by side. By subtracting the RCS of one configuration from the other, the “effect” can be quantified as a difference plot. The subtraction itself can be done arithmetically in m^2 or geometrically on a log scale in $\Delta dBsm$. The difference was decided to be quantified in $\Delta dBsm$ for two reasons. The first reason is that RCS data is always plotted in $dBsm$ units. By comparing differences in $\Delta dBsm$, one can immediately see the angular regions that are most sensitive to change in missile configuration. The arithmetic RCS difference may be small yet it may make a huge impact on a log scale RCS plot. The second reason is that a numerical RCS difference would not show enough variation for a meaningful analysis. For example, Figure 3-10 illustrates the arithmetic RCS values for a finless and small fin missile configuration. Hardly any variation is seen between the two arithmetic RCS plots to make any comparison, even though intuitively, one would expect a great variation on a log scale RCS plot. Even if the difference was converted back into a log scale, the conversion would be almost meaningless because it is not easily comparable to the original RCS plots of the two missiles.

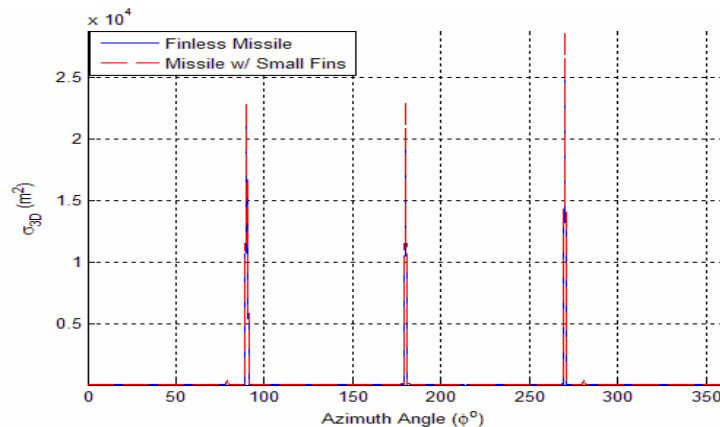


Figure 3-10: Arithmetic RCS of finless missile configuration and small fin missile configuration.

In order to reduce the data further we refer to Figure 3-11, which compares the frequency averaged RCS returns between the 01 missile configuration and the 13 missile configuration over six elevation angles. The frequency is X band in HH polarization. The dBsm difference between the two configurations is plotted in red. Each RCS plot at a given elevation angle is offset from the plot at the next elevation angle by 50 dBsm. The 01 and the 13 missile configuration differ in nosecones. The 01 configuration has a simple conic nosecone whereas the 13 configuration has a bi-conic nosecone. Because the RCS of the nosecones do not vary as a function of elevation as long as azimuth is fixed, the difference plots remain fairly consistent across elevation, even though the RCS of the two missile configurations are significantly changing. The difference plots at every elevation remain close to a 0 Δ dBsm difference except in the immediate vicinity of $\phi = \pm 79^\circ$. Figure 3-11 serves as an illustration of the best case scenario in terms of consistency of the difference plots across elevation angles. Consistent difference plots across elevation are observed for other nosecone combinations, heat shields and panels as well. Averaging the difference plots across elevation is well justified in every one of these cases.

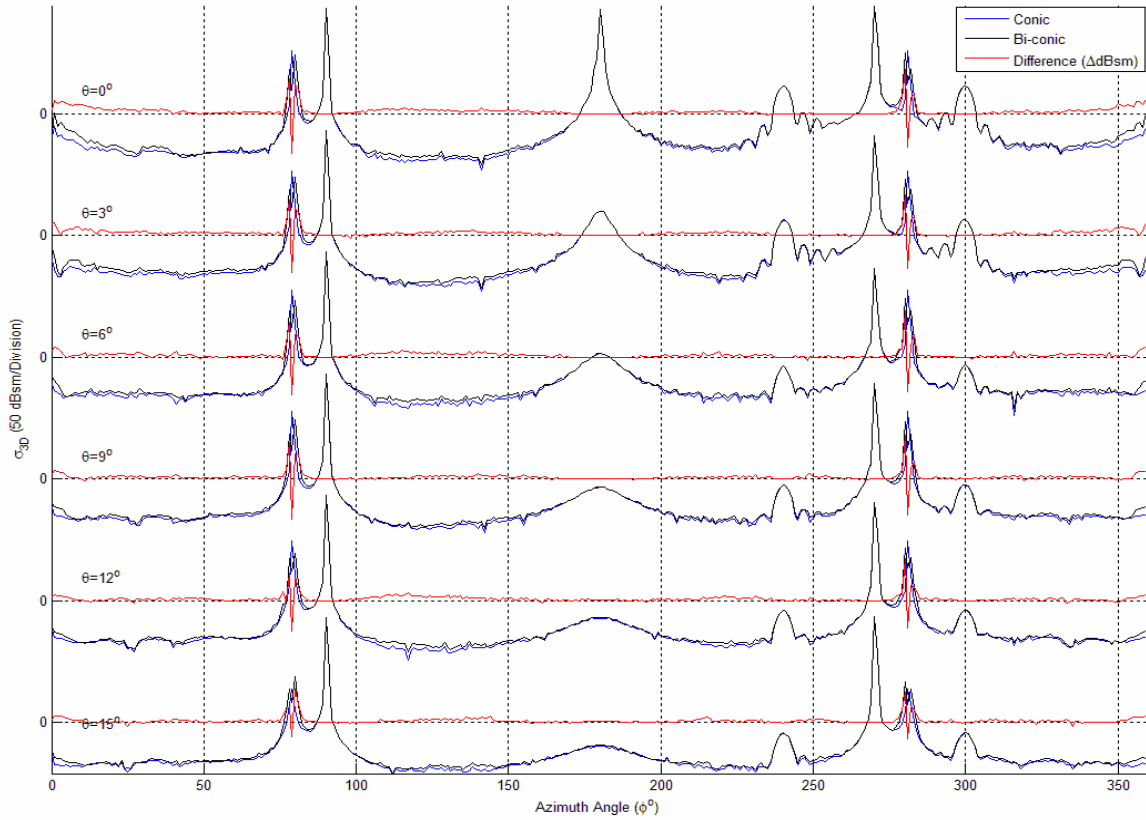


Figure 3-11: C&S RCS comparison between simple conic and bi-conic nosecone missile configurations over elevation in X-band at HH polarization.

Figure 3-12 compares the 01 configuration to the 05 configuration over elevation. The frequency is X band in VV polarization. The 01 configuration is finless whereas the 05 configuration has a set of small fins. As Figure 3-11 served as an illustration of the best case scenario for consistency of difference plots over elevation, Figure 3-12 serves as an illustration of the worst case. The difference plots remain fairly consistent across elevation except at $\theta = 0^\circ$. Only at waterline, $\theta = 0^\circ$, is the RCS difference plot in the non specular regions for $100^\circ \leq \varphi \leq 260^\circ$ is on the order of 15 dBsm after the introduction of the fins. Other fin variations yielded similar results. Despite this discrepancy at $\theta = 0^\circ$, the difference plots for fin comparison at the other elevations are similar enough to

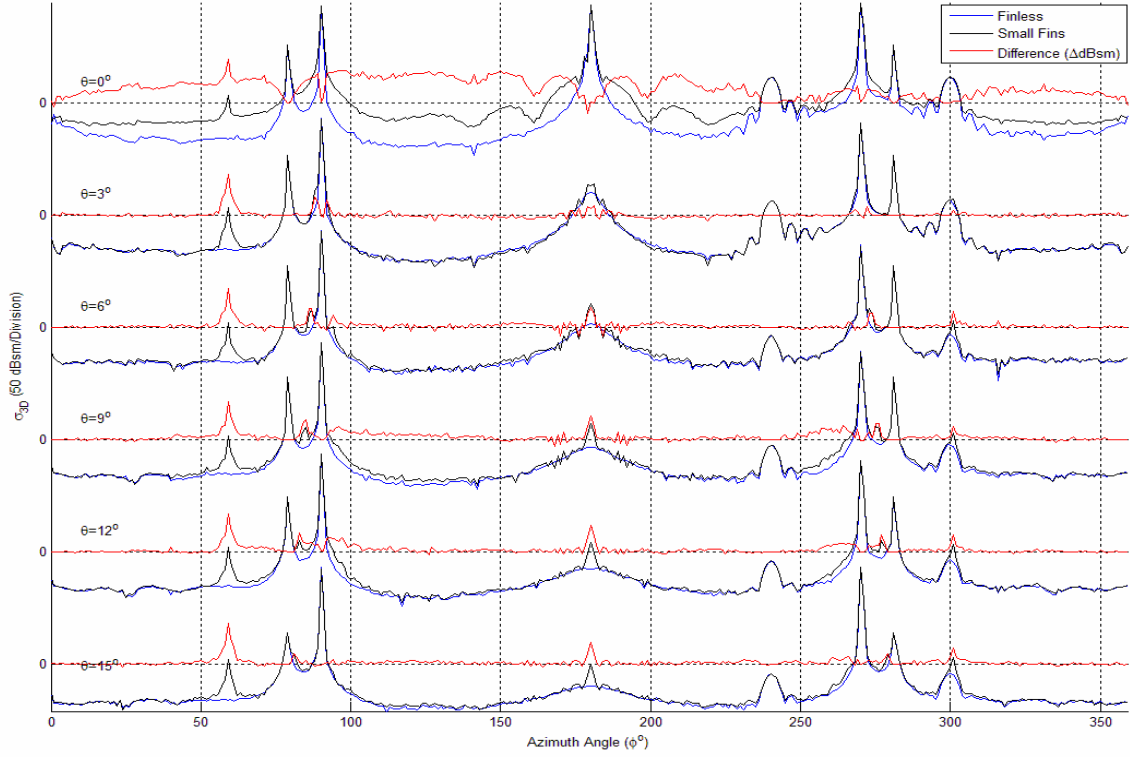


Figure 3-12: XPatch RCS comparison between finless and small fin missile configurations over elevation in X band at VV polarization.

average over elevation and obtain a result in which we can be confident. The result of averaging the difference plots over elevation can be written

$$\Delta\sigma_{\lambda_{avg}, \theta_{avg}} = f(\varphi, p, K) \quad (3.3)$$

Not only are the difference plots over elevation similar, but over families of configurations as well. The difference plots comparing finless missile configurations to large fin configurations have similar difference plots as shown in Figure 3-13. The same relationship is valid for configurations comparing nosecones, panels, heat shields, and other fin configurations. Because of difference plot similarities when two sets of missile configurations are comparing the same missile component, averaging over sets of configuration comparisons are well justified. For example, averaging the difference plots of finless missile configurations vs. large fin configurations would be achieved by

averaging the 12 difference plots generated by subtracting the returns of missile configurations 01, 02, 03, 04, 13, 14, 15, 16, 25, 26, 27, and 28 from configurations 09, 10, 11, 12, 21, 22, 23, 24, 33, 34, 35, and 36; respectively. Each of the 12 difference plots would then be averaged into one difference plot representing all configuration possibilities for a particular component. In essence, the difference plot has been averaged over configuration. The final functional form used for the parametric study data comparison in Chapter 4 will be

$$\Delta\sigma_{\lambda_{avg}, \theta_{avg}, K_{avg}} = f(\varphi, p) \quad (3.4)$$

Henceforth, the term ‘difference plot’ will refer to equation (3.4) unless otherwise stated. For a difference plot comparing one configuration against another, a positive value corresponds to an increase in RCS if that configuration were to change to the other configuration and a negative value corresponds to a decrease in RCS.

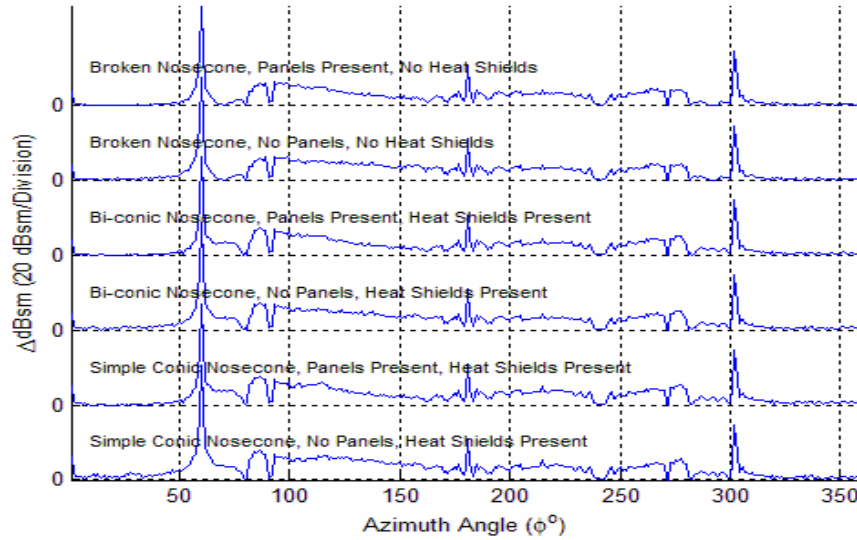


Figure 3-13: XPatch difference plots of finless missile configurations vs. large fin missile configurations plotted over varied configurations.

3.4 Comparing Missile Configurations Utilizing C&S Formulations

The analytical method used in this thesis borrows heavily from the works of Crispin and Siegel (C&S) [2]. The C&S formulations for simple shapes have been discussed in section 2.2. By using the C&S formulas to approximate the RCS of simple shapes and then combining the RCS returns, a close estimate for the RCS of a complex target can be obtained. Methods of combining RCS returns have been introduced in section 2.3. The method that will be used to combine RCS returns in this thesis will be the random phase method, described by equation (2.19).

3.4.1 Modeling Missile Configurations Using C&S Formulations

Every component of the missile body, except heat shields and panels, were approximated with a combination of simple shapes. The heat shields and panels were not modeled using the C&S formulas due to their limitations to be discussed in section 3.4.2

Cylindrical Body: The main body of the cylindrical cylinder was modeled as a 13 m long cylinder with a radius of 0.64 m. The RCS of the cylinder can be approximated with equation (2.14). The flat end of the missile was modeled as a flat circular plate with a radius of 0.64 m through the use of equation (2.17). The cylinder makes signature contributions to the missile RCS in the $60^\circ < \varphi < 300^\circ$ region.

Raceway: In XPatch, the raceway was modeled as a cross between a rectangular prism and a cylinder where the sides were flat but the corners and edges were rounded. In order to make the best estimate in the C&S approximations, the raceway that lies parallel to the missile body was modeled as a cylinder with a length of 9.4 m using

equation (2.14). The flat 30° beveled edges were modeled as flat square plates with 0.14 m sides. Though beveled square plates at the end of a cylinder do not make geometric sense, it gives a good signature approximation at that region. The raceway makes signature contributions to the missile RCS in the $180 < \varphi < 360^\circ$ region.

Simple Conic Nosecone: The simple conic nosecone is easily modeled as a circular cone with an 11° half angle, 3 m length and a base radius of 0.64 m. The RCS of the cone was approximated by equations (2.11) and (2.12). The simple conic nosecone makes significant signature contributions to the missile RCS in the $\varphi < |90^\circ|$ region.

Bi-conic Nosecone: The bi-conic nosecone is composed of two simple shapes. The tip of the nosecone was modeled as a circular cone with a half angle of 12° , a circular base with a 0.43 m radius and a nosecone length of 1.4 m. The base of the missile was modeled as a truncated cone with a length of 1.6 m, a circular base of 0.64 m and circular roof of 0.43 m. The bi-conic nosecone makes significant signature contributions to the missile RCS in the $\varphi < |90^\circ|$ region.

Broken Nosecone: The broken nosecone was composed of three simple shapes. The nosecone tip was modeled as a circular cone with a half angle of 11° , a 0.525 m diameter circular base, and a length of 1 m. The base of the tip is connected to a 1 m long cylinder with a diameter of 0.525 m. The other end of the cylinder is connected to a truncated cone with a length of 1 m, a circular base of 0.64 m and circular roof with a diameter of 0.525 m. The broken nosecone makes significant signature contributions to the missile RCS in the $\varphi < |90^\circ|$ region.

Large Fins: The fins were modeled as a series of flat plates. The surfaces of the fins were modeled as a flat plate with a height of 0.51 m and a length of 1.5 m using

equation (2.16). The fin edge parallel to the body of the missile was modeled as a thin $0.2 \text{ m} \times 0.9 \text{ m}$ strip and the fin edge perpendicular to the body of the missile was modeled as a thin $0.2 \text{ m} \times 0.7 \text{ m}$ strip. The edge that is angled 31° against the body of the missile was modeled as a $2 \text{ m} \times 1.34 \text{ m}$ strip. The fins make significant signature contributions to the missile RCS over every azimuth angle.

Small Fins: Small fins were modeled the same way as the large fins except the dimensions were halved.

The RCS of each missile component was modeled and added non-coherently using MATLAB. The MATLAB code used to compute the component RCS and overall missile RCS is shown in Appendix B.

With the random phase method of combining the RCS signatures of missile components, seeing the potential effects of taking away a missile component and replacing that component with another on the overall signature is more intuitive than in the XPatch parametric study. Applying equation (2.19), the expected RCS of an entire missile configuration can be written as follows:

$$E[\sigma_{\text{Missile}}] = \sigma_{\text{Body}} + \sigma_{\text{Raceway}} + \sigma_{\text{Nosecone}} + \sigma_{\text{Fins}} \quad (3.5)$$

In order to conduct an analytical study that parallels the XPatch parametric study, the same data sets must be obtained. Recall that the 32 frequencies in both the X band and the L-S band were first averaged in order to characterize RCS of a missile configuration over the entire frequency band as shown in equation (3.2). The same was done with the RCS dataset produced with the C&S formulas. The frequency-averaged RCS datasets were subtracted from comparative missile configurations to produce difference plots as described in equation (3.4). The difference plots were then averaged

over elevation and configuration, as in the parametric study, which is represented in equation (3.4), in order to be compared against each other.

3.4.2 Limitations of Approximating Complex Targets

The combination of the C&S formulas and the random phase method are a powerful tool in estimating the RCS of a complex target. However, in order to implement the formulations successfully, one must understand their limitations.

The first limitation is that the C&S formulas have been derived using asymptotic techniques to calculate the RCS of a simple shape. These asymptotic techniques do not account for second order electromagnetic effects such as diffraction, traveling waves and creeping waves. Realistically, second order effects are always present. They have much lower returns than specular returns but may have significant impact on the RCS plots in regions of low return.

The second limitation is that the method of random phase does not account for interactions between components. The assumption behind using the method of random phase is that the illuminating ray hits the target no more than once. The method of random phase merely adds the returns of the components together. Targets with features that cause multiple ray bounces before returning to the radar (*e.g.* corner reflectors) are not well approximated using this method. Adding the RCS of two separate flat plates at $+45^\circ$ and -45° will not give a good approximation of a 90° dihedral.

The third limitation is that when combining the RCS simple shapes using the C&S formulas, polarization cannot be taken into account. The formulas in section 2.2 were derived for a certain polarization at a certain orientation (usually at VV

polarization). When simple shapes are reoriented from the original coordinate axis and combined with other shapes in different free space orientations, polarization becomes somewhat meaningless. Only a general estimate of RCS strength independent of polarization can be obtained for a complex target.

Another limitation of the C&S formulas is that the target should be at least five to ten times larger than the wavelength, because they were derived using optics approximations. This five to ten wavelength criteria is not a hard set rule but rather a general rule of thumb and can somewhat flexed. The longest wavelength dealt with in this thesis is 0.2 m associated with 1.5 GHz. This means that the dimensions dealt with in this thesis should be at least 1 m in order for the C&S approximations to hold well. Unfortunately, there are certain portions of the missile that do not meet this requirement. The edges of the small fins and raceway are 0.1 m and the edges of the large fins are 0.2 m thick. Fortunately, dimensions of the missile body are so large that the second order effects from the fin and raceway edges are dominated by the returns from the missile body.

The final limitation is that the C&S formulas in section 2.2 assume the targets are PEC. The C&S formulas do not account for materials properties other than PEC. Due to these limitations, paneling and heat shielding on the missile cannot be accounted for through C&S formulas. Heat shielding cannot be modeled because it deals with materials other than PEC. Paneling cannot be correctly modeled because the rivets on the panels are smaller than or on the order of the wavelengths used in this thesis. The shortest wavelength dealt with in this thesis is 0.03 m at 10.5 GHz. The dimensions of the rivets on the panels have a diameter of 15 mm and a height of 4 mm, smaller than the

wavelength at 10.5 GHz and beyond the bounds in which the C&S formulas apply. The rivets are also closely spaced together and number approximately 550. Multiple panel rivets closely aligned are bound to have numerous interactions with each other. The nosecones and fins are the only variable missile components that will be investigated through the use of the C&S formulas.

4 Analysis and Results

4.1 *Analysis on the Effects of Nosecones*

This section will investigate the effects of varying nosecones on the RCS of a generic ballistic missile. The three nosecone configurations will be compared in the following order: simple conic vs. bi-conic nosecone configurations in section 4.1.1, simple conic vs. broken nosecone configurations in section 4.1.2, and bi-conic vs. broken nosecone configurations in section 4.1.3. Section 4.1.4 will conclude the nosecone section and discuss the general effects that a change in nosecone configuration has on the overall RCS of the missile.

4.1.1 Simple Conic vs. Bi-conic

The difference plots comparing the simple conic nosecone family of configurations to the bi-conic nosecone family of configurations in X band are shown in Figure 4-1 and in L-S band is shown in Figure 4-2. The XPatch parametric dataset is plotted in blue and black. The C&S dataset is plotted in green. A positive value on the difference plot means the RCS of the bi-conic missile configuration is on average higher at that particular azimuth angle than the simple conic nosecone configuration and vice versa. Overall, there is good agreement between the XPatch and C&S datasets. The data are focused on the $0^\circ < \varphi < 100^\circ$ because the differences between the simple conic and the bi-conic missile configurations can be best seen here. The difference plot is also symmetrical about the point of 180° and there is negligible difference shown in the

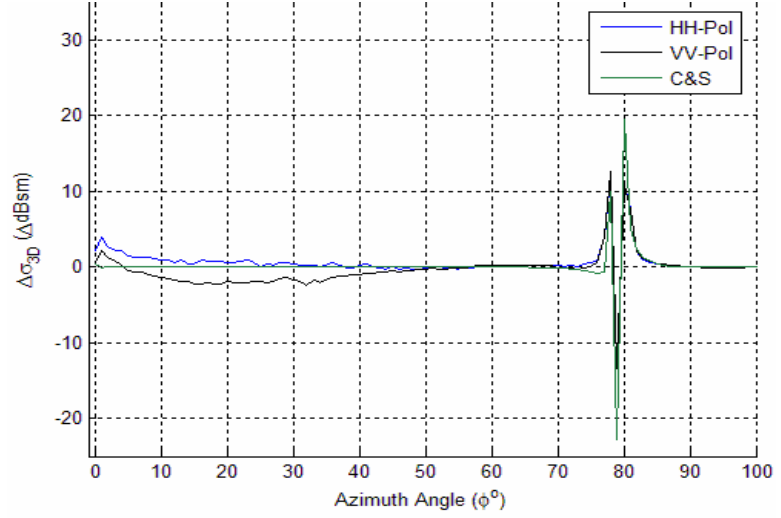
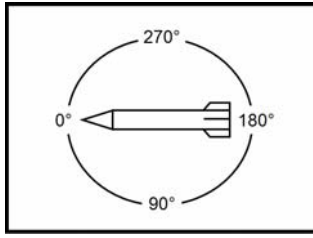


Figure 4-1: XPatch and C&S difference plots of the simple conic nosecone vs. the bi-conic nosecone configurations over X band frequencies.

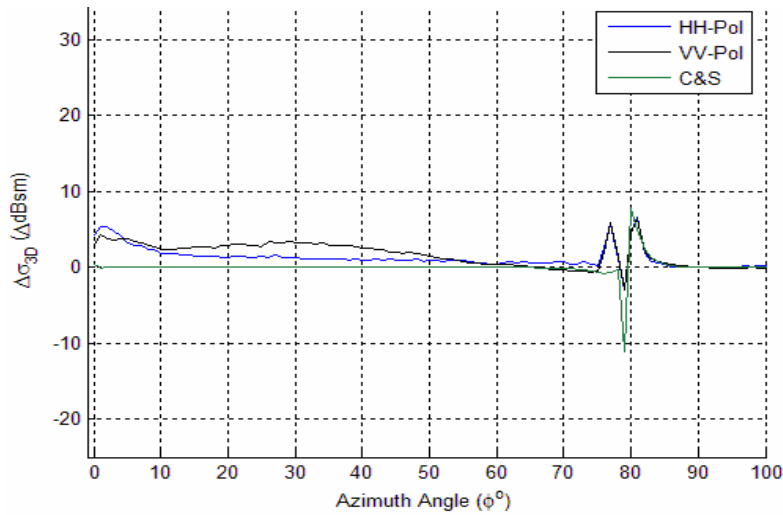


Figure 4-2: XPatch and C&S difference plots of the simple conic nosecone vs. the bi-conic nosecone configurations over L-S band frequencies.

angles between 90° and 270° thus all the information can be captured within this azimuth region.

There are two series of prominent differences in the immediate vicinity of $\phi = \pm 79^\circ$ at both frequency bands. The angles at which these large differences occur are specifically at $\pm 78^\circ$, $\pm 79^\circ$, $\pm 80^\circ$. For the Xpatch dataset, the X band difference starts to

increase in the $\varphi < |10^\circ|$ region to a value of 4 ΔdBsm at $\varphi = 1^\circ$ in HH polarization and 2.2 ΔdBsm in VV polarization. In L-S band frequencies, there is also a rise in difference in the $\varphi < |10^\circ|$ region up to a value of approximately 5 ΔdBsm $\varphi = 1^\circ$ for both HH and VV polarizations. The C&S difference plot remains fairly consistent around 0 ΔdBsm . The difference in the $\varphi < |10^\circ|$ region in the XPatch dataset is due to the wedge created by the transition of a 12° conic half angle to a 10° conic half angle in the bi-conic nosecone. The wedge contributes a diffractive effect in the bi-conic nosecone that is not present in the simple conic shape. Diffractive effects are a limitation of the C&S formulations, thus there is no noticeable change in the $\varphi < |10^\circ|$ region for the C&S difference plot.

Figure 4-3 illustrates that the prominent differences that occur at these specific angles are due to the change in where the specular returns occur on the nosecone. The high negative difference at $\pm 79^\circ$ is due to the specular return from the normal to the half angle of the 11° simple conic nosecone that is not present on the bi-conic nosecone. The high positive differences at $\pm 78^\circ$ and $\pm 80^\circ$ are due to the specular returns from the normals to the half angles of the 10° and 12° conic components of the bi-conic nosecone that is not present in the simple conic nosecone.

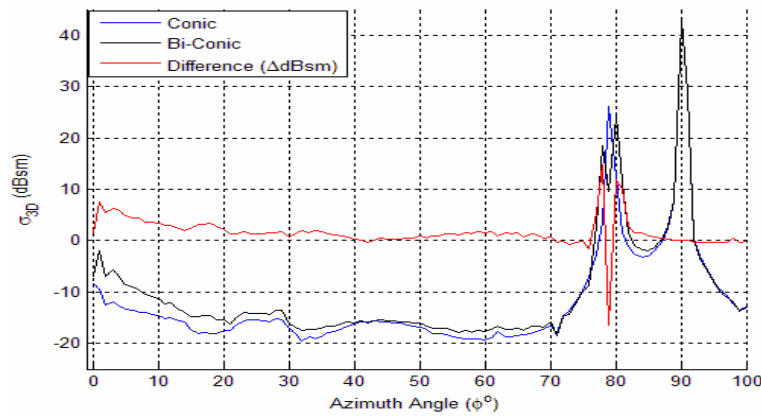


Figure 4-3: XPatch RCS of simple conic nosecone configuration compared to RCS of bi-conic nosecone configuration at X band in HH polarization at $\theta = 0^\circ$.

Other than the differences discussed, the difference plots show very little variation within each frequency band. When comparing difference levels, the magnitude of differences in the L-S band at $\varphi = \pm 78^\circ, \pm 79^\circ$ and $\pm 80^\circ$ are about 5 dBsm lower than in X band. The reason for significant drop in magnitude of the differences between the two frequency bands can be explained by the relationship between RCS lobing patterns and frequency. When a target with a characteristic length is swept across in angle, a higher frequency will result in narrower lobes in the RCS pattern because its electrical size is larger and there are more phase variations along the same range of angles. In X-Band, the frequency is high enough to give enough resolution to see each specular return at each angle normal to the half angles of the nosecones. In essence, the X-Band allows enough resolution to isolate the specular mainlobes from conic specular returns within a single degree, whereas the lobes of the specular returns in L-S Band are not isolated within a single degree. At L-S Band, the specular mainlobe at $\varphi = \pm 78^\circ$ and $\pm 80^\circ$ “spill out” into $\varphi = \pm 79^\circ$ and look like a single lobe. Figure 4-4 illustrates that the two distinct spikes for the bi-conic nosecone, which are clearly seen at 78° and 80° at X Band, has melded into one lobe centered at 79° .

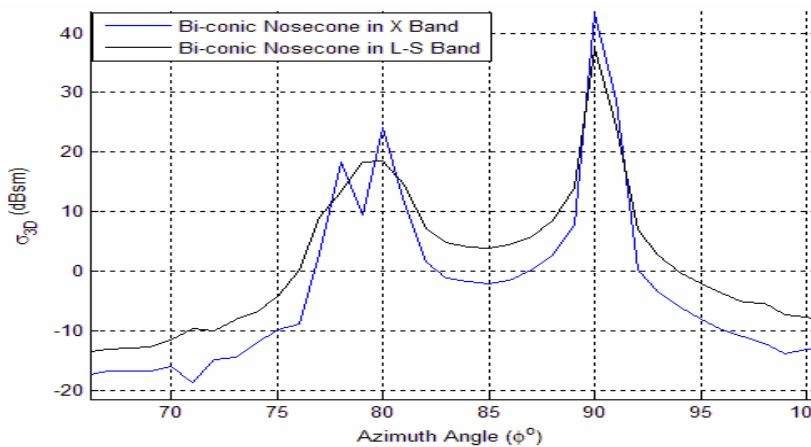


Figure 4-4: XPatch RCS of bi-conic nosecone missile plotted in X band and L-S band illustrating loss of resolution of conic component specular return peaks at lower frequencies.

4.1.2 Simple Conic vs. Broken

Figure 4-5 and Figure 4-6 show the difference plots comparing the family of simple nosecone configurations to the family of broken nosecone configurations in X band and L-S band, respectively. The angles of greatest discrepancy between the two missile configurations once again occur at the normals to the half angles of the conic components of the nosecones. The difference at $\varphi = \pm 69^\circ$ corresponds to the normal to the half angle of the 21° conic component in the broken missile configuration. Even though both missile configurations have a nosecone component with a half angle of 11° , both 11° conic components do not have the same dimensions. The simple nosecone's 11° conic component runs the entire length of the 3 m nosecone whereas the 11° component of the broken nosecone runs only a third of the full 3 m length. Thus the specular returns from both 11° conic components will occur at the same angles but differ in magnitude. This difference in dimension causes a difference of approximately $10 \Delta\text{dBsm}$ at $\varphi = 79^\circ$. Note that if the broken nosecone did not have an 11° conic component, the magnitude of difference at $\varphi = 79^\circ$ would be greater.

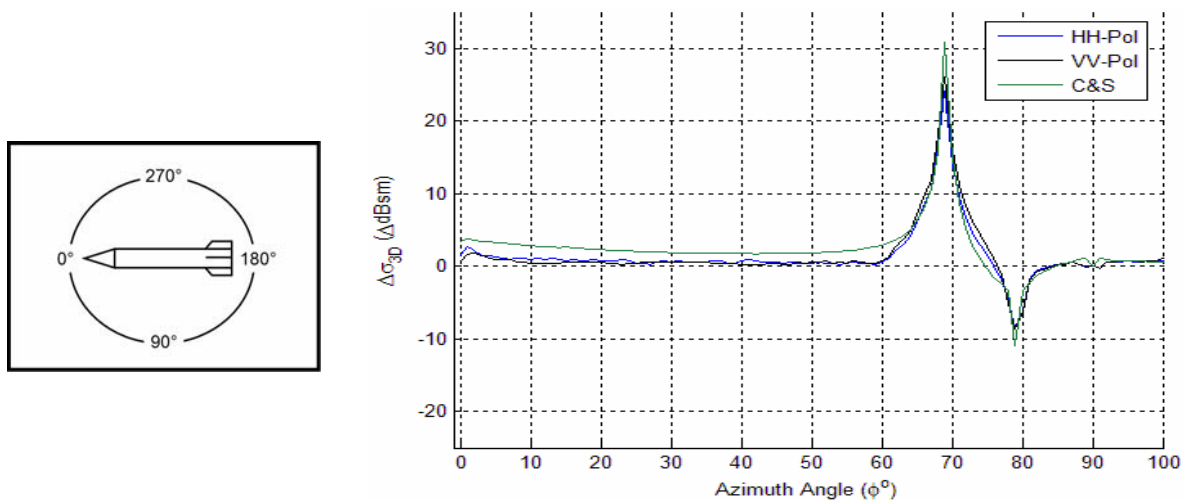


Figure 4-5: XPatch and C&S difference plots of the simple conic nosecone vs. the broken nosecone configurations over X band frequencies.

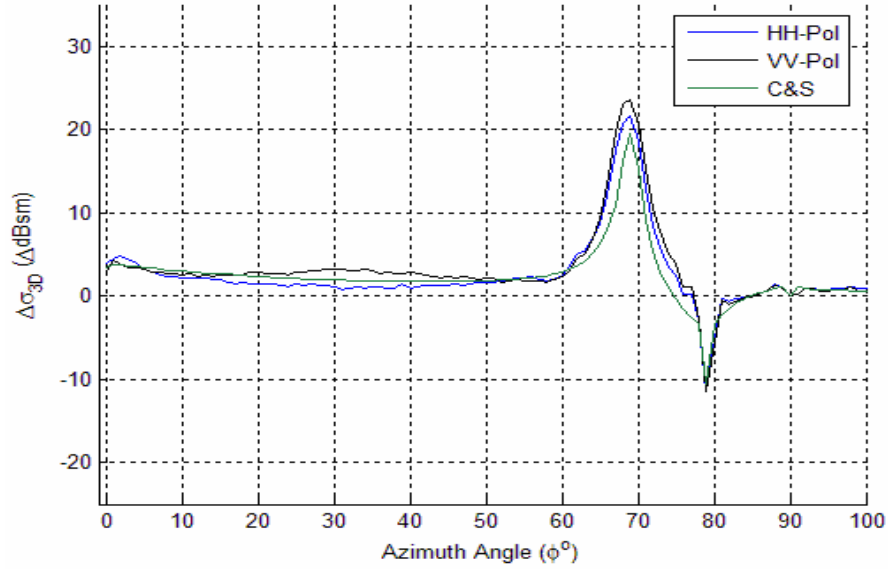


Figure 4-6: XPatch and C&S difference plots of the simple conic nosecone vs. the broken nosecone configurations over L-S band frequencies.

There is also a slight difference within 10° of the nose-on angle ($\varphi = 0^\circ$) between the two configurations. This difference is due to the diffraction within the broken nosecone. There are two discontinuities in the broken nosecone: one at the transition from the 11° conic component to the middle nosecone cylinder and the other discontinuity at the transition from the middle nosecone cylinder to the 21° conic component. The discontinuities at the transitions cause diffractive effects to take place causing a rise in RCS signature near $\varphi = 0^\circ$.

Note that in Figure 4-5, the C&S difference plot shows more of a difference in the $0^\circ < \varphi < 65^\circ$ region than does the XPatch dataset. The higher ΔdBsm difference of the C&S difference plot is due to the fact that the C&S formulas leave out diffractive effects. The $0^\circ < \varphi < 65^\circ$ region is a non-specular region with very low returns. Figure 4-7 shows the RCS and difference plot between the conic and broken nosecone configurations for the XPatch dataset. In the $0^\circ < \varphi < 65^\circ$ region, the RCS of both the conic and broken missile configurations are on the order of -17 dBsm. In the same azimuth region, the

C&S dataset presents the RCS of the conic missile configuration on the order of -30 dBsm and the bi-conic missile configuration on the order of -25 dBsm as shown in Figure 4-8. The RCS levels are significantly lower in the C&S dataset than in the XPatch dataset because the effects of diffraction are not taken into consideration. The lower RCS at this region made the RCS plot of the conic nosecone configuration more susceptible to change from the return from the 21° conic component in the broken missile.

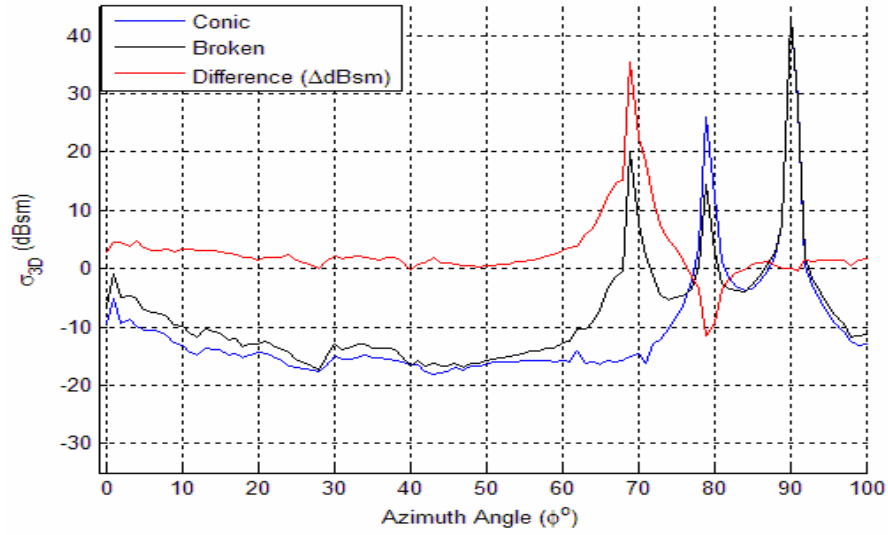


Figure 4-7: XPatch RCS of simple conic nosecone configuration compared to RCS of broken nosecone configuration at X band in VV polarization at $\theta = 0^\circ$.

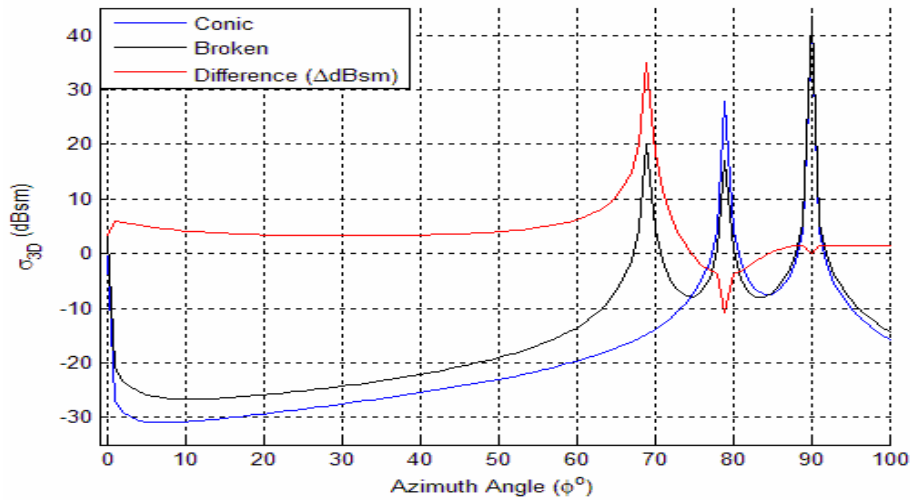


Figure 4-8: C&S RCS of simple conic nosecone configuration compared to RCS of broken nosecone configuration at X band at $\theta = 0^\circ$.

It is important to note that dBsm differences by themselves cannot be used to find an arithmetic difference in square meters. The ΔdBsm can only give a ratio of how much larger or smaller one configuration's RCS is to another. The angle of highest difference on the dBsm difference plot may not translate to the angle with largest RCS on the signature plot. In fact, the opposite is more likely to be true because on a log scale, smaller magnitudes are more sensitive to change.

4.1.3 Bi-conic Nosecone vs. Broken

Figure 4-9 and Figure 4-10 are the difference plots comparing the bi-conic nosecone missile configuration to the broken nosecone missile configurations in X band and L-S band frequencies, respectively. The angles of greatest difference once again lie at the normals to the half angles of the conic components of the nosecones. In X band, peaks occur at $\phi = \pm 69^\circ$ and $\pm 79^\circ$ due to the high specular returns from the 21° and 11° conic components in the broken nosecone at those angles. The dips in the difference plot at $\phi = \pm 78^\circ$ and $\pm 80^\circ$ are caused by the high specular returns from the 12° and 10° conic components in the bi-conic nosecone at those angles.

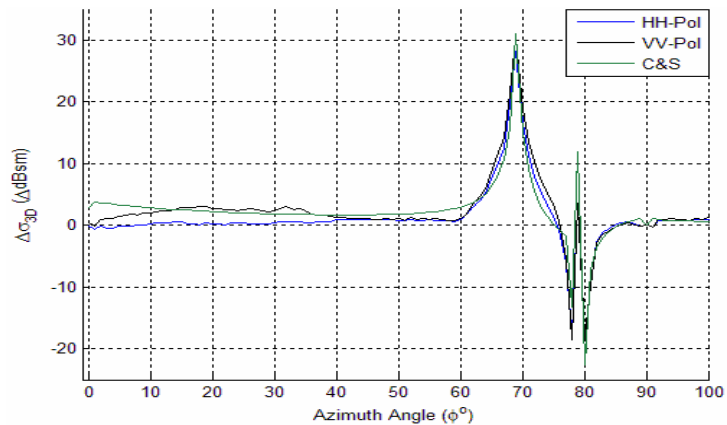
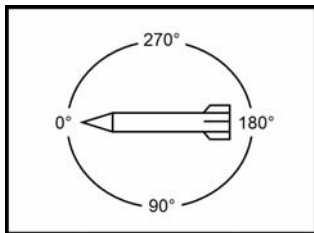


Figure 4-9: XPatch and C&S difference plots of the bi-conic conic nosecone vs. the broken nosecone configurations over X band frequencies.

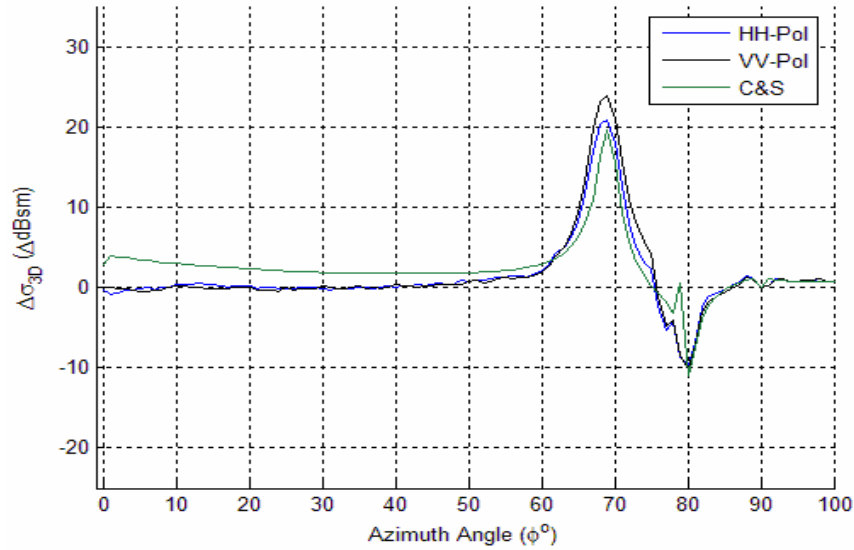


Figure 4-10: XPatch and C&S difference plots of the bi-conic nosecone vs. the broken nosecone configurations over L-S band frequencies.

The same effects are observed in L-S band. The dip at $\varphi = 78^\circ$ and the peak at $\varphi = 79^\circ$ are barely distinguishable from each other but can be observed upon close observation. The reason the differences at the nosecone normals are not seen as prominently as in Figure 4-9 is due to the loss of angular resolution at lower frequencies as discussed in section 0 and illustrated in Figure 4-4.

Unlike the previous two nosecone comparisons, there seems to hardly be any differences between the RCS of the bi-conic nosecone and the broken nosecone at nose-on aspects in the XPatch dataset. Diffractive effects from the bi-conic nosecone and the broken nosecone accounted for the rises in the difference plots at nose-on aspects when compared separately to the simple conic nosecone. However, the fact that there is hardly a difference in the nose-on aspects between the bi-conic nosecone missile configuration and the broken nosecone missile configurations means that the strengths of the diffractive effects are equal in magnitude and average out to be the same over elevation and frequency in the XPatch dataset. On the other hand, the C&S has a difference of

approximately 2 Δ dBsm on average at both X Band and L-S Band in the $0^\circ < \varphi < 65^\circ$ region, like in the simple conic vs. bi-conic case.

4.1.4 Summary of Nosecones

The C&S and XPatch datasets agree very well in showing that when two different missile nosecones have conic components with different half angles, the greatest change occurs at the normals to the half angles of those nosecone conic components due to the specular returns. The difference in dBsm at those angles depends on the dimension of the conic components, the angular regions at which the change occurs (specular regions are less sensitive to changes in RCS), and the frequency of the illumination.

Differences due to diffractive effects seen in the XPatch dataset, are caused by discontinuities in the nosecone of the missile are strongest at the nose-on aspects of the missile. Besides the angles normal to the conic components of the nosecones and nose-on aspects, where diffractive effects are significant, the change in RCS is consistently close to 0 Δ dBsm.

4.2 Analysis on the Effects of Fins

This section will investigate the effects of adding fins or varying fin size on the RCS of a generic ballistic missile. The three fin configurations will be compared in the following order: finless vs. small fin configurations in section 4.2.1, finless vs. large fin configurations in section 4.2.2, and small fin vs. large fin configurations in section 4.2.3.

Section 0 will conclude the fin section and discuss the general effects that a change in fin configuration has on the overall RCS of the missile.

4.2.1 Finless vs. Small Fins

Figure 4-11 and Figure 4-12 are the averaged difference plots between the finless missile configuration and the small fin missile configuration in X band and L-S band respectively. Though the difference plots seem rather complex, the phenomenon behind the differences between the compared missile configurations can be well accounted for. In the XPatch data, the highest ΔdBsm difference occurs at $\phi = \pm 59^\circ$. This difference is due to the specular return introduced from the 31° tilted leading edge from fins 2 and 4 shown in Figure 4-13.

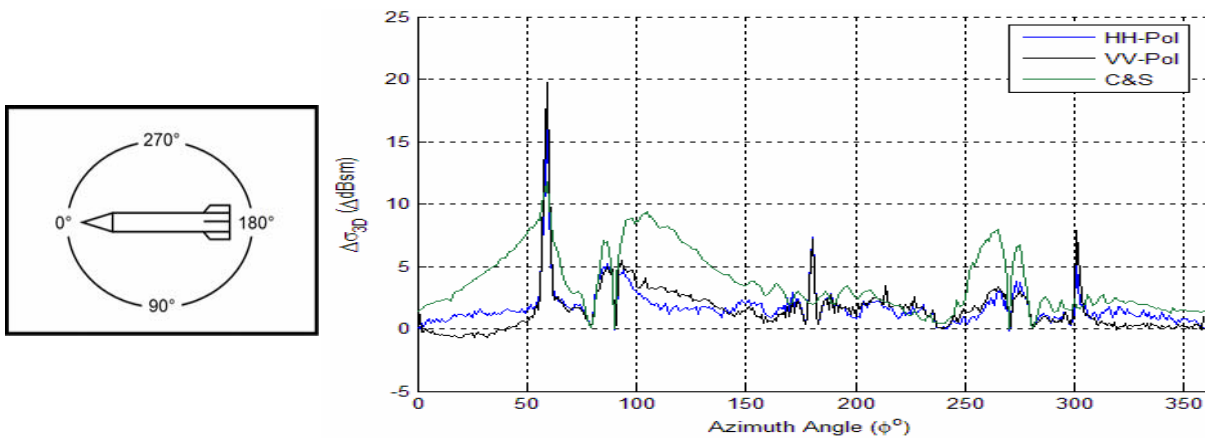


Figure 4-11: XPatch and C&S difference plots of the finless missile configuration vs. the small fin missile configuration over X band frequencies.

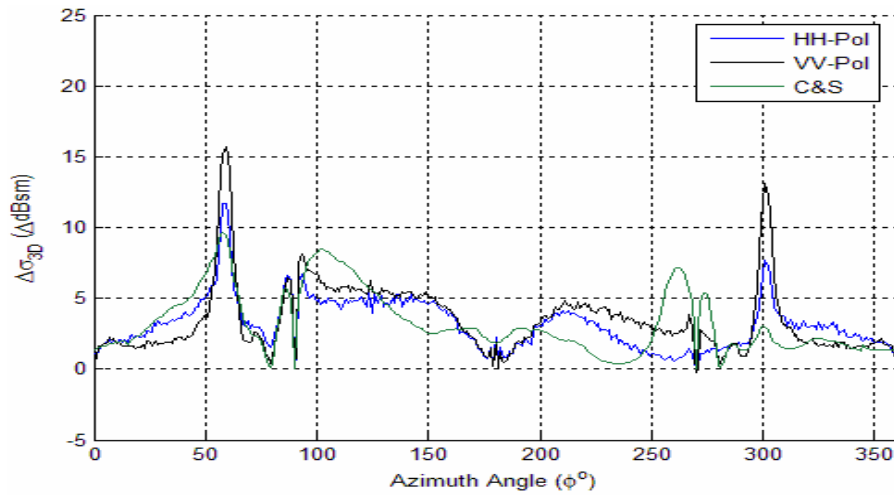


Figure 4-12: XPatch and C&S difference plots of the finless missile configuration vs. the small fin missile configuration over L-S band frequencies.

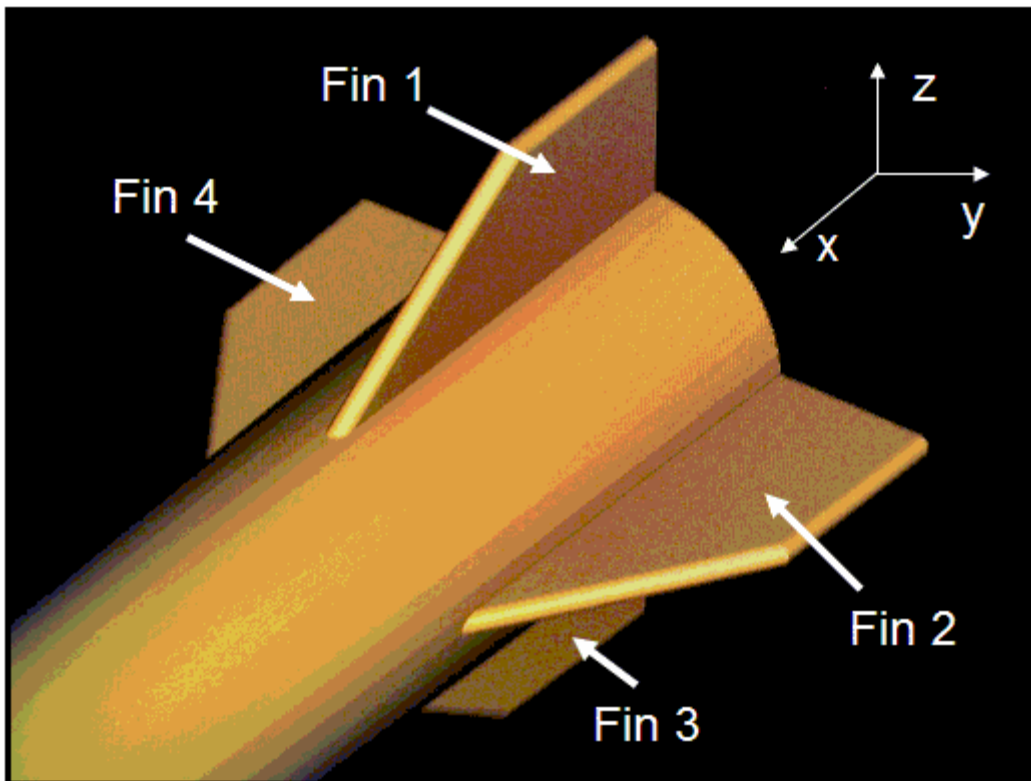


Figure 4-13: XPatch screenshot of missile fins with curved edges.

The same peaks can be observed in the C&S dataset but the difference levels of the peaks are significantly lower than the XPatch datasets. The reason for this dissimilarity is due to a difference in the way the fin edges were modeled. The XPatch facet files modeled the edges of the fins with a curvature which can be seen in Figure 4-13, thus there will be a bit consistent specular return across elevation from the fin edges when the azimuth angle is normal to the fin edge. This consistent return across elevation can be observed at $\varphi = \pm 59^\circ$ in Figure 4-14. In contrast, the edges in the C&S dataset were modeled as flat edges and will not return a consistent specular return over elevation. Thus in Figure 4-15, a specular return is observable at $\varphi = \pm 59^\circ$ only when $\theta = 0^\circ$, where the radar is normal to the flat edge.

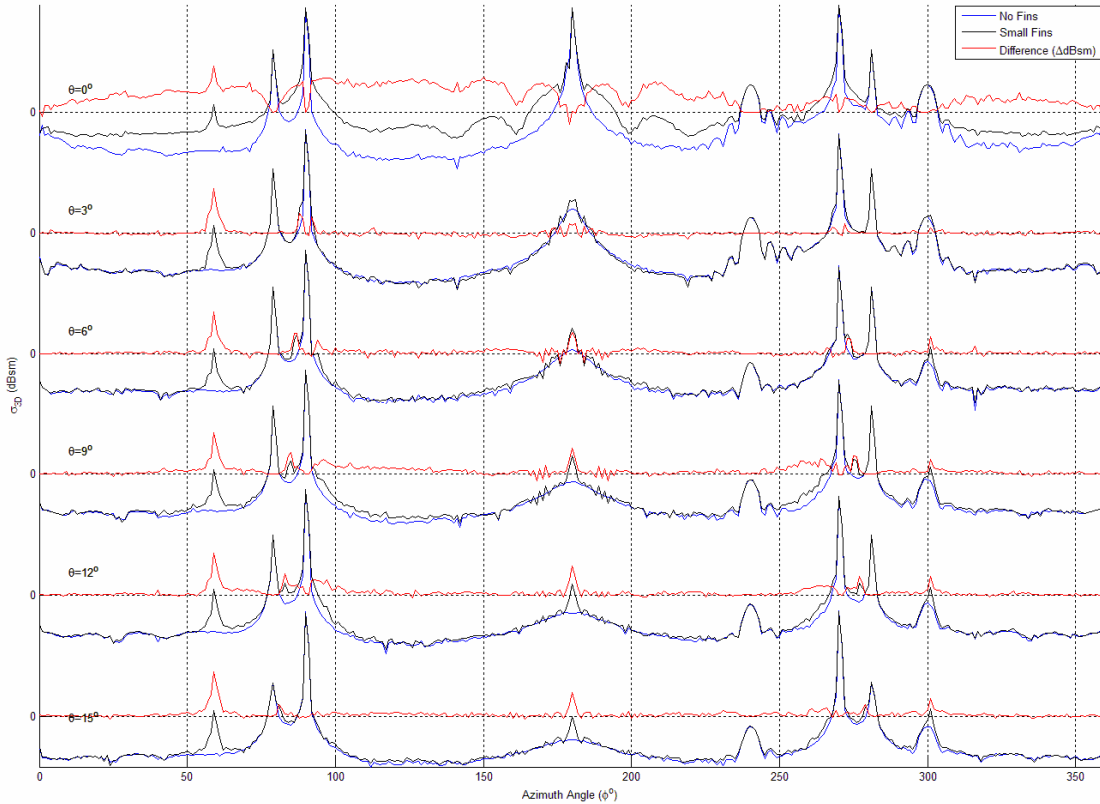


Figure 4-14: XPatch RCS comparison between finless and small fin missile configurations over elevation in X band at VV polarization.

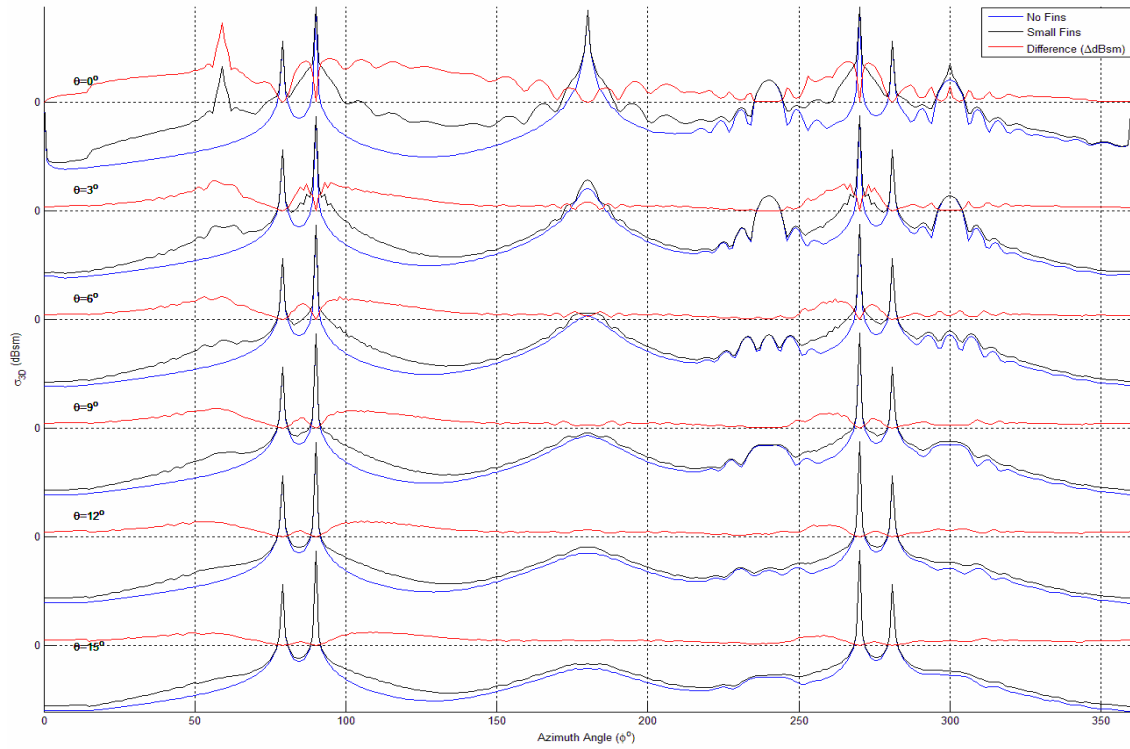


Figure 4-15: C&S RCS comparison between finless and small fin missile configurations over elevation in X band at VV polarization.

The large difference that occurs at $\varphi = 180^\circ$ in the XPatch data set but does not appear on the C&S dataset can also be explained by difference in modeling. The fin edges that are perpendicular to the cylindrical body of the missile fins 2 and 4 are modeled as curved edges in the XPatch facet files instead of a flat surface, as in the C&S dataset. Due to the curved nature of the edge, a high specular return occurs over a range of elevations as Figure 4-16 illustrates.

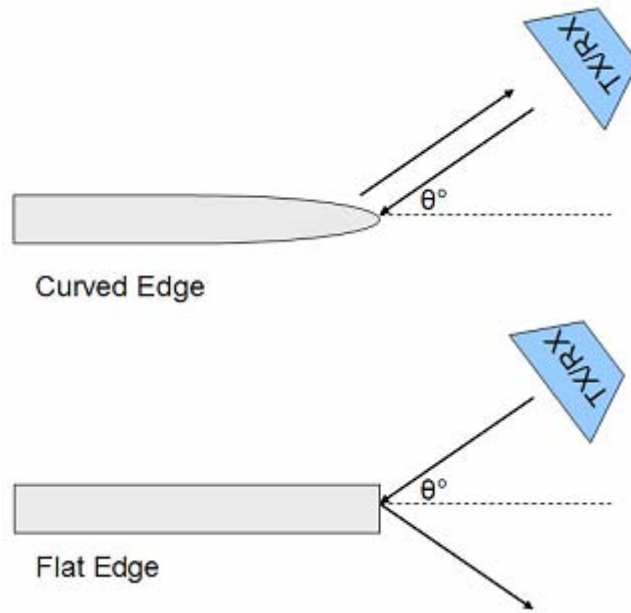


Figure 4-16: Illustration of difference of specular returns between curved fin edges and flat fin edges over elevation.

In Figure 4-11, deep nulls occur at $\varphi = \pm 79^\circ$ and $\pm 90^\circ$ where specular returns are strong regardless of elevation and the returns from the fins are relatively insignificant. In the regions just shy of $\pm 90^\circ$, high differences levels occur. The reason for these high differences is because without the fins, the width of the main specular lobe is dependent on the length of the cylindrical missile body. The 13 m length of the missile body will cause a very narrow mainlobe of approximately 0.114° . When fins are introduced, the edge of fins 2 and 3 and the sides of fins 1 and 3 have dimensions that are less than that of the missile body. Therefore the returns from the fins will have a wider mainlobe width of 2° . Due to the difference in mainlobe width, the angles just shy of $\varphi = \pm 90^\circ$ will have a significant difference value.

In X band, the C&S difference plot, shown in Figure 4-11 consistently had higher difference levels over the non-specular regions of the graph. This is because C&S formulas do not take into consideration diffractive effects, which results in lower RCS

values than XPatch in non-specular angles. The regions of lower RCS returns are more sensitive to changes and will result in a higher difference value in ΔdBsm .

In the XPatch dataset, there is a consistent rise of 2 dBsm on average in X band between $\varphi = 100^\circ$ and $\varphi = 260^\circ$ which can be attributed to a combination of diffraction from the edges of the fins and interactions between the fins and other components of the missile. In VV-polarization the RCS remains consistent at $\varphi < |50^\circ|$ but is raised by about 1.5 dBsm in HH-polarization.

The effects of the fins seen at X-band are also seen at L-S band. The peaks in difference levels at $\varphi = \pm 59^\circ$ are due to the 31° leading edge of fins 2 and 4. The deep nulls at $\varphi = \pm 79^\circ$ and $\varphi = \pm 90^\circ$ are due to the dominant specular returns at those angles that make the effects of the fins insignificant. The angles in the immediate vicinity of the deep nulls at $\varphi = \pm 90^\circ$ have a significant ΔdBsm difference.

The large difference at $\varphi = 180^\circ$ in the X band is no longer as prominent in L-S band. This is because the thickness of the edge is 0.1 m whereas the center frequency of L-band has a wavelength of 0.12 m. The wavelength to target dimension ratio is no longer considered in the optics region resulting in a weaker return. In the XPatch dataset, there is a consistent rise of 4 dBsm on average between $\varphi = 100^\circ$ and $\varphi = 260^\circ$. In the $\varphi < |50^\circ|$ region, the RCS rises by 2.5 dBsm on average in both polarizations.

4.2.2 Finless vs. Large Fins

The averaged difference plots for X-band and L-S band are shown in Figure 4-17 and Figure 4-18, respectively. The results for the finless vs. large fin configurations are almost identical to that of the finless vs. small fin configurations. The only difference is

that the RCS difference levels are higher in the finless vs. large fin case. The same effects and features that result from the introduction of the small fins discussed in section 4.2 can be applied to the large fins.

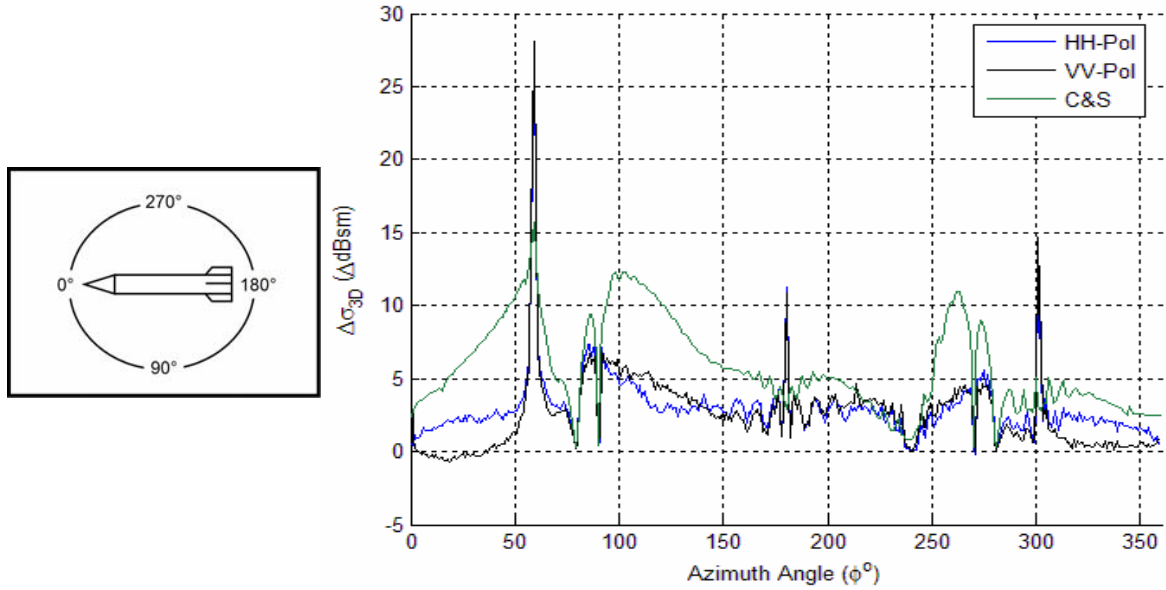


Figure 4-17: XPatch and C&S difference plots of the finless missile configuration vs. the large fin missile configuration over X band frequencies.

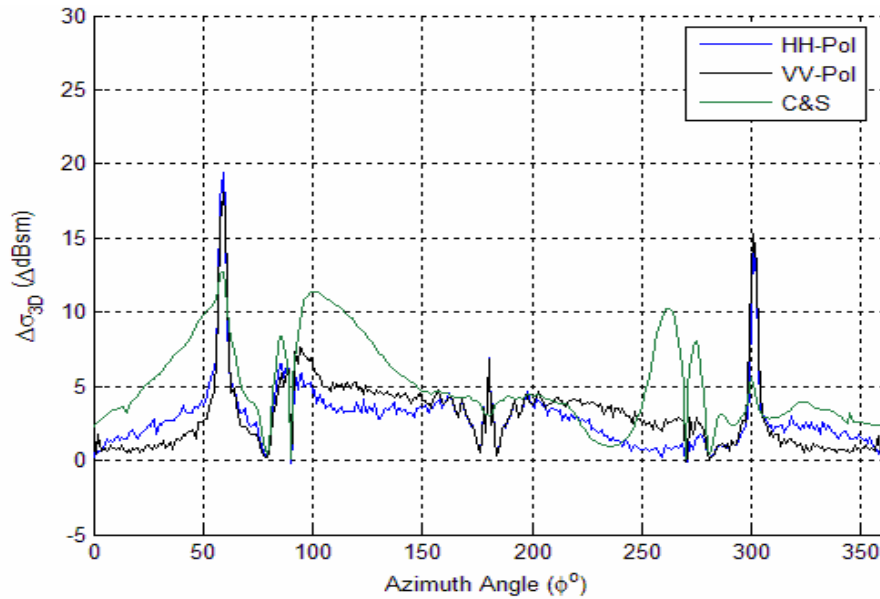


Figure 4-18: XPatch and C&S difference plots of the finless missile configuration vs. the large fin missile configuration over L-S band frequencies.

4.2.3 Small Fins vs. Large Fins

The difference plot in Figure 4-19 shows $\varphi = \pm 59^\circ$ is the angle at which the largest difference occurs for the XPatch dataset. The difference is due to the increase in size of the 31° angled leading edge. There are also three small peaks in the XPatch difference plots at $\varphi = 180^\circ$, 176° , and 184° . The peak at $\varphi = 180^\circ$ is a result of the higher specular return from increased length and width of the edges perpendicular to the cylindrical missile body. The peaks that occur at $\varphi = 176^\circ$ and $\varphi = 184^\circ$ are a result of raised RCS levels around 180° of the larger fins which are dominant at $\theta = 0^\circ$ but are averaged into the plots. These peaks can be seen in the RCS comparisons over elevation between the small fin and large fin configurations in Figure 4-20 at $\theta = 0^\circ$.

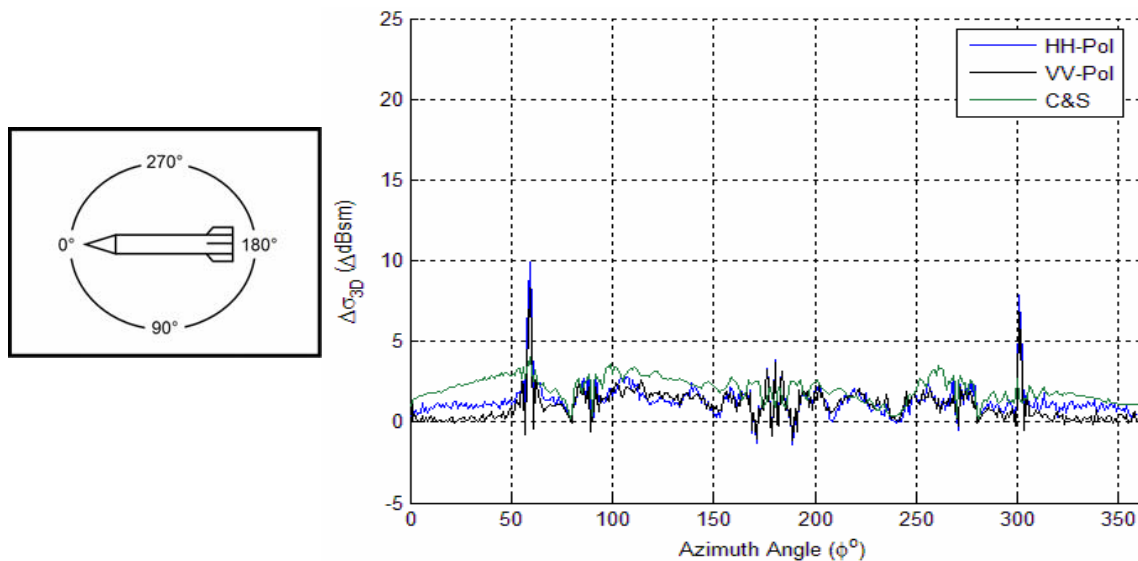


Figure 4-19: XPatch and C&S difference plots of the small fin missile configuration vs. the large fin missile configuration over X band frequencies.

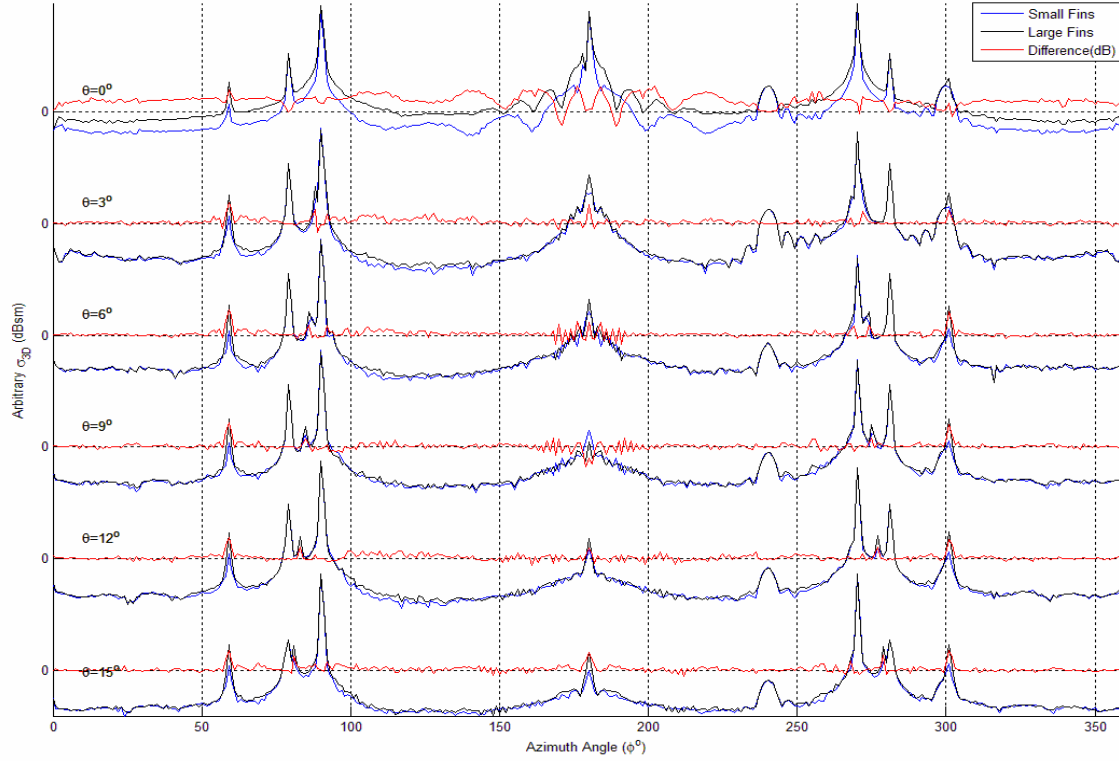


Figure 4-20: XPatch RCS comparison between small and large fin missile configurations over elevation in X band at HH polarization.

In both the C&S and XPatch datasets, the nulls at $\varphi = \pm 79^\circ$ and $\varphi = \pm 90^\circ$ are still observed because the increased size of the fin edges that the radar sees are insignificant compared to the specular returns at those angles. In X band, there is a rise of 1.5 dBsm and 2 dBsm on average between $\varphi = 100^\circ$ and $\varphi = 260^\circ$ for the XPatch and C&S datasets, respectively, due to the increase in specular, diffractive and interactive effects from the introduction of the large fins. In the $\varphi < |50^\circ|$ region, the RCS of the XPatch data is raised by approximately 1 dBsm on average in VV-polarization and barely changed in HH-polarization. In the same region, there is a rise of 2.5 dBsm on average for the C&S dataset.

Figure 4-21 shows the averaged difference plots for L-S band frequencies. The same features are seen in the L-S band difference plot as that of the X band frequencies.

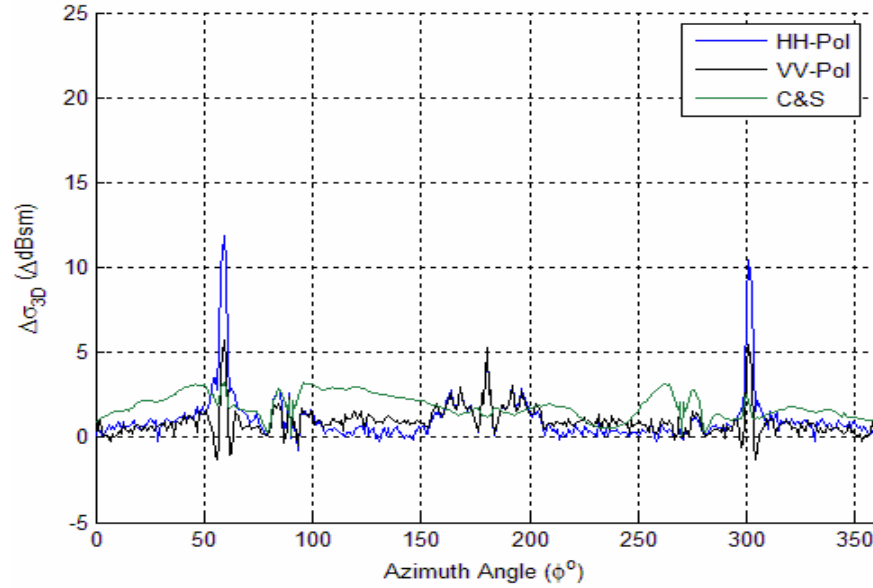


Figure 4-21: XPatch and C&S difference plots of the small fin missile configuration vs. the large fin missile configuration over L-S band frequencies.

4.2.4 Summary of Fins

From this study, the effects of introducing fins on a finless missile configuration generally made the biggest impact at $\varphi = \pm 59^\circ$ by the 31° angled edge of the fin returning a specular return. The angle at which the specular return from the 31° angled edge occurs is an angle that is over a non-specular region in the finless missile configuration, thus causing the sharp peaks in the difference plots at those angles. However, if the front edge of the wing were angled such that its specular return occurred at an angle where specular returns were strong; the difference plot would not be as sensitive. Thus one must take very careful note of how the fin edges are oriented when analyzing a target's RCS.

The regions of high specular return at $\varphi = \pm 79^\circ$ (nosecone) and $\varphi = \pm 90^\circ$ (body) were not sensitive to changes in RCS and had difference values close to 0 Δ dBsm. At the angles between $\varphi = 100^\circ$ and $\varphi = 260^\circ$, there is a consistent rise in dBsm that is dependent on the dimensions of the fins.

4.3 Analysis on the Effects of Heat Shielding

The effects of heat shielding are discussed in this section. The heat shield in this thesis is a PEC-backed 10 mm coating of asbestos phenolic. The asbestos phenolic has a relative material permittivity of $\epsilon_r = 5 - 0.5j$ and a relative permeability of $\mu_r = 1$. The complex term in the relative permittivity indicates there will be loss associated with the material as the radiation passes through it.

Since the effects of heat shield application are specific to the geometry of the nosecone, the specific effects of the heat shield will first be discussed for each of the three nosecone configurations separately and then the summary of the effects will be presented at the end of this section.

4.3.1 Heat Shielding on Conic Nosecone

Figure 4-22 shows the difference plot comparing the PEC conic nosecone missile configurations with the heat-shielded conic nosecone configurations in X-band. The azimuth angle at which the heat shielding makes the biggest impact is at $\varphi = \pm 79^\circ$, which is the normal to the half-angle of the 11° cone. On average there is a 7.5 dBsm decrease in RCS return at 79° when heat shielding is applied. There is a considerable drop in specular RCS at that angle due to the heat-shielding.

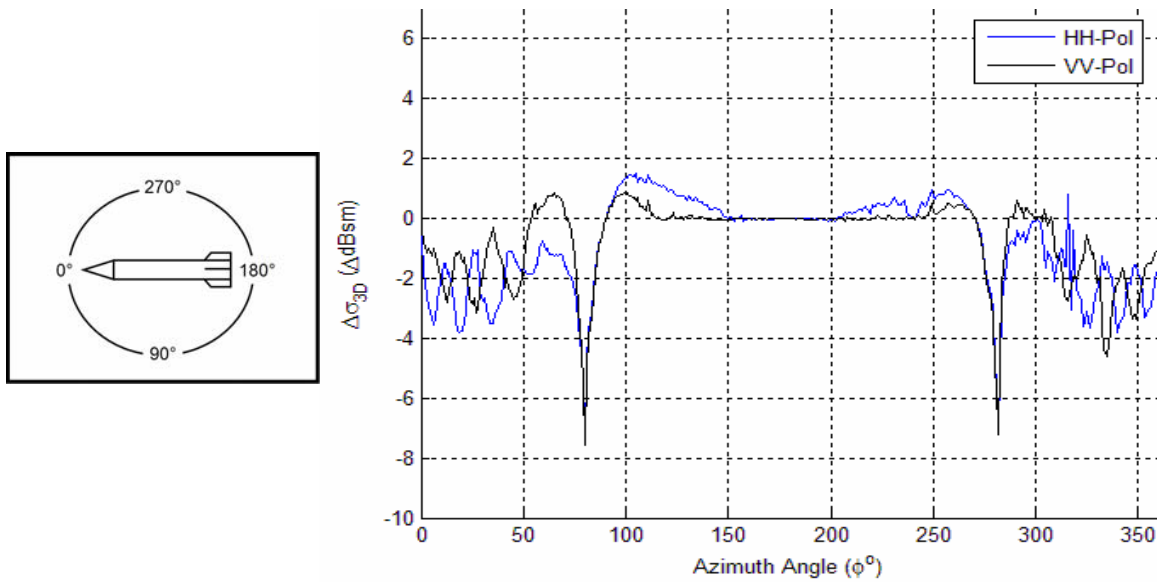


Figure 4-22: XPatch difference plots of the PEC conic nosecone missile configuration vs. the heat shielded missile configuration over X band frequencies.

In the $\varphi < |50^\circ|$ region, there is approximately a 2 dBsm decrease on average in RCS due to heat shielding but the oscillations vary from 0.5 to 4.5 dBsm. There are angles at which heat shielding raises the RCS signature. However, these rises in RCS are usually no more than 1 dBsm in magnitude and they occur in non-specular regions. These effects are minute compared to the magnitude of the RCS drop at $\varphi = \pm 79^\circ$. The oscillations in the $\varphi < |50^\circ|$ region and the angles of raised RCS can be explained by the effect of changing phase angles. When the illuminating wave travels through free space and strikes the air-asbestos phenolic boundary a portion of the energy is reflected back out and the other portion passes through the boundary. The portion of the energy that makes it through the boundary is refracted at a different angle than that of which it was traveling at in free space.

Because the return path of the illuminating wave is different between the two missile configurations, the phase interactions will add constructively and

destructively at different angles giving rise to oscillations and areas of higher RCS in the heat shielded configuration.

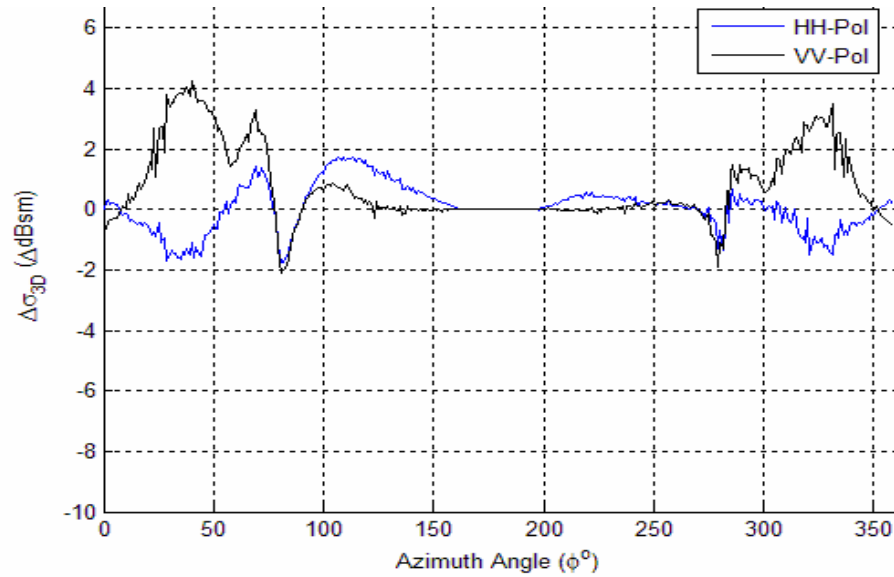


Figure 4-23: XPatch difference plots of the PEC conic nosecone missile configuration vs. the heat shielded missile configuration over L-S band frequencies

Figure 4-23 is the same set of data as Figure 4-22 for the L-S band. There is a 2 dBsm RCS drop at $\phi = 79^\circ$ due to the heat shielding absorbing some of the specular energy. In the $\phi < |50^\circ|$ at HH-polarization, the difference plot oscillates ± 1.5 dBsm due to phase interaction and is centered at 0 Δ dBsm. However, the VV-polarization heat shielding raises the RCS of the missile by up to 4 dBsm in the same angular region with its peak centered at approximately $\pm 40^\circ$. This effect is most likely due to the effects of phase interactions.

From first glance it may seem that the most significant effect heat shielding has in L-band occurs in VV-polarization at $\pm 40^\circ$ with a difference of 4 dBsm as opposed to the difference at $\pm 79^\circ$ of 2 dBsm. However, if one were to take into account the arithmetic RCS at which these differences occur, it is apparent that is not the case. In Figure 4-24,

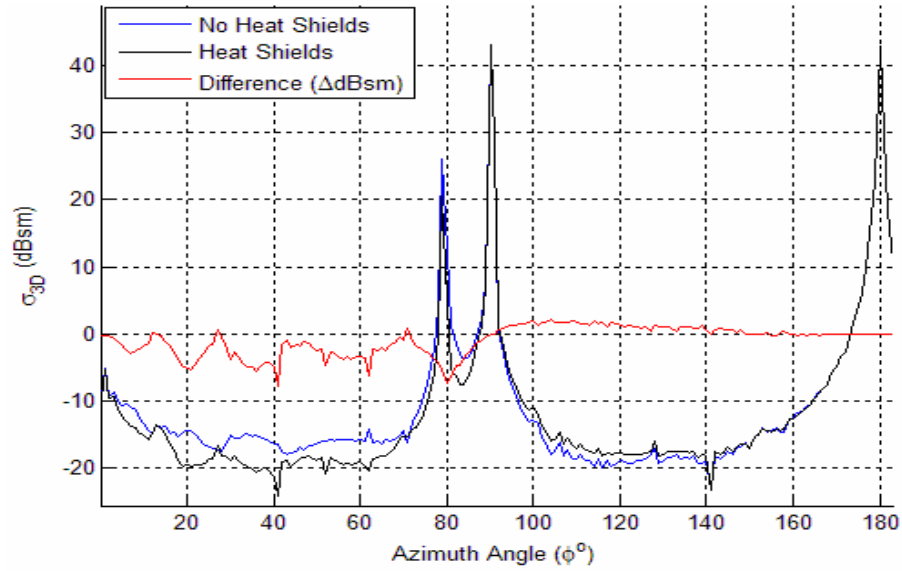


Figure 4-24: XPatch RCS of PEC conic nosecone configuration compared to RCS of heat shielded nosecone configuration.

the RCS of the PEC conic nosecone configurations at $\varphi = \pm 40^\circ$ is approximately -15 dBsm. This means that a rise of 4dBsm equates to a rise of 0.05 m^2 numerically. The RCS of the PEC conic nosecone configurations at $\varphi = \pm 79^\circ$ is approximately 20 dBsm. A 2 dBsm drop from 20 dBsm equates to a numerical drop of 36.9 square m. The greatest impact is obviously made at $\varphi = \pm 79^\circ$.

4.3.2 Heat Shielding on the Bi-conic Nosecone

Figure 4-25 and Figure 4-26 are difference plots comparing a PEC missile configuration to a heat shielded bi-conic nosecone configurations. The results of the difference plot results in Figure 4-22 and Figure 4-23 are very similar to those seen in heat-shielded conic nosecone case. The angles of greatest difference are at the normals to the half angles of the nosecone conic components: $\varphi = \pm 78^\circ$ and $\varphi = \pm 80^\circ$. At $\varphi = \pm 78^\circ$, the RCS drops by 5.3 dBsm on average when heat shields are applied. At $\varphi = \pm 80^\circ$, the

RCS drops by 7.5 dBsm on average when heat shields are applied. In the $\varphi < |50^\circ|$ region, the RCS returns oscillate between -5 dBsm and -4 dBsm. The oscillations are centered at -2 dBsm similar to the analysis from the conic configuration.

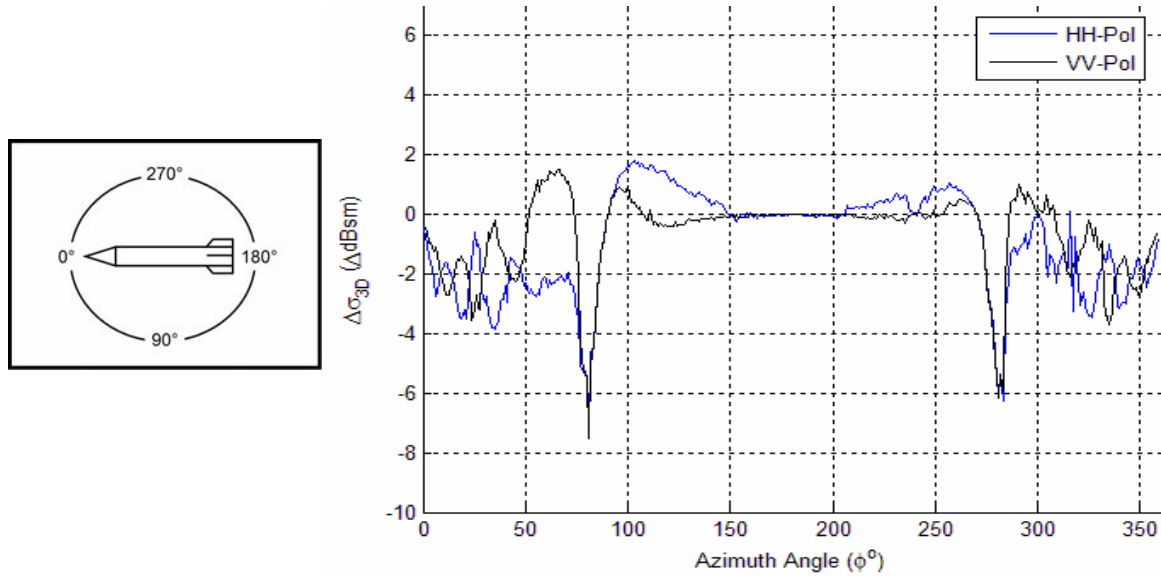


Figure 4-25: XPatch difference plots of the PEC bi-conic nosecone missile configuration vs. the heat shielded missile configuration over L-S band frequencies.

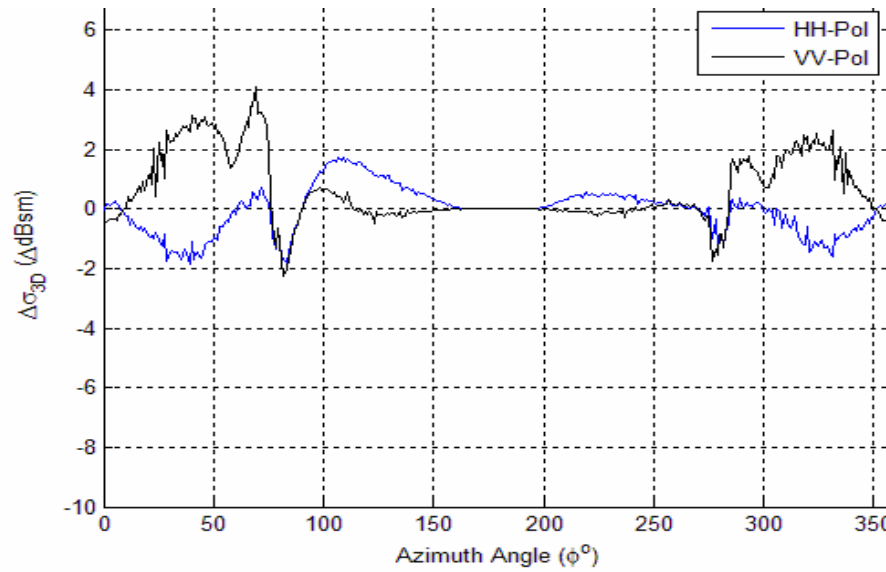


Figure 4-26: XPatch difference plots of the PEC bi-conic nosecone missile configuration vs. the heat shielded missile configuration over L-S band frequencies.

In Figure 4-26 we see the similar effects of heat shielding that we have seen in Figure 4-23. At the normals to the half-angles of the conic components of the bi-conic nosecone ($\varphi = \pm 78^\circ$ and $\varphi = \pm 80^\circ$), there is approximately a 2 dBsm drop in RCS due to heat shielding. In the $\varphi < |50^\circ|$ non-specular region there is a rise in RCS in VV polarization of up to 4 dBsm. This 4dBsm drop in the non-specular region is a small change compared to the 2dBsm drop that occurs at $\varphi = \pm 78^\circ$ and $\varphi = \pm 80^\circ$ specular region like in the conic case.

4.3.3 Heat Shielding on the Broken Nosecone

Figure 4-27 shows the difference plot comparing the PEC and heat shielded broken nosecone configurations in X band. Like in the conic and bi-conic case, the angles of greatest difference are at the normals to the half angles of the nosecone conic components: $\varphi = \pm 69^\circ$ and $\varphi = \pm 79^\circ$. At $\varphi = \pm 69^\circ$, the RCS drops by approximately -6.5 dBsm on average when heat shields are applied. At $\varphi = \pm 80^\circ$, the RCS drops by approximately -5.5 dBsm on average when heat shields are applied. In the $\varphi < |50^\circ|$ region, the RCS returns oscillate between -0.1 dBsm and -3.5 dBsm due to changes in phase interactions. The oscillations are centered at -1.8 dBsm.

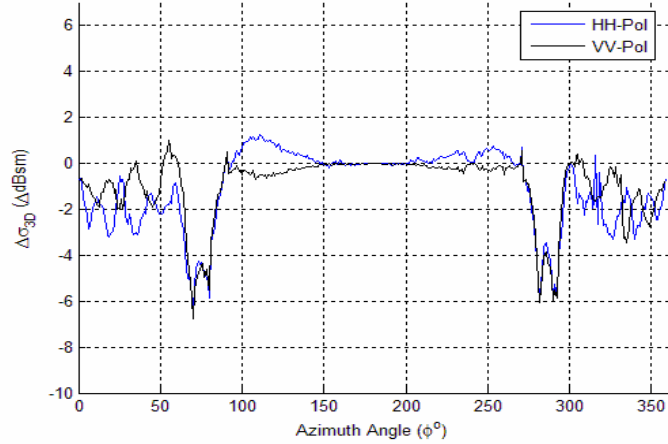
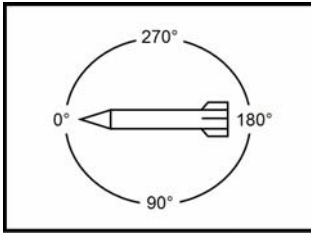


Figure 4-27: XPatch difference plots of the PEC broken nosecone missile configuration vs. the heat shielded missile configuration over X band frequencies.

In Figure 4-28 we see the same effects of heat shielding that we have seen in both the conic and bi-conic nosecone cases. At the normals to the half-angles of the conic components of the broken nosecone ($\varphi = \pm 69^\circ$ and $\varphi = \pm 80^\circ$), there is approximately a 2.5 dBsm drop in the specular return due to heat shielding. In the $\varphi < |50^\circ|$ non-specular region there is a rise in RCS in VV polarization with a peak of 3.5 dBsm centered at $\pm 49^\circ$. This 3.5 dBsm drop in the non-specular region is a small change compared to the 2.5 dBsm drop that occurs at $\varphi = \pm 78^\circ$ and $\varphi = \pm 80^\circ$ specular region like in the conic and bi-conic cases.

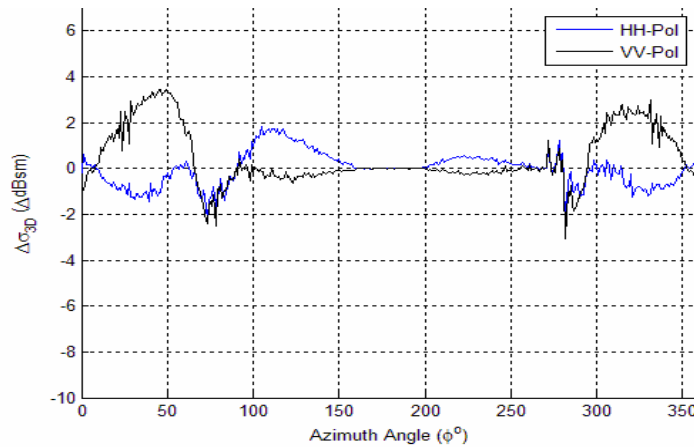


Figure 4-28: XPatch difference plots of the PEC broken nosecone missile configuration vs. the heat shielded missile configuration over L-S band frequencies.

4.3.4 Summary of Heat Shielding

In each of the three nosecone configurations the same effects of heat shielding were consistently seen. The most significant impact of heat shielding is the reduction of specular returns at the normals to the half-angles of each conic component in the nosecone. The amount by which the specular returns are reduced is dependent on frequency and the dimensions of the conic portion of the nosecone.

In the $\varphi < |50^\circ|$ region at X band frequencies, there were oscillations present within the difference plots but averaged out as an overall drop in RCS signature. The introduction of the heat shield changed the return path of the illuminating waves back toward the receiver which changes the phase interactions at the receiver and caused the oscillations in the difference plots. The change in phase interactions at the receiver may also account for why heat shielding raises the RCS of the missile at certain non-specular regions. The oscillations only occur predominantly in the $\varphi < |90^\circ|$ region because this region is where the heat-shielded nosecone component of the missile has the greatest impact on the RCS of the entire missile.

In the $\varphi < |50^\circ|$ region at L-S band frequencies, a heat shielded missile configuration illuminated by VV-polarization will have a signature rise of up to 4 dBsm. Though the cause of this rise in RCS is unaccounted for in this thesis, its presence in every one of the difference plots for the conic, bi-conic, and broken nosecones may warrant further study.

4.4 Analysis on the Effects of Paneling

Figure 4-29 and Figure 4-30 are the differences in paneled and non-paneled RCS returns averaged over frequency, elevation, and configuration in the X-band and L-band frequencies, respectively. In the X-band frequency there is an obvious effect that paneling has. The rivets in XPatch were modeled as cylindrical rods pointing in the +y direction. The orientation of the panel riveting results in the HH-polarization giving a higher RCS than the VV-polarization because the E-component in HH-polarization lies parallel to the broadside of the rivet cylinder.

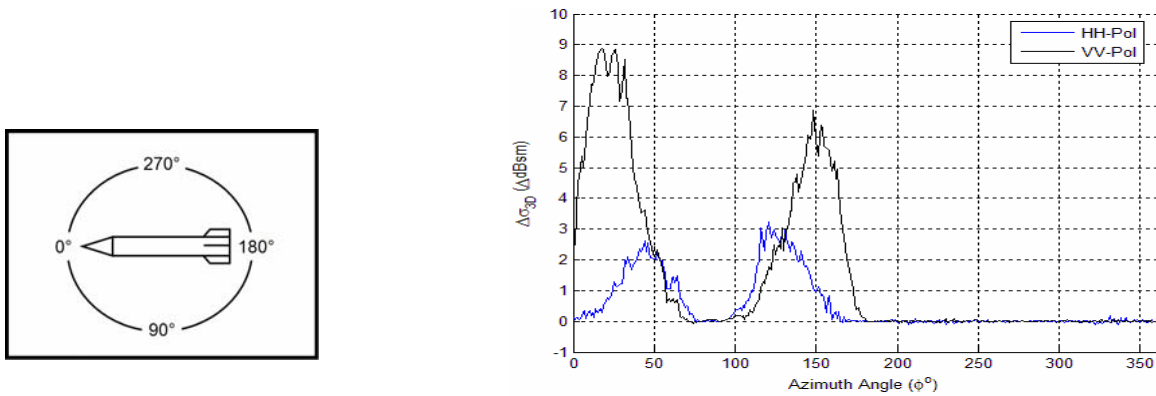


Figure 4-29: XPatch difference plots of non-paneled missile configurations vs. paneled missile configuration over X band frequencies.

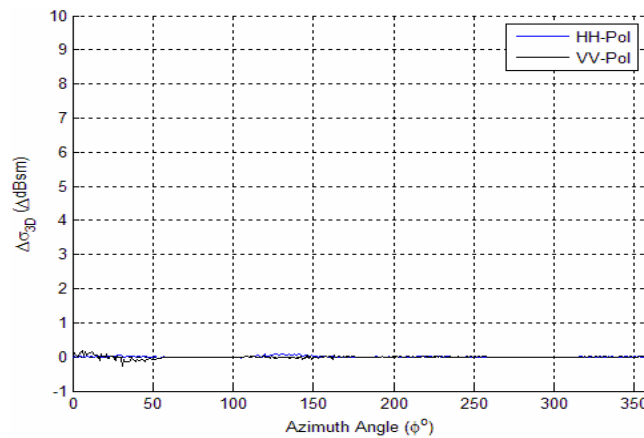


Figure 4-30: XPatch difference plots of non-paneled missile configurations vs. paneled missile configuration over L-S band frequencies.

In VV-polarization, the effects of paneling raise the RCS signature by approximately 3 dBsm with the effects centered at $\varphi = 45^\circ$ and $\varphi = 135^\circ$, angles that are 45° apart from broadside. These angles correspond to when the panel rivets and the missile body create a 45° dihedral and produces a large return. In HH-polarization a similar phenomenon occurs except that the RCS differences are centered approximately 60° away from broadside at $\varphi = 25^\circ$ and $\varphi = 150^\circ$. The significance of the why the maximum returns are centered 60° away from broadside is still a mystery.

Though paneling increases the RCS at specific angular regions by up to 9 dBsm, one should note that these elevated differences occur at non-specular regions which were -10 dBsm or lower. Paneling essentially creates a -10 dBsm RCS “floor” where the RCS of the missile cannot be below a certain dBsm level over the angular region where paneling effects are present. Figure 4-31 serves as an illustration to show that the angles where the RCS increased the most due to the effects of paneling were the same angles of lowest signature before the panels were added. Any specular return would easily drown out the effects of the panels.

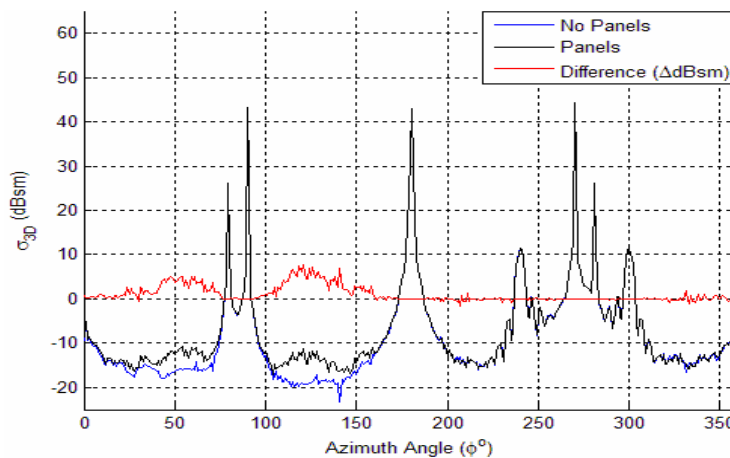


Figure 4-31: XPatch RCS plot comparison of a paneled and non-paneled missile configuration in HH-polarization at $\theta = 0^\circ$.

From Figure 4-30 it is obvious that the effects of paneling are negligible in the L-S band frequencies. The wavelength of the center frequency of 2.5 GHz is 120 mm which is almost 10 times the length of the 15 mm diameter rivets. A lower frequency results in lower resolution. In L-S band the resolution of the illuminating frequency is so low that the panels cannot be seen by the receiver.

In conclusion, the effects of panels are dependent mostly on polarization and frequency. How polarization affects the RCS effects of paneling will be dependent on the geometry of the target. The effects of frequency are as follows: the higher the frequency, the more significant the effects of paneling become. On a log scale RCS plot, paneling will make its biggest impact in the non-specular regions of the plot. Because the effects of paneling are relatively small, its effects are easily drowned out by specular returns.

5 Conclusion

The original problem statement was to investigate how the monostatic radar signature changes as a result of changes in four specific ballistic missile features: nosecones, fins, heat shielding and panels. The conclusions of this study are given in this section.

5.1 *Missile Components Conclusions*

Nosecones: From the results of this study, when a nosecone on a missile is changed, the angles that are the most sensitive to the change are the normals to the half angles of the nosecone conic components. Discontinuities within the nosecone geometry will cause diffractive effects which are strongest at nose on aspects.

Fins: Adding fins on a finless missile raises the overall RCS level of the missile. The angles of high specular return, such as the broadside of a missile, were insensitive to the addition of fins. Fin edges can have a significant impact on the sensitivity of an RCS plot depending on the orientation of the fin edges. If the normal to the fin edge occurs at an angle where specular returns are dominant, the effect of the fin edge will not make much difference at that angle. However, if the normal to the edge occurs at an angle that is dominated by non-specular returns, RCS will be very sensitive to that particular fin edge.

Panels: From the XPatch data, the sensitivity of the RCS to the effects of paneling is heavily dependent on the size of the rivets and the frequency and polarization of the illuminating wave. VV-polarization will generally result in a higher change in RCS.

When the wavelength of the illuminating wave is longer than the dimensions of the rivets or panels, the effects of paneling are negligible. However, if the wavelength of the illuminating wave is smaller than the dimensions of the panel features, there will be a significant increase in RCS in the non-specular portions of the missile RCS. Paneling will essentially cause an RCS “floor” in which non-specular regions that were lower in RCS than the floor level before paneling will be raised to that floor level. In the case of the 15 mm diameter rivet paneling, the RCS floor was -10 dBsm.

Heat shields: The greatest effect that heat shielding has on the RCS of a missile occurs at the angles of specular returns. Heat shielding makes a tremendous impact on cutting down specular RCS. On a nosecone, heat shielding would make its greatest impact on the normals to the half angles of the conic components of the nosecones. Because the return path of the illuminating wave is different in the two missile configuration, the phase interactions will be add constructively and destructively at different angles giving rise to oscillations and areas of higher RCS in the heat shielded configuration near the nose on aspects. However, there is an overall drop in RCS on average in that region.

5.2 Conclusions of XPatch and C&S Approximations

Even though diffraction and polarization were not accounted for in the C&S approximations, the C&S formulas generally did a good job matching the results of the XPatch simulations. The C&S formulas matched remarkably well for the nosecone configurations. For the configurations that had fins, the RCS of the C&S formulas usually returned RCS levels much lower than the XPatch RCS results in the nonspecular azimuth

regions. The lower RCS is because the C&S formulas did not account for diffraction off of the wing edges or multiple bounces off the fins. Other than the non-specular regions, the RCS of the XPatch data and the C&S data matched very well.

The C&S formulas are a highly useful tool when used within its limitations. It is fortunate that the geometry of a ballistic allows few multiple bounces as long as the fins are small. As long as the wavelength of the illuminating frequency is much smaller than that of any missile component, the C&S formulas should give a solid estimate on the RCS of the missile. When many interactions or diffractive components are present on the missile geometry, it would be recommended to use XPatch instead of the C&S approximations. XPatch is not as limited as C&S in the areas of interactions and diffraction. However, the C&S formulas do carry the benefit of not having to build the geometry of the target as a facet file or some other geometry.

5.3 Recommendations for Follow-On Research

This study scratches the surface of a study with literally an infinite number of possible configurations. However, rather than arbitrarily varying missile components, it would be interesting to study in depth one particular component, such as the nosecone, and develop a mathematical relationship or rule-of-thumb relationship for any variation of that component. For example, the nosecones that were dealt with in this thesis were straight conic shapes. An ogive or spheroid shape will have a different characteristic across azimuth and elevation than the straight conic shapes used in this thesis. A relationship may be obtained for nosecones as a function of curvature and length.

Another follow on topic would be to find a quick approximation in order to account for second order electromagnetic effects such as diffraction, traveling waves, creeping waves, *etc.* This topic combined with the C&S formulas would provide a quick yet closer approximation to the true RCS of a target.

APPENDIX A: SAMPLE XPATCH INPUT FILE

```
##
## WARNING!! These input settings were generated by the graphical
## user interface.
## There are a number of dependent and calculated fields in this file.
## Be forewarned
## that modifying these values with an editor (ie - not the GUI) or
## via other
## programmatic methods (ie - awk, sed, perl scripts) may cause data
## inconsistencies
## and potentially cause errors when the input page is read into xp4
## or read back into
## the GUI.
##

[Xpatch]
Comments =
EM Simulation Mode = Xpatch Far-field
Last Xpatch GUI Edit Date =
Project Name =
Xpatch Version = 4.7.22

[CAD Models]
Files = /home/user/Sang/PEC/missile.facet facet true
Settings Enabled = 1
Units = mm

[Materials]
DSA Exception Component IDs =
ICOAT for Total Ray Absorbers = 28
Material Setting = All PEC (no materials)
Material Settings File = ""
Number of DSA Exception Components = 0
Number of Random Materials = 0
Random Materials Table =
Settings Enabled = 1
Undersampling Ratio for Reflection/Transmission Table = 10
Use Dark Side Absorption (DSA) = false

[EM Physics]
Calculate Shadow Boundary diffraction = false
Calculate TILDC edge/face associations = false
Contributing Bounces = First/Last Bounces
EDGE File = /home/user/Sang/PEC/missile.edge
First Bounce Algorithm = SBR
Higher Order Bounces = Scattered Field Only
Include Diffraction from Edge = true
Include Diffraction from Gap, Crack, or Bump = false
Include Diffraction from line scatterers = false
Include Diffraction from point scatterers = false
LINESCATR File = ""
MSCILDC File = ""
Maximum Bounces = 5
Maximum Surfaces Per Voxel = 10
```

Maximum Tree Depth = 20
Minimum Bounce to Include = 1
Minimum Number of Bounces for Cavity Rays = 10
Number of Surface Currents Target Components = 1
PO Blockage Interval (deg) = 0.9
PO CellMax = 0.1
PO Uses CellMax = false
PTSCATR File = ""
Ray History Version = 1
Rays Per Wavelength = 10.0
Settings Enabled = 1
Skip Early Bounces = false
Skip PO Blockage Check = false
Surface Currents Component IDs (ICOMP) = 0
Surface Currents Maximum Cell Spacing = 1.0
Surface Currents Mode = No Surface Currents
Total Field Integration for Penetrable Materials = false
Use Adjacency Filter = true
Use Divergence Factor = false
Use One Bounce Only = false
Use Single Precision Facet Calculations = false
Write Ray History File = false

[Signature Settings]

Angular Increment = 0.02355912
Angular Span = 6.03113468
Bandwidth = 2.0
Center Frequency = 9.5
Cross-Range Bin Size = 149.89622913894
Cross-Range Oversample Factor = 0.99999999999993
Delta Time = 0.5
Discrete Frequency List = 10.0
Down Range Bin Size = 74.9481145
Down Range Resolution = 74.9481145
Edge Icomp = -2
FFT Angular Window File = ""
FFT Frequency Window File = ""
FFT Range Weight = 50.0
FFT Range n_bar = 8
FFT Window Choice = Uniform
FFT X-Range Weight = 50.0
FFT X-Range n_bar = 8
Frequency Increment = 0.064516129032258
GapIldc Icomp = -3
Generate Frequency Spectrum = false
Generate Ray Path Tree = false
Generate SAR Image = false
Generate SAR Image Mask = false
Generate SAR Image Mask Only = false
Generate Traceback Information = false
Ground Icomp = 1
Ground Squint Angle = 90.0
Hybrid Icomp = -4
Mask Height Above Ground = 609.59999985359
Mask Material ID for Ground = 5
Maximum Number of SC's = 50
Maximum Number of SC's Total = 320

Multi-look angle skip size (in bins) = 5.0
 Multi-look window size (in bins) = 11.0
 Number of Frequency Steps = 31
 Number of Range Bins = 32
 Number of X-Range Bins = 256
 Polarization = VV HH VH HV
 RCS Frequency Mode = Use Uniform Frequencies
 Range Oversample Factor = 1.0
 Run Computation = Compute in Frequency Domain
 SC Dynamic Range = 55.0
 Segregate Edges = false
 Segregate Gap ILDCs = false
 Segregate Ground = false
 Segregate Hybrid = false
 Settings Enabled = 1
 Signature Entry Mode = RCS
 Square Image Pixels = false
 Start Frequency = 8.5
 Start Range = -1199.169832
 Start Time = -8.0
 Start X-Range = -19186.71732978358
 Stop Frequency = 10.5
 Stop Range = 1199.169832
 Stop Time = 8.0
 Stop X-Range = 19186.717329784
 Use Multi-look field compensation = false
 X-Range Resolution = 149.89622913893

[Aspects]
 AZ Increment = 1.0
 AZ Start = 0.0
 AZ Stop = 360.0
 Antenna Mode = Mono-static
 Aspect Angle Choice = Use Aspect Sweep
 Aspect List (EL, AZ) =
 EL Increment = 3.0
 EL Start = 0.0
 EL Stop = 15.0
 Model Pose = Default
 Number of AZ Steps = 360
 Number of EL Steps = 5
 Rx Antenna AZ Offset = 0.0
 Rx Antenna EL Offset = 0.0
 SAR Image Orientation = Horizontal Sweep
 Settings Enabled = 1
 Target RPY End = 0.0 0.0 0.0
 Target RPY Order = 2 1 3
 Target RPY Start = 0.0 0.0 0.0
 Target RPY Steps = 0 0 0
 Target X-axis = 1.0 0.0 0.0
 Target Y-axis = 0.0 1.0 0.0
 Target Z-axis = 0.0 0.0 1.0
 Tx Antenna AZ = 0.0
 Tx Antenna EL = 0.0

APPENDIX B: MATLAB RCS APPROXIMATION CODE

RCS Approximation Code for Generic Ballistic Missile:

```
%*****
%*****
%RCS Approximation Code for Generic Ballistic Missile
%By Lt Sang Lee
% This program utilizes the the Crispin and Siegel formulas in
combination to the method of random phase in order to output the
estimated RCS of the ballistic missile. The nosecones and fins can be
changed in 3 different configurations each. This program is only valid
for elevations under 15 degrees and frequencies above 1.5 GHz. This
program must be used in conjunction with the SpecCalc.m file. The RCS of
the generic ballistic missile is te variable 'RCS'.
%*****
%*****
clear;clc;close all;
%*****
%*****
%Inputs
%*****
%*****
f=input('Enter Frequency(in GHz):');
f=f*1e9
theta=input('Enter Elevation(Degrees)');
theta=theta*pi/180;
%*****
%*****
%General Calculations/ Constants
%*****
%*****
resolution=361;
lambda=3e8/f;
beta=2*pi/lambda;
gamma=1.78;
phi=linspace(0,2*pi,resolution);
phi_calc=phi;index=find(phi<theta);phi_calc(index)=theta;
angular_buffer=15*pi/180;
%*****
%*****
***
%Cylinder Body
%*****
%*****
radius_BodyCylinder=.64;
length_BodyCylinder=13;
sigma_BodyCylinder=(lambda*radius_BodyCylinder*sin(phi_calc))./(8*pi*cos
(phi_calc).^2);
max_phi=max(phi);
n=floor(max_phi/pi);
for k=0:n
    index=find(phi==(k*pi+pi/2));

sigma_BodyCylinder(index)=(2*pi*radius_BodyCylinder*length_BodyCylinder^
2)/lambda;
end
sigma_BodyCylinder=abs(sigma_BodyCylinder);
%*****
phi_end=linspace(0,2*pi,resolution);
toggle_EndCap=zeros(1,resolution);
```

```

index_EndCap=find(phi>pi/2 & phi<3/2*pi);
toggle_EndCap(index_EndCap)=1;
if theta==0
    index=find(phi==pi);
    sigma_EndCap(index)=4*pi*(pi*radius_BodyCylinder^2)/(lambda^2);
    sigma_EndCap=((pi*radius_BodyCylinder^2)./(tan(phi-
pi).^2)).*besselj(1,4*pi*radius_BodyCylinder*sin(phi-pi)/lambda).^2;
else
    sigma_EndCap=SpecCalc(f, [-1 0 0], theta, radius_BodyCylinder, phi).';
end
sigma_EndCap=abs(sigma_EndCap).*toggle_EndCap;
sigma_BodyCylinder=sigma_BodyCylinder+sigma_EndCap;
%*****
%*****
%Flat Back Cone
%*****
%*****
phi_Cone=linspace(0,pi,floor(resolution/2)+1);
halfangle_SimpleCone=11*pi/180;
toggle_SimpleCone=zeros(1,resolution);
index_SimpleCone=find(phi>=0 & phi<=(pi/2)+angular_buffer | (phi<=2*pi &
phi>3/2*pi-angular_buffer));
toggle_SimpleCone(index_SimpleCone)=1;
L2=radius_BodyCylinder/tan(halfangle_SimpleCone);
L1=L2-3;
phi_cone_normal=(pi/2)-halfangle_SimpleCone;
for k=1:length(phi_Cone);
    if (phi_calc(k)== 0)

sigma_SimpleCone(k)=pi^3*(radius_BodyCylinder^2)/(((3*pi/2)+halfangle_Si
mpleCone)^2)*((csc(4*pi^2/(3*pi+2*halfangle_SimpleCone)))^2);
        elseif (phi_calc(k)<(phi_cone_normal-.005*halfangle_SimpleCone))

sigma_SimpleCone(k)=(((lambda*L2*tan(halfangle_SimpleCone))/(8*pi*sin(pi
-phi_calc(k))))*(tan(pi-phi_calc(k)-halfangle_SimpleCone)^2));
        elseif (phi_calc(k)<(phi_cone_normal+.005*halfangle_SimpleCone) &&
(phi_calc(k)>(phi_cone_normal-.005*halfangle_SimpleCone)))
            sigma_SimpleCone(k)=(L2^(3/2)-
L1^(3/2))^2*(8*pi)/(9*lambda)*sin(halfangle_SimpleCone)/(cos(halfangle_S
impleCone)^4);
        elseif
(phi_calc(k)>(phi_cone_normal+.005*halfangle_SimpleCone)&&phi_calc(k)<pi
/2)

sigma_SimpleCone(k)=(((lambda*L2*tan(halfangle_SimpleCone))/(8*pi*sin(pi
-phi_calc(k))))*(tan(pi-phi_calc(k)-halfangle_SimpleCone)^2));
        else
            sigma_SimpleCone(k)=((pi*radius_BodyCylinder^2)./(tan(phi_Cone(k)-
pi).^2)).*besselj(1,4*pi*radius_BodyCylinder*sin(phi_Cone(k)-
pi)/lambda).^2;
        end
    end
sigma_SimpleCone=[sigma_SimpleCone
fliplr(sigma_SimpleCone(1:length(sigma_SimpleCone)-1))];
index=find(phi<(180+.001)*pi/180 & phi>(180-.001)*pi/180);
sigma_SimpleCone(index)=4*pi*(pi*radius_BodyCylinder^2)/(lambda^2);
sigma_SimpleCone=toggle_SimpleCone.*abs(sigma_SimpleCone);
%*****
%*****
%Spheroid Nosecone Tip
%*****
%*****
r_SpheroidTip=.075;
toggle_SpheroidTip=zeros(1,resolution);

```

```

index_SpheroidTip=find(phi<=pi/2-halfangle_SimpleCone | phi>=2*pi-
pi/2+halfangle_SimpleCone);
toggle_SpheroidTip(index_SpheroidTip)=1;
sigma_SpheroidTip=ones(1,resolution)*pi*r_SpheroidTip^2;
sigma_SpheroidTip=toggle_SpheroidTip.*sigma_SpheroidTip;
%*****
%*****
%Bi-Conic Nose Cone
%*****
%*****
halfangle_BiCone1=10*pi/180;
halfangle_BiCone2=12*pi/180;
length_BiCone1=1.6;
length_BiCone2=1.4;
toggle_BiCone1=zeros(1,resolution);
index_BiCone=find((phi>=0 & phi<=(pi/2)+angular_buffer) | (phi<=2*pi &
phi>=3/2*pi-angular_buffer));
toggle_BiCone1(index_BiCone)=1;
L2=radius_BodyCylinder/tan(halfangle_BiCone1);
L1=L2-length_BiCone1;
phi_cone_normal=(pi/2)-halfangle_BiCone1;
for k=1:length(phi_Cone);
    if (phi_calc(k)== 0)

sigma_BiCone1(k)=pi^3*(radius_BodyCylinder^2)/(((3*pi/2)+halfangle_BiCone1)^2)*((csc(4*pi^2/(3*pi+2*halfangle_BiCone1)))^2);
    elseif (phi_calc(k)<(phi_cone_normal-.005*halfangle_BiCone1))

sigma_BiCone1(k)=(((lambda*L2*tan(halfangle_BiCone1))/(8*pi*sin(pi-phi_calc(k))))*(tan(pi-phi_calc(k)-halfangle_BiCone1))^2));
    elseif (phi_calc(k)<(phi_cone_normal+.005*halfangle_BiCone1) &&
(phi_calc(k)>(phi_cone_normal-.005*halfangle_BiCone1)))
        sigma_BiCone1(k)=(L2^(3/2)-
L1^(3/2))^2*(8*pi)/(9*lambda)*sin(halfangle_BiCone1)/(cos(halfangle_BiCone1)^4);
    elseif
(phi_calc(k)>(phi_cone_normal+.005*halfangle_BiCone1)&&phi_calc(k)<pi/2)

sigma_BiCone1(k)=(((lambda*L2*tan(halfangle_BiCone1))/(8*pi*sin(pi-phi_calc(k))))*(tan(pi-phi_calc(k)-halfangle_BiCone1))^2));
    else
        sigma_BiCone1(k)=((pi*radius_BodyCylinder^2)./(tan(phi_Cone(k)-pi).^2)).*besselj(1,4*pi*radius_BodyCylinder*sin(phi_Cone(k)-pi)/lambda).^2;
    end
end
sigma_BiCone1=[sigma_BiCone1
fliplr(sigma_BiCone1(1:length(sigma_BiCone1)-1))]; % (make 360 from 180
due to symetry)
index=find(phi<(180+.001)*pi/180 & phi>(180-.001)*pi/180);
sigma_BiCone1(index)=4*pi*(pi*radius_BodyCylinder^2)/(lambda^2);
%*****
%*****
toggle_BiCone2=zeros(1,resolution);
index_BiCone=find((phi>=0 & phi<=(pi/2)+angular_buffer) | (phi<=2*pi &
phi>=3/2*pi-angular_buffer));
toggle_BiCone2(index_BiCone)=1;
L2=length_BiCone1*tan(halfangle_BiCone1);
L1=L2-length_BiCone2;
phi_cone_normal=(pi/2)-halfangle_BiCone2;
for k=1:length(phi_Cone);
    if (phi_calc(k)== 0)
sigma_BiCone2(k)=pi^3*(radius_BodyCylinder^2)/(((3*pi/2)+halfangle_BiCone2)^2)*((csc(4*pi^2/(3*pi+2*halfangle_BiCone2)))^2);
    elseif (phi_calc(k)<(phi_cone_normal-.005*halfangle_BiCone2))

```

```

sigma_BiCone2(k)=(((lambda*L2*tan(halfangle_BiCone2))/(8*pi*sin(pi-
phi_calc(k))))*(tan(pi-phi_calc(k)-halfangle_BiCone2))^2));
elseif (phi_calc(k)<(phi_cone_normal+.005*halfangle_BiCone2) &&
(phi_calc(k)>(phi_cone_normal-.005*halfangle_BiCone2)))
    sigma_BiCone2(k)=(L2^(3/2)-
L1^(3/2))^2*(8*pi)/(9*lambda)*sin(halfangle_BiCone2)/(cos(halfangle_BiCo
ne2)^4);
elseif
(phi_calc(k)>(phi_cone_normal+.005*halfangle_BiCone2)&&phi_calc(k)<pi/2)

sigma_BiCone2(k)=(((lambda*L2*tan(halfangle_BiCone2))/(8*pi*sin(pi-
phi_calc(k))))*(tan(pi-phi_calc(k)-halfangle_BiCone2))^2));
else
    sigma_BiCone2(k)=((pi*radius_BodyCylinder^2)/(tan(phi_Cone(k)-
pi).^2)).*besselj(1,4*pi*radius_BodyCylinder*sin(phi_Cone(k)-
pi)/lambda).^2;
end
end
sigma_BiCone2=[sigma_BiCone2
fliplr(sigma_BiCone2(1:length(sigma_BiCone2)-1))];
index=find(phi<(180+.001)*pi/180 & phi>(180-.001)*pi/180);
sigma_BiCone2(index)=4*pi*(pi*radius_BodyCylinder^2)/(lambda^2);
sigma_BiCone=(toggle_BiCone1.*abs(sigma_BiCone1))+(toggle_BiCone2.*abs(s
igma_BiCone2));
%*****
%*****
%Broken Nose Cone
%*****
%*****
halfangle_BrokenCone1=21*pi/180;
halfangle_BrokenCone2=11*pi/180;
radius_BrokenCylinder=.2625;
length_BrokenCone1=(radius_BodyCylinder-
radius_BrokenCylinder)/tan(halfangle_BrokenCone1);
length_BrokenCylinder=(3-length_BrokenCone1)/1;
length_BrokenCone2=length_BrokenCylinder;
toggle_BrokenCone1=zeros(1,resolution);
index_BrokenCone=find((phi>=0 & phi<=(pi/2)+angular_buffer) | (phi<=2*pi
& phi>3/2*pi-angular_buffer));
toggle_BrokenCone1(index_BrokenCone)=1;
L2=radius_BodyCylinder/tan(halfangle_BrokenCone1);
L1=L2-length_BrokenCone1;
phi_cone_normal=(pi/2)-halfangle_BrokenCone1
for k=1:length(phi_Cone);
    if (phi_calc(k)== 0)
        sigma_BrokenCone1(k)=pi^3*(radius_BodyCylinder^2)/(((3*pi/2)+halfangle_B
rokenCone1)^2)*(csc(4*pi^2/(3*pi+2*halfangle_BrokenCone1)))^2);
    elseif (phi_calc(k)<(phi_cone_normal-.005*halfangle_BrokenCone1))
        sigma_BrokenCone1(k)=(((lambda*L2*tan(halfangle_BrokenCone1))/(8*pi*sin(
pi-phi_calc(k))))*(tan(pi-phi_calc(k)-halfangle_BrokenCone1))^2));
    elseif (phi_calc(k)<(phi_cone_normal+.005*halfangle_BrokenCone1) &&
(phi_calc(k)>(phi_cone_normal-.005*halfangle_BrokenCone1)))
        sigma_BrokenCone1(k)=(L2^(3/2)-
L1^(3/2))^2*(8*pi)/(9*lambda)*sin(halfangle_BrokenCone1)/(cos(halfangle_
BrokenCone1)^4);
    elseif (phi_calc(k)>(phi_cone_normal+.005*halfangle_BrokenCone1) &&
phi_calc(k)<pi/2)
        sigma_BrokenCone1(k)=(((lambda*L2*tan(halfangle_BrokenCone1))/(8*pi*sin(
pi-phi_calc(k))))*(tan(pi-phi_calc(k)-halfangle_BrokenCone1))^2));
    else
        sigma_BrokenCone1(k)=((pi*radius_BodyCylinder^2)/(tan(phi_Cone(k)-
pi).^2)).*besselj(1,4*pi*radius_BodyCylinder*sin(phi_Cone(k)-
pi)/lambda).^2;
    end
end

```

```

end
sigma_BrokenCone1=[sigma_BrokenCone1
fliplr(sigma_BrokenCone1(1:length(sigma_BrokenCone1)-1))];
index=find(phi<(180+.001)*pi/180 & phi>(180-.001)*pi/180);
sigma_BrokenCone1(index)=4*pi*(pi*radius_BodyCylinder^2)/(lambda^2);
sigma_BrokenCone1=toggle_BrokenCone1.*abs(sigma_BrokenCone1);
%*****
toggle_BrokenCylinder=zeros(1,resolution);
index_BrokenCylinder=find(phi>=0 & phi<=pi-halfangle_BrokenCone1 |
phi<=2*pi & phi>=pi+halfangle_BrokenCone2);
toggle_BrokenCylinder(index_BrokenCylinder)=1;
sigma_BrokenCylinder=(lambda*radius_BrokenCylinder*sin(phi_calc))./(8*pi
*cos(phi_calc).^2);
max_phi_body=max(phi);
n=floor(max_phi_body/pi);
for k=0:n
    index=find(phi==(k*pi+pi/2));
    sigma_BrokenCylinder(index)=(2*pi*radius_BrokenCylinder*length_BrokenCyl
inder^2)/lambda;
end
sigma_BrokenCylinder=abs(sigma_BrokenCylinder).*toggle_BrokenCylinder;
%*****
toggle_BrokenCone2=zeros(1,resolution);
index_BrokenCone=find((phi>=0 & phi<(pi/2)+angular_buffer) | (phi<=2*pi
& phi>3/2*pi-angular_buffer));
toggle_BrokenCone2(index_BrokenCone)=1;
L2=radius_BrokenCylinder/tan(halfangle_BrokenCone2);
L1=L2-length_BrokenCone2;
phi_cone_normal=(pi/2)-halfangle_BrokenCone2;      %(normal to flatback
cone)
for k=1:length(phi_Cone);
    if (phi_calc(k)== 0)
        sigma_BrokenCone2(k)=pi^3*(radius_BodyCylinder^2)/(((3*pi/2)+halfangle_B
rokenCone2)^2)*(csc(4*pi^2/(3*pi+2*halfangle_BrokenCone2)))^2);
    elseif (phi_calc(k)<(phi_cone_normal-.005*halfangle_BrokenCone2))
        sigma_BrokenCone2(k)=((lambda*L2*tan(halfangle_BrokenCone2))/(8*pi*sin(
pi-phi_calc(k))))*(tan(pi-phi_calc(k)-halfangle_BrokenCone2)^2);
    elseif (phi_calc(k)<(phi_cone_normal+.005*halfangle_BrokenCone2) &&
(phi_calc(k)>(phi_cone_normal-.005*halfangle_BrokenCone2)))
        sigma_BrokenCone2(k)=(L2^(3/2)-
L1^(3/2))^2*(8*pi)/(9*lambda)*sin(halfangle_BrokenCone2)/(cos(halfangle_
BrokenCone2)^4);
    elseif
(phi_calc(k)>(phi_cone_normal+.005*halfangle_BrokenCone2)&&phi_calc(k)<p
i/2)
        sigma_BrokenCone2(k)=((lambda*L2*tan(halfangle_BrokenCone2))/(8*pi*sin(
pi-phi_calc(k))))*(tan(pi-phi_calc(k)-halfangle_BrokenCone2)^2);
    else
        sigma_BrokenCone2(k)=(pi*radius_BodyCylinder^2)/(tan(phi_Cone(k)-
pi).^2).*besselj(1,4*pi*radius_BodyCylinder*sin(phi_Cone(k)-
pi)/lambda).^2;
    end
end
sigma_BrokenCone2=[sigma_BrokenCone2
fliplr(sigma_BrokenCone2(1:length(sigma_BrokenCone2)-1))];
index=find(phi<(180+.001)*pi/180 & phi>(180-.001)*pi/180);
sigma_BrokenCone2(index)=4*pi*(pi*radius_BodyCylinder^2)/(lambda^2);
sigma_BrokenCone2=abs(sigma_BrokenCone2).*toggle_BrokenCone2;
sigma_BrokenCone=sigma_BrokenCone1+sigma_BrokenCone2+sigma_BrokenCylind
er;
%*****
%*****
%Raceway
%*****

```



```

%*****
length_Raceway=9.4;
width_Raceway=.1;
edgeangle_Raceway=30*pi/180;
toggle_Raceway=zeros(1,resolution);
index_Raceway=find(phi>pi);
toggle_Raceway(index_Raceway)=1;
sigma_RacewayBody=(lambda*(width_Raceway/2)*sin(phi_calc))./(8*pi*cos(phi_
i_calc).^2);
max_phi_body=max(phi);
n=floor(max_phi_body/pi);
for k=0:n
    index=find(phi==(k*pi+pi/2));

sigma_RacewayBody(index)=(2*pi*(width_Raceway/2)*length_Raceway^2)/lambda;
end
sigma_RacewayBody=abs(sigma_RacewayBody).*toggle_Raceway;
%*****
side_Approximation=sqrt(.1/sin(edgeangle_Raceway)*width_Raceway);
toggle_RacewayEdge1=zeros(1,resolution);
index_RacewayEdge1=find(phi>=pi & phi<=3/2*pi);
toggle_RacewayEdge1(index_RacewayEdge1)=1;
if theta==0

sigma_RacewayEdge1=4*pi*side_Approximation^4/(lambda^2)*sinc(beta*side_A
pproximation*sin(phi+pi/2+edgeangle_Raceway)/pi).^2;
else
    r=sqrt(side_Approximation^2/pi);
    sigma_RacewayEdge1=SpecCalc(f,[-sind(30) -sind(60)
0],theta,r,phi).';
end
sigma_RacewayEdge1=abs(sigma_RacewayEdge1).*toggle_RacewayEdge1;
%*****
toggle_RacewayEdge2=zeros(1,resolution);
index_RacewayEdge2=find(phi>=3/2*pi);
toggle_RacewayEdge2(index_RacewayEdge2)=1;
if theta==0
sigma_RacewayEdge2=4*pi*side_Approximation^4/(lambda^2)*sinc(beta*side_A
pproximation*sin(phi+pi/2-edgeangle_Raceway)/pi).^2;
else
    r=sqrt(side_Approximation^2/pi);
    sigma_RacewayEdge2=SpecCalc(f,[sind(30) -sind(60) 0],theta,r,phi).';
end
sigma_RacewayEdge2=abs(sigma_RacewayEdge2).*toggle_RacewayEdge2;
sigma_Raceway=sigma_RacewayBody+sigma_RacewayEdge1+sigma_RacewayEdge2;
%*****
%*****
%Small Fins
%*****
fin_L=1.025;
fin_h=.346;
fin_ang=31*pi/180;
fin_thick=.1;
edge_hyp=fin_h/sin(fin_ang);
edge_hyp_xL=fin_h/tan(fin_ang);
edge_shortL=fin_L-fin_h/tan(fin_ang);
fin_spec_A=fin_h*(fin_L-
fin_h/tan(fin_ang))+(fin_h*fin_h/tan(fin_ang))/2;
r_spec=sqrt(fin_spec_A/pi);
W_spec=sqrt(fin_spec_A/(fin_L/fin_h+1));
L_spec=(fin_L/fin_h)*W_spec;
fin_ang_edge_A=fin_thick*edge_hyp;

```

```

r_ang=sqrt(fin_ang_edge_A/pi);
W_ang=sqrt(fin_ang_edge_A/(edge_hyp/fin_thick+1));
L_ang=edge_hyp/fin_thick*W_ang;
fin_shortL_A=fin_thick*edge_shortL;
r_shortL=sqrt(fin_shortL_A/pi);
W_shortL=sqrt(fin_shortL_A/(edge_shortL/fin_thick+1));
L_shortL=edge_shortL/fin_thick*W_ang;
fin_h_A=fin_thick*fin_h;
r_h=sqrt(fin_h_A/pi);
W_h=sqrt(fin_h_A/(fin_h/fin_thick+1));
L_h=fin_h/fin_thick*W_h;
toggle=zeros(1,resolution);
index=find((phi>=angular_buffer & phi<=pi-angular_buffer) | (phi<=2*pi-
angular_buffer & phi>=pi+angular_buffer));
toggle(index)=1;
if theta==0
sigma_spec_w1234=2*(4*pi*W_spec^2*L_spec^2/lambda^2)*sin(phi).^2.*sinc(b
eta*L_spec*cos(phi)/pi).^2;
else
sigma_spec_w1234=2*SpecCalc(f,[0 1 0],theta,r_spec,phi).';
end
sigma_spec_w1234=abs(sigma_spec_w1234).*toggle;
toggle=zeros(1,resolution);
index=find(phi>=0 & phi<angular_buffer | phi<=2*pi & phi>=2*pi-
angular_buffer);
toggle(index)=1;
if theta==0
sigma_ang_w1=(4*pi*W_ang^2*L_ang^2/lambda^2)*sin(phi).^2.*sinc(beta*L_an
g*cos(phi)/pi).^2;
else
sigma_ang_w1=SpecCalc(f,[sind(30) 0 sind(59)],theta,r_ang,phi).';
end
sigma_ang_w1=abs(sigma_ang_w1).*toggle;
toggle=zeros(1,resolution);
index=find(phi>=pi/2 & phi<3/2*pi);
toggle(index)=1;
if theta==0
sigma_perp_w13=2*(4*pi*W_h^2*L_h^2/lambda^2)*sin(phi-
pi/2).^2.*sinc(beta*W_h*cos(phi-pi/2)/pi).^2;
else
sigma_perp_w13=2*SpecCalc(f,[-1 0 0],theta,r_h,phi).';
end
sigma_perp_w13=abs(sigma_perp_w13).*toggle;
toggle=zeros(1,resolution);
index=find(phi>=0 & phi<=pi/2);
toggle(index)=1;
if theta==0
sigma_ang_w2=(4*pi*W_ang^2*L_ang^2/lambda^2)*sin(phi+(31*pi/180)).^2.*si
nc(beta*L_ang*cos(phi+(31*pi/180))/pi).^2;
else
sigma_ang_w2=SpecCalc(f,[sind(30) sind(59) 0],theta,r_ang,phi).';
end
sigma_ang_w2=abs(sigma_ang_w2).*toggle;
toggle=zeros(1,resolution);
index=find(phi>angular_buffer & phi<pi-angular_buffer | phi<=2*pi-
angular_buffer & phi>pi+angular_buffer);
toggle(index)=1;
if theta==0
sigma_par_w24=(4*pi*W_shortL^2*L_shortL^2/lambda^2)*sin(phi).^2.*sinc(b
eta*W_shortL*cos(phi)/pi).^2;
else
sigma_par_w24=SpecCalc(f,[0 1 0],theta,r_shortL,phi).';
end
sigma_par_w24=abs(sigma_par_w24).*toggle;

```

```

toggle=zeros(1,resolution);
index=find(phi>=pi/2 & phi<3/2*pi);
toggle(index)=1;
if theta==0
sigma_perp_w24=2*(4*pi*W_h^2*L_h^2/lambda^2)*sin(phi).^2.*sinc(beta*L_h*
cos(phi)/pi).^2;
else
sigma_perp_w24=2*SpecCalc(f,[-1 0 0],theta,r_h,phi).';
end
sigma_perp_w24=abs(sigma_perp_w24).*toggle;
toggle=zeros(1,resolution);
index=find(phi>=0 & phi<angular_buffer | phi<=2*pi & phi>=2*pi-
angular_buffer);
toggle(index)=1;
if theta==0
sigma_ang_w3=(4*pi*W_ang^2*L_ang^2/lambda^2)*sin(phi).^2.*sinc(beta*L_an
g*cos(phi)/pi).^2;
else
sigma_ang_w3=SpecCalc(f,[sind(30) 0 -sind(59)],theta,r_ang,phi).';
end
sigma_ang_w3=abs(sigma_ang_w3).*toggle;
toggle=zeros(1,resolution);
index=find(phi>=3/2*pi & phi<=2*pi);
toggle(index)=1;
if theta==0
sigma_ang_w4=(4*pi*W_ang^2*L_ang^2/lambda^2)*sin(phi-
(31*pi/180)).^2.*sinc(beta*L_ang*cos(phi-(30*pi/180))/pi).^2;
else
sigma_ang_w4=SpecCalc(f,[sind(30) -sind(59) 0],theta,r_ang,phi).';
end
sigma_ang_w4=abs(sigma_ang_w4).*toggle;
%Combine
sigma_Fin_Small=sigma_spec_w1234+sigma_ang_w1+sigma_perp_w13+sigma_ang_w
2+sigma_par_w24+sigma_perp_w24+sigma_ang_w3+sigma_ang_w4;
%*****
%*****
%Large Fins
%*****
%*****
fin_L=2.05;
fin_h=.692;
fin_ang=31*pi/180;
fin_thick=.2;
edge_hyp=fin_h/sin(fin_ang);
edge_hyp_xL=fin_h/tan(fin_ang);
edge_shortL=fin_L-fin_h/tan(fin_ang);
fin_spec_A=fin_h*(fin_L-
fin_h/tan(fin_ang))+(fin_h*fin_h/tan(fin_ang))/2;
r_spec=sqrt(fin_spec_A/pi);
W_spec=sqrt(fin_spec_A/(fin_L/fin_h+1));
L_spec=(fin_L/fin_h)*W_spec;
fin_ang_edge_A=fin_thick*edge_hyp;
r_ang=sqrt(fin_ang_edge_A/pi);
W_ang=sqrt(fin_ang_edge_A/(edge_hyp/fin_thick+1));
L_ang=edge_hyp/fin_thick*W_ang;
fin_shortL_A=fin_thick*edge_shortL;
r_shortL=sqrt(fin_shortL_A/pi);
W_shortL=sqrt(fin_shortL_A/(edge_shortL/fin_thick+1));
L_shortL=edge_shortL/fin_thick*W_ang;
fin_h_A=fin_thick*fin_h;
r_h=sqrt(fin_h_A/pi);
W_h=sqrt(fin_h_A/(fin_h/fin_thick+1));
L_h=fin_h/fin_thick*W_h;
toggle=zeros(1,resolution);

```

```

index=find((phi>=angular_buffer & phi<=pi-angular_buffer) | (phi<=2*pi-
angular_buffer & phi>=pi+angular_buffer));
toggle(index)=1;
if theta==0
sigma_spec_w1234=2*(4*pi*W_spec^2*L_spec^2/lambda^2)*sin(phi).^2.*sinc(b
eta*L_spec*cos(phi)/pi).^2;
else
sigma_spec_w1234=2*SpecCalc(f,[0 1 0],theta,r_spec,phi).';
end
sigma_spec_w1234=abs(sigma_spec_w1234).*toggle;
toggle=zeros(1,resolution);
index=find(phi>=0 & phi<angular_buffer | phi<=2*pi & phi>=2*pi-
angular_buffer);
toggle(index)=1;
if theta==0
sigma_ang_w1=(4*pi*W_ang^2*L_ang^2/lambda^2)*sin(phi).^2.*sinc(beta*L_an
g*cos(phi)/pi).^2;
else
sigma_ang_w1=SpecCalc(f,[sind(30) 0 sind(59)],theta,r_ang,phi).';
end
sigma_ang_w1=abs(sigma_ang_w1).*toggle;
toggle=zeros(1,resolution);
index=find(phi>=pi/2 & phi<3/2*pi);
toggle(index)=1;
if theta==0
sigma_perp_w13=2*(4*pi*W_h^2*L_h^2/lambda^2)*sin(phi-
pi/2).^2.*sinc(beta*W_h*cos(phi-pi/2)/pi).^2;
else
sigma_perp_w13=2*SpecCalc(f,[-1 0 0],theta,r_h,phi).';
end
sigma_perp_w13=abs(sigma_perp_w13).*toggle;
toggle=zeros(1,resolution);
index=find(phi>=0 & phi<=pi/2);
toggle(index)=1;
if theta==0
sigma_ang_w2=(4*pi*W_ang^2*L_ang^2/lambda^2)*sin(phi+(31*pi/180)).^2.*si
nc(beta*L_ang*cos(phi+(31*pi/180))/pi).^2;
else
sigma_ang_w2=SpecCalc(f,[sind(30) sind(59) 0],theta,r_ang,phi).';
end
sigma_ang_w2=abs(sigma_ang_w2).*toggle;
toggle=zeros(1,resolution);
index=find(phi>angular_buffer & phi<pi-angular_buffer | phi<=2*pi-
angular_buffer & phi>pi+angular_buffer);
toggle(index)=1;
if theta==0
sigma_par_w24=(4*pi*W_shortL^2*L_shortL^2/lambda^2)*sin(phi).^2.*sinc(b
eta*W_shortL*cos(phi)/pi).^2;
else
sigma_par_w24=SpecCalc(f,[0 1 0],theta,r_shortL,phi).';
end
sigma_par_w24=abs(sigma_par_w24).*toggle;
toggle=zeros(1,resolution);
index=find(phi>=pi/2 & phi<3/2*pi);
toggle(index)=1;
if theta==0
sigma_perp_w24=2*(4*pi*W_h^2*L_h^2/lambda^2)*sin(phi).^2.*sinc(beta*L_h*
cos(phi)/pi).^2;
else
sigma_perp_w24=2*SpecCalc(f,[-1 0 0],theta,r_h,phi).';
end
sigma_perp_w24=abs(sigma_perp_w24).*toggle;
toggle=zeros(1,resolution);

```

```

index=find(phi>=0 & phi<angular_buffer | phi<=2*pi & phi>=2*pi-
angular_buffer);
toggle(index)=1;
if theta==0

sigma_ang_w3=(4*pi*W_ang^2*L_ang^2/lambda^2)*sin(phi).^2.*sinc(beta*L_an
g*cos(phi)/pi).^2;
else
    sigma_ang_w3=SpecCalc(f,[sind(30) 0 -sind(59)],theta,r_ang,phi).';
end
sigma_ang_w3=abs(sigma_ang_w3).*toggle;
toggle=zeros(1,resolution);
index=find(phi>=3/2*pi & phi<=2*pi);
toggle(index)=1;
if theta==0
    sigma_ang_w4=(4*pi*W_ang^2*L_ang^2/lambda^2)*sin(phi-
(31*pi/180)).^2.*sinc(beta*L_ang*cos(phi-(30*pi/180))/pi).^2;
else
    sigma_ang_w4=SpecCalc(f,[sind(30) -sind(59) 0],theta,r_ang,phi).';
end
sigma_ang_w4=abs(sigma_ang_w4).*toggle;
sigma_Fin_Large=sigma_spec_w1234+sigma_ang_w1+sigma_perp_w13+sigma_ang_w
2+sigma_par_w24+sigma_perp_w24+sigma_ang_w3+sigma_ang_w4;
%*****
%*****
%Combine
%*****
%*****
RCS=sigma_SimpleCone+sigma_Raceway+sigma_BodyCylinder+sigma_Raceway;
if theta==0
    index=find(phi==pi);
    RCS=4*pi*(pi*radius_BodyCylinder^2)/(lambda^2);
end

```

Flat Surface Specular Approximation Code:

```

%*****
%*****
%Specular Approximation Code
%By Lt Sang Lee
% This code approximates the specular return from an flat surface that
% is irregularly shaped. It is to be used with the missile approximation
% code.
%*****
%*****
function [sigma] = SpecCalc(f,norm,theta,r,phi)
lambda=3e8/f;
norm=repmat(norm,length(phi),1);
[x_inc,y_inc,z_inc]=sph2cart(phi.'-pi,ones(length(phi),1).*theta,1);
inc_ang=acos(dot(norm,[x_inc,y_inc,z_inc],2));
sigma=(pi*r^2)./(tan(inc_ang).^2)).*besselj(1,4*pi*r*sin(inc_ang)/lambd
a).^2;

```

BIBLIOGRAPHY

- [1] Crispin, J. W., and Maffett A. L. "Radar Cross-Section for Complex Shapes," Proceedings of the IEEE, Aug. 1965, Volume 53, Issue 8: 833 - 848
- [2] Crispin, J. W., Siegel K. M. Methods of Radar Cross Section Analysis. New York: Academic Press, 1968
- [3] Crispin, J. W., and Maffett A. L. "Radar Cross-Section for Simple Shapes," Proceedings of the IEEE, Aug. 1965, Volume 53, Issue 8: 972-982
- [4] Knott, Eugene F. Radar Cross Section. North Carolina: SciTech Publishing, 2004
- [5] Beck, Allan R. Investigation of Electromagnetic Scattering Effects From Aeroelastic Wing Deformations. Master's thesis, Graduate School of Engineering, Air Force Institute of Technology (AETC), Wright-Patterson AFB OH, March 1991. AFIT/GAE/AA/86D-1.
- [6] McKenzie, Samuel D. Investigation of the Effects of Aeroelastic Deformations on the Radar Cross Section of Aircraft. Master's thesis, Graduate School of Engineering, Air Force Institute of Technology (AETC), Wright-Patterson AFB OH, March 1986. AFIT/EN/ENG/91D-40.
- [7] Welsh, Bryon M., Muller, William D. and Kent, Brian M. "Air Force Research Laboratory Advanced Compact Range RCS Uncertainty Analysis for a General Target," IEEE Antennas and Propagation Magazine, Jun. 2003, Volume 45, No. 3: 195-2000
- [8] Whittman, R.C. et.al. "Proposed Analysis of RCS Measurement Uncertainty," Proc Antenna Measurement Techniques Association, Long Beach, 1994. 51-56
- [9] Balanis, Constantine A. Advanced Engineering Electromagnetics. New Jersey: John Wiley & Sons, 1989
- [10] Balanis, Constantine A. Antenna Theory: Analysis and Design. New Jersey: John Wiley & Sons, 1982

Vita

Lieutenant Sang H. Lee graduated from Stuyvesant High School in New York, New York in June 1999. He entered undergraduate studies at the State University University New York at Binghamton where he graduated with a Bachelor of Science degree in Electrical Engineering in 2003. He was commissioned as a 2nd Lieutenant through the Air Force Officer Training School at Maxwell AFB in Montgomery, Alabama.

Upon commissioning, his first assignment was at the aeronautical weapons branch of the National Air and Space Intelligence Center (NASIC) at Wright Patterson AFB in Dayton, Ohio. He returned to Maxwell AFB in the spring of 2004 to complete the Aerospace Basic Course and was chosen to attend the Air Force Institute of Technology (AFIT) shortly after as a Watson Scholar. At AFIT, his studies focus on Low Observables and Electromagnetics. Upon graduation, he will return to NASIC as a threat control engineer in the signatures branch.

REPORT DOCUMENTATION PAGE				Form Approved OMB No. 074-0188	
<p>The public reporting burden for this collection of information is estimated to average 1 hour per response, including the time for reviewing instructions, searching existing data sources, gathering and maintaining the data needed, and completing and reviewing the collection of information. Send comments regarding this burden estimate or any other aspect of the collection of information, including suggestions for reducing this burden to Department of Defense, Washington Headquarters Services, Directorate for Information Operations and Reports (0704-0188), 1215 Jefferson Davis Highway, Suite 1204, Arlington, VA 22202-4302. Respondents should be aware that notwithstanding any other provision of law, no person shall be subject to an penalty for failing to comply with a collection of information if it does not display a currently valid OMB control number.</p> <p>PLEASE DO NOT RETURN YOUR FORM TO THE ABOVE ADDRESS.</p>					
1. REPORT DATE (DD-MM-YYYY) 23-03-2006		2. REPORT TYPE Master's Thesis		3. DATES COVERED (From – To) Aug 2004 – Mar 2006	
4. TITLE AND SUBTITLE Investigation of the Effects of Target Feature Variations Ballistic Missile RCS				5a. CONTRACT NUMBER	
				5b. GRANT NUMBER	
				5c. PROGRAM ELEMENT NUMBER	
6. AUTHOR(S) Lee, Sang, H., First Lieutenant, USAF				5d. PROJECT NUMBER If funded, enter ENR #	
				5e. TASK NUMBER	
				5f. WORK UNIT NUMBER	
7. PERFORMING ORGANIZATION NAMES(S) AND ADDRESS(S) Air Force Institute of Technology Graduate School of Engineering and Management (AFIT/EN) 2950 Hobson Way Bldg 640 WPAFB OH 45433-7765				8. PERFORMING ORGANIZATION REPORT NUMBER AFIT/GE/ENG/06-34	
9. SPONSORING/MONITORING AGENCY NAME(S) AND ADDRESS(ES) National Air and Space Intelligence Center/ADNS MAJCOM: ACC Attn: Mr. Bob Schalle 4180 Watson Way WPAFB OH 45433-5648 Email: Robert.schalle@wpafb.af.mil DSN: 672-3084				10. SPONSOR/MONITOR'S ACRONYM(S)	
				11. SPONSOR/MONITOR'S REPORT NUMBER(S)	
12. DISTRIBUTION/AVAILABILITY STATEMENT APPROVED FOR PUBLIC RELEASE; DISTRIBUTION UNLIMITED.					
13. SUPPLEMENTARY NOTES					
14. ABSTRACT <p>Uncertainties in certain features of target geometries result in a loss of confidence in the signature assessment of the target. Knowledge of the impact to a target's radar cross section (RCS) due to changes to specific target features can assist to identify whether uncertainty in a certain target feature warrants a loss of confidence in the target signature. This study will allow a development of a general "rule-of-thumb" on how the radar signature of a target varies as a function of the target's specific target features. The targets of interest which this study is centered around are fictitious ballistic missiles. Four target features that were investigated: fin size, nosecone shape, effect of panel riveting along the sides of the missile and the effects of heat shielding on the nosecone. By varying each of the four target features into a missile configuration and comparing to another configuration, a relationship between specific target features and its effect on the radar cross section of a ballistic missile can be obtained. Based on the range of possible configurations that target's feature can take, it is possible to estimate a range of possible values of the radar signature. This will enable the user of the signature data to have a better understanding of the target being assessed and target characteristics when a complete knowledge of target configuration is unavailable.</p>					
15. SUBJECT TERMS Radar Cross Section, RCS, Uncertainty, Target Feature Variation, Ballistic, Crispin and Siegel					
16. SECURITY CLASSIFICATION OF:			17. LIMITATION OF ABSTRACT	18. NUMBER OF PAGES	19a. NAME OF RESPONSIBLE PERSON
REPORT U	ABSTRACT U	c. THIS PAGE U			James A. Fellows, Lt. Col., USAF (ENG)
				112	19b. TELEPHONE NUMBER (Include area code) (937) 255-3636, ext 7230; e-mail: james.fellows@afit.edu

Standard Form 298 (Rev: 8-8)

Prescribed by ANSI Std. Z39-18